Photonic switching in III/V nanostructures

Citation for published version (APA):
Prasanth, R. (2004). *Photonic switching in III/V nanostructures*. [Phd Thesis 2 (Research NOT TU/e / Graduation TU/e), Applied Physics and Science Education]. Technische Universiteit Eindhoven.
https://doi.org/10.6100/IR575061

DOI:
10.6100/IR575061

Document status and date:
Published: 01/01/2004

Document Version:
Publisher's PDF, also known as Version of Record (includes final page, issue and volume numbers)

Please check the document version of this publication:

• A submitted manuscript is the version of the article upon submission and before peer-review. There can be important differences between the submitted version and the official published version of record. People interested in the research are advised to contact the author for the final version of the publication, or visit the DOI to the publisher's website.
• The final author version and the galley proof are versions of the publication after peer review.
• The final published version features the final layout of the paper including the volume, issue and page numbers.

Link to publication

General rights
Copyright and moral rights for the publications made accessible in the public portal are retained by the authors and/or other copyright owners and it is a condition of accessing publications that users recognise and abide by the legal requirements associated with these rights.

- Users may download and print one copy of any publication from the public portal for the purpose of private study or research.
- You may not further distribute the material or use it for any profit-making activity or commercial gain
- You may freely distribute the URL identifying the publication in the public portal.

If the publication is distributed under the terms of Article 25fa of the Dutch Copyright Act, indicated by the "Taverne" license above, please follow below link for the End User Agreement:

www.tue.nl/taverne

Take down policy
If you believe that this document breaches copyright please contact us at:

openaccess@tue.nl

providing details and we will investigate your claim.

Download date: 16. Nov. 2023

Photonic switching in III/V nanostructures

R. Prasanth

Druk: Universiteitsdrukkerij Technische Universiteit Eindhoven

CIP-DATA LIBRARY TECHNISCHE UNIVERSITEIT EINDHOVEN

Prasanth, Ravindran

Photonic switching in III/V nanostructures / by R. Prasanth. – Eindhoven: Technische Universiteit Eindhoven 2004. – Proefschrift
ISBN 90-386-1895-6
NUR 926
Subject headings: semiconductors; nanostructures; photonic switching; quantum dots; quantum wells; all-optical switching; Stark effect
Trefwoorden: halfgeleiders, nanostructuren, optisch schakelen, quantumputstructuren

The work described in this dissertation was carried out at the COBRA Inter-University Research Institute on Communication Technology within the Department of Applied Physics of the Eindhoven University of Technology. The research has been supported by the "Netherlands organization for international cooperation in higher education" (NUFFIC) within the framework of the "Joint financing program for cooperation in Higher Education (MHO)".

Photonic switching in III/V nanostructures

PROEFSCHRIFT

ter verkrijging van de graad van doctor aan de
Technische Universiteit Eindhoven, op gezag van
de Rector Magnificus, prof.dr. R.A. van Santen,
voor een commissie aangewezen door het College
voor Promoties in het openbaar te verdedigen op
woensdag 12 mei 2004 om 16.00 uur

door

Prasanth Ravindran

geboren te Eravipuram, India

Dit proefschrift is goedgekeurd door de promotoren:

prof.Dr. J.H. Wolter
en
prof.dr. V.P.N. Nampoori

Copromotor:
dr. J.E.M. Haverkort

Dedicated to my teachers

എന്റെ ഗുരുനാഥൻമാർക്കു സമർപ്പണം

Contents

1. **Switching in optical communication**

2. **Theory of electro-refraction in nanostructures**

3. **An ultra short Mach-Zehnder Interferometric (MZI) space switch based on a composite quantum well**

4. Electro-refraction in quantum dots

5. All-Optical switching in quantum dots

Chapter 1

Switching in optical communication

“ *Light brings us the news of the Universe”*
Sir William Bragg

1.1 Introduction

Glass fibers are known from the time of Roman civilization. The history of modern fiber optics communication, however, starts with two Nature papers [1], one by the Dutch scientist Abraham van Heel and the other by Harold Hopkins and Narinder Kapani. In these two papers, optical fiber contains a transparent layer of low refractive index that confines the light and protects the surface of the fiber from contamination. These two properties make the fiber capable for transmitting optical signals with low loss. After the invention of semiconductor lasers, the optical communication field progressed rapidly. In 1961, Bernard et.al [2] predicted laser emission from direct inter-band transitions in InAs like semiconductors. In 1962, Hall et.al observed coherent light emission from a GaAs p-n junction. In 1963 Alferov patented his historic invention of semiconductor heterojunction lasers. He first observed lasing in an AlGaAs-GaAs double heterostructure [3]. In 1970 Kapron [4] demonstrated the first glass optical fiber for the low-loss (20 dB/km) transmission of signals in the 1.5 μm wavelength region. In 1986 Kanamori [5] showed that, for this wavelength region, the attenuation in a pure silica-core single mode fiber can even be as low as 0.154 dB/km. With these two basic elements, the optical fiber and the semiconductor laser, now the trans-Atlantic-trans-Pacific global communication cables connect almost all countries of the five continents.

In order to satisfy the increasing global demand we need, not only high bandwidth communication fibers, but also fast, compact, low switching energy and polarization independent switches, modulators and amplifiers. To this end the technology must be improved. Compact space switches are an essential part of such cost effective and reliable communication networks. Highly nonlinear optical materials are required for making the space switches as compact as possible. The large optical nonlinearity of quantum dots and quantum wells, make them attractive structures for designing compact electro-refractive switches as well as all-optical switches.

This thesis investigates the large optical nonlinearities of these semiconductor structures and how these nonlinearities can effectively be exploited for optical switching. We investigate the potential of combining the Quantum Confined Stark Effect (QCSE) and the carrier depletion effect for optimizing the electro-refraction. The thesis also focuses on our experimental investigation of wavelength independent all-optical switching in an inhomogeneous array of quantum dots. The goal of our research is to design an efficient material for all-optical switching. Many researchers studied optical switching in bulk and quantum well materials. Only very few reports has been published on switches based on quantum dots.

1.2 Optical communication networks

In principle, the increasing demand for telecommunication services can be achieved by installing more fiber cables. However, this simple method will increase the cost exponentially. A better alternative is to make use of the huge available optical bandwidth in the fiber [6]. Different multiplexing schemes have been suggested [7] for exploiting the allowed bandwidth in the 1.55 μm communication window. In optical time division multiplexing (OTDM) [8] technique, many low speed data streams can be multiplexed into a high-speed data stream. As long as the data pulses in OTDM are still in the picosecond time domain preventing excessive problems with fiber dispersion, this scheme will allow only a limited part of the wavelength region to be exploited. By allowing many different wavelength channels in the same fiber, this limitation will be overcome. This technique is called wavelength division multiplexing (WDM) [9]. A more critical version of WDM enabling the capacity expansion of fiber optics system is Dense Wavelength Division Multiplexing (DWDM). In this scheme the multiplexed frequencies are closely separated. These high bit rate and multi-wavelength channel signals now have to be sorted out, and possibly also have to be routed at the nodes of the network.

The wavelength routing is achieved with add-drop multiplexers and cross-connects [10]. Most of the communication nodes in optical networks are electro-optical and hence need *optical-to-electronic-to-optical (OEO)* conversion. However, these OEO conversions are slow and require an expensive Distributed Feedback (DFB) laser for the EO conversion. In optical nodes, the OEO conversion can be completely removed. Both optical cross-connects and add-drop demultiplexers require demultiplexing, switching and again multiplexing [11]. By integrating these components, the number of fiber-chip coupling can be drastically reduced, which should also decrease the cost and increase the performance. However, compact polarization independent space switches in planar technology still form a major obstacle towards the realization of these integrated chips [12].

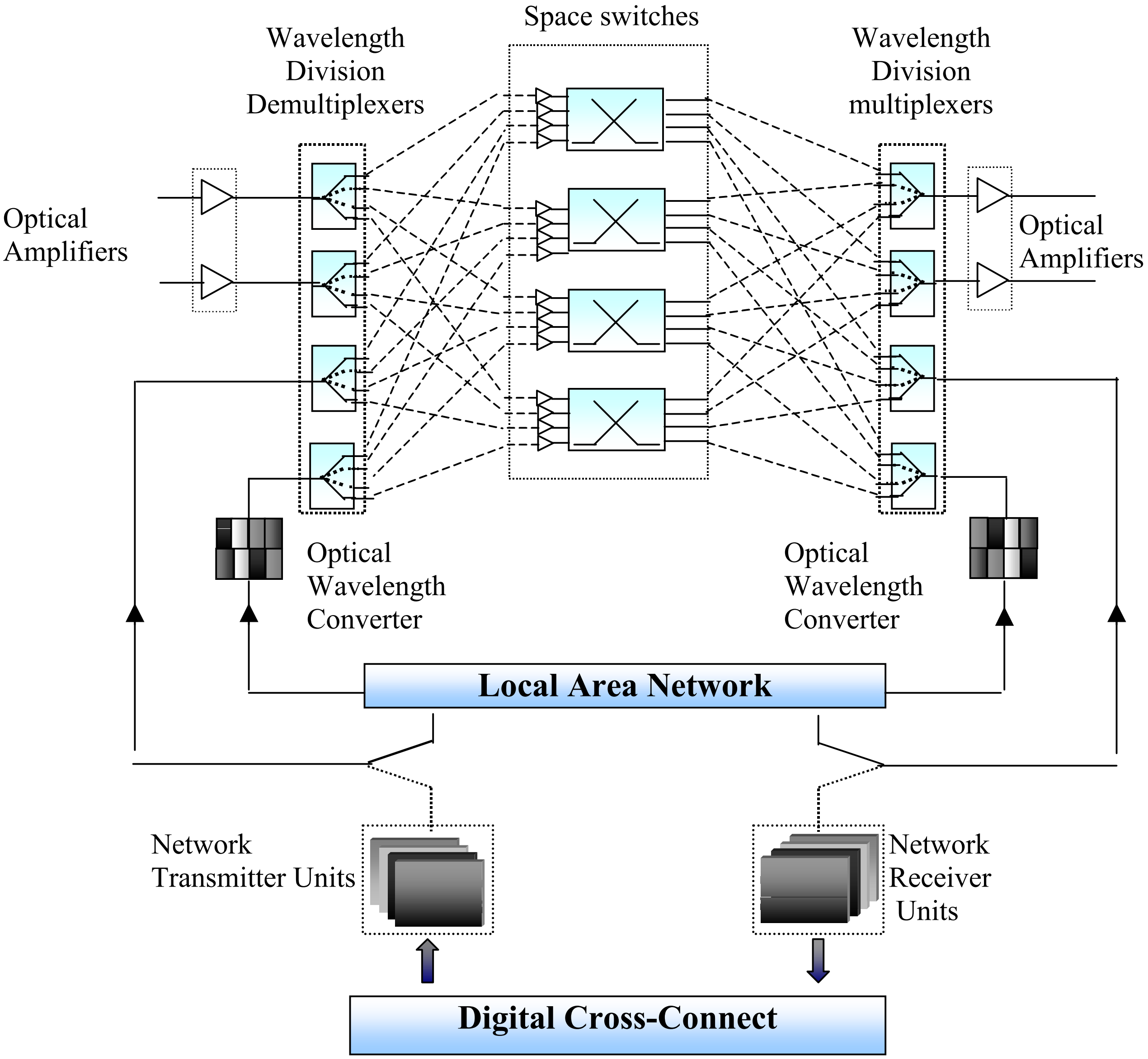

Figure 1.1: Schematic diagram of all-optical communication crossconnect

1.3 Optical switching

We employ a Mach-Zehnder Interferometric space switch (MZI) as a testing device to measure the electro-refraction and all-optical nonlinearity of the semiconductor quantum wells and quantum dots.

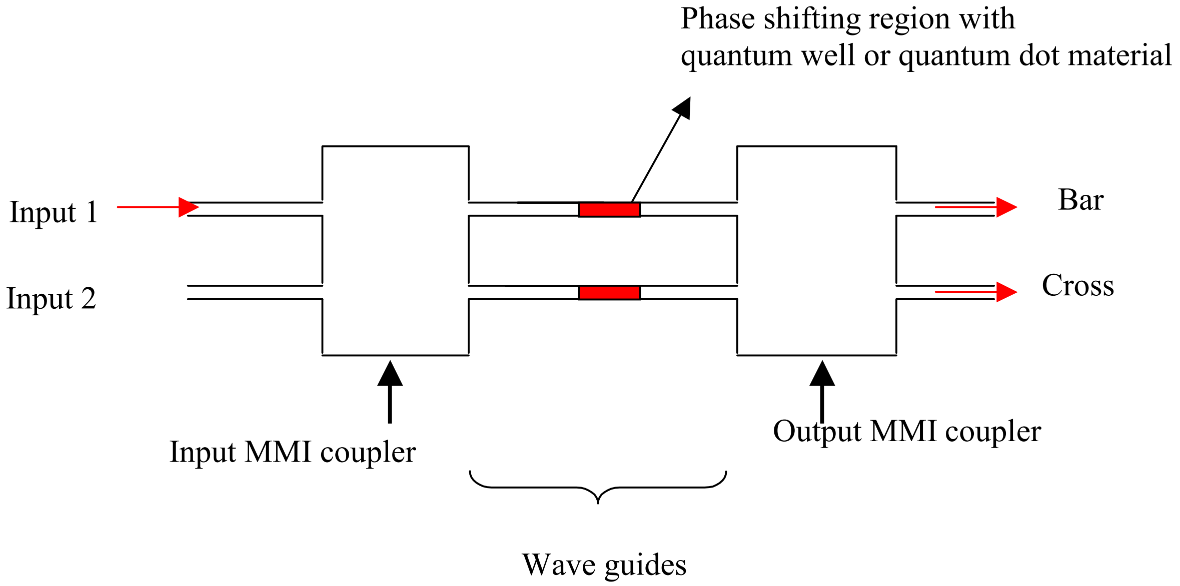

Figure 1.2: Mach-Zehnder interferometric space switch

Many of these switching characteristics are determined by material properties. The requirements for photonic switch are

1. *Polarization independence*: The input signals have random polarization properties. To re-direct this entire signal through the different output channels, the switches must have a polarization independent performance [12]. In our studies, we intentionally incorporate strain to achieve polarization insensitive switching
2. *Low crosstalk*: Crosstalk between different output channels leads to mixing up of the signals. The bit error rate will exponentially grow with network size [13]. Crosstalk penalty is an important design criterion in optimizing the electro-refraction in the material. Crosstalk is mainly generated by imperfections in the processing. From the material point of view, the electro-absorption within the MZI also introduces crosstalk. We therefore investigate the electro-refraction at a wavelength sufficiently below the bandgap, so that the electro-absorption and thus the crosstalk also remain acceptable.

3. *Low insertion loss:* The absorption inside the switching medium is a parasitic effect. The insertion loss in the connecting waveguides of a photonic integrated chip should be kept as low as possible. Assuming that the active material of the space switch is the same as the material comprising the waveguide core, one requires that the absorption loss in the active material also remains extremely low. In our calculations we detuned the operating wavelength sufficiently outside the Urbach tail of the absorption spectrum to keep the absorption loss below 0.5 dB/cm
4. *Wavelength independence:* Optical communication employs the low loss (absorption and scattering loss) window around 1.55 μm. WDM intrinsically implies that one uses a large wavelength window. Generally the refractive index variation is wavelength dependent in all materials. To make the performance of the switch as wavelength insensitive as possible, a proper design of the active semiconductor material is required. In our opinion the broad inhomogeneous distribution of quantum dots can assist in achieving wavelength independent switching.
5. *High bit rate packet switching:* Optical packet switching requires high speed switching. All-optical switching is the most promising technique to achieve switching at Terabit/s rate. The switches based on QCSE are limited by the RC time constant of the device [14]. Traveling wave designs allow switching speeds above 40 Gbits/s. Finally, the bandfilling effect will reduce the speed of the switch due to the large carrier decay time. Externally applied electric fields, however, speed up the carrier emission out of a quantum well or quantum dot into the picosecond time regime.
6. *Scalability:* The integrated chip consists of many devices. To restrict the on-chip propagation losses, and to integrate many devices on a single chip, the individual components must be as small as possible. Large scalability enables integration of many components on a single chip. Compared to semiconductor optical amplifiers and lasers, space switches are lengthy. A compact space switch requires an efficient and short phase shifting section and thus a large electro-refraction or a large optical nonlinearity.
7. *Low voltage:* High frequency application requires low switching voltage, typically below 2V. The increased optical non-linearity in low-dimensional semiconductor structures might provide an opportunity to reduce the operating voltage bellow 2V.

1.4 Switching principles

The principle of switching is based on the refraction of light in the material medium or alternatively on an interferometer effect. In the latter case, a change in the refractive index in the path of the light within the interferometer can direct it into a different output optical path. Several switching methods have been suggested.

1.4.1 Micro-Electro-Mechanical systems (MEMs)

In the past few years MEMs have emerged as a new technology for optical switching. The switches are fabricated by micro machining [15]. The mirrors are arranged in two-dimensional arrays and have very good scalability up to 1000x1000. The structures range in dimensions from a few hundred microns to a millimeter. These are mechanical devices, which steer the mirrors to deflect the light properly. They are either in the ON position to reflect light or in the OFF position to allow the uninterrupted passage of light, thus avoiding any crosstalk. The disadvantage of MEMs is their limited switching speed, which prevents their use in optical packet switching. MEMs also require a complicated 3-D fabrication technology, which does not fit in a planar technology. Reliability of MEMs in telecommunication applications has still to be proven.

1.4.2 Thermo-optic switches

Thermo-optic switches are based on the refractive index variation in a material due to temperature variations. Basically thermo-optic switches are of two different types; interferometric switches [16] and digital optical switches [17]. Scalability is relatively high. The factor limiting the speed of such switch normally depends on the cooling properties of the material. Usually, the switching speed is below a few kHz, which is too low for packet switching. Repeated heating and cooling limits the life of the switch [18].

1.4.3. Semiconductor optical amplifier (SOA) switch

SOA-based switches are promising candidates for all-optical switching. Semiconductor optical amplifiers have been grown in the arms of Mach-Zehnder interferometer or inside an optical nonlinear loop device. Low energy control pulse and high power data pulse could be achieved due to the gain in a SOA [19]. At the same time the gain dynamics lead to complicated switching characteristics and transmission characteristics. An SOA based MZI easily suffers from imbalance between both arms when the optical gain in both SOAs is not equal, resulting in crosstalk. In some designs, both SOA's and a thermo-optic phase shifter are included in the arms of the MZI to avoid this problem. Amplified spontaneous emission noise and heat dissipation are problems of SOA based switches.

1.4.4 Electro-optic switches

Electro-optic switches are usually based on the Pockels effect, on the Quantum Confined Stark Effect or on the carrier depletion effect. If an electric field is applied to a crystal, which lacks center of symmetry, the crystal will become birefringent. This effect is called the Pockels effect, and is linear with the applied electric field. In the Kerr effect, on the other hand, the birefringence is proportional to the square of the electric field. The response time of the refractive index variations due to these effects are in the range of 10^{-14} to 10^{-13} seconds. However, the RC time constant of the device usually limits the switching speed to picoseconds [14]. To increase the electro-refraction and electro-absorption, quantum wells have been applied. These structures show a red shift of the inter-band transition with applied field. This effect is called the Quantum Confined Stark Effect (QCSE), which is considerably enhanced by excitonic effects. Alternatively, refractive index variations are induced by carrier depletion. The carrier depletion effect is somewhat more efficient than the QCSE, but it is of nanosecond speed due to the slow carrier recombination dynamics.

1.5 Optical switching based on the QCSE

Chemla et.al [20] first reported a large Stark shift of the effective bandgap when an electric field was applied to a quantum well. He named this effect the Quantum Confined Stark Effect (QCSE). Compared to the Franz-Keldysh effect in a bulk semiconductor, the electrons and holes remain confined inside the quantum well or quantum dot, even at an applied electric field as high as 200-300 kV/cm, which implies that the transition matrix elements remain large. In bulk materials, the electric field ionizes the exciton, whereas in low dimensional structures, the excitonic enhancement can be observed for electric fields up to 200-300 kV/cm.

With respect to electro-absorption, the QCSE results in two effects [21]. The electric field shifts the envelope wave functions within the quantum well into opposite directions and hence the oscillator strength decreases. The second effect is a bandgap reduction due to the triangular confinement potential in the presence of an applied electric field. This is schematically indicated in figure 1.3. The reduction in bandgap produces a positive refractive index variation whereas the reduction in oscillator strength produces a negative change [22]. Consequently, the electro-refraction due to QCSE is small, since both contributions partly cancel.

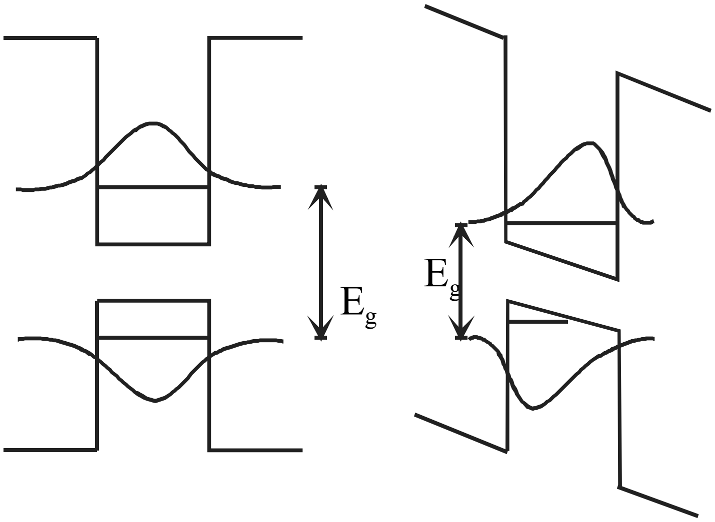

Figure 1.3: Schematic diagram of the Quantum Confined Stark Effect showing the effective bandgap in a quantum well without (left) and with (right) applied electric field

The carrier depletion effect is mainly based on the bandfilling effect [23], which produces a blue shift of the absorption spectrum because the ground state absorption becomes transparent. On the other hand, carrier-carrier interaction produces a bandgap renormalization, which counteracts the blue shift due to bandfilling. Bandfilling is always accompanied with free carrier absorption, which produces a small refractive index variation in the 1.55 μm wavelength window. The bandfilling effect in general produces a larger electro-refraction compared to the QCSE. However, in the case of bandfilling, the unavoidable free carrier absorption produces a significant absorption loss. In our calculations, the carrier concentration was taken such that the level of free carrier absorption loss was acceptable (<-30dB). In addition, in the case of bandfilling, the switching speed slows down due to the nanosecond carrier recombination time. When one uses the electro-refraction in a waveguide based space switch, one cannot employ the peak value of electro-refraction, since around the peak the absorption loss is also huge. One must thus detune the operating wavelength away from the peak in order to keep the electro-absorption in the acceptable range. The Urbach tail of the absorption edge governs the material losses in the quantum well and quantum dot. For realizing a low waveguide propagation loss, the spectral spacing between the bandgap and the operating wavelength must be made comparatively large (50-100 meV).

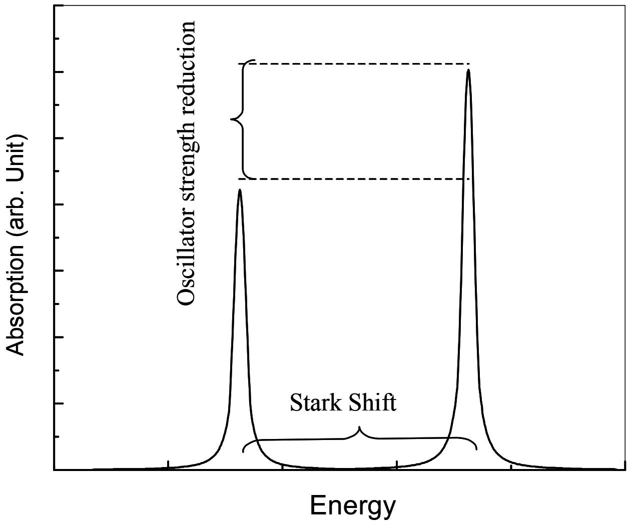

Figure 1.4: Schematic picture of the changes in the absorption spectrum due to the QCSE. The change in the peak height reflects the oscillator strength reduction. The shift in the peak energy reflects the Stark shift.

Maat et.al [24] studied electro-optic switches in bulk quaternary InGaAsP, doped up to $6.10^{17}/cm^2$, in which they incorporated the Pockels effect in combination with the carrier depletion effect. However, contrary to low dimensional structures, in bulk material, the electrical field induced refractive index variation is quite small. Moreover, the doping, which increases the electro-refraction has the disadvantage that the switching speed reduces.

Quantum wells are a good alternative for an enhanced electro-optic effect and for fast switching. Zucker et.al [25] measured the electro-refraction in InGaAs/InP quantum wells. She found that the refractive index variation per applied electric field in these quantum wells is 19 times larger than in bulk InP. Apling et.al [26] calculated an electro-refraction of $1.3.10^{-4}$ in bulk InGaAsP (Q=1.03 eV) at wavelength of 1.55 µm at 400 kV/cm. However, the electro-absorption at this wavelength is more than 30/cm, which is much too high for application in waveguide devices.

In InGaAs/InP quantum well materials, the required large spectral spacing between the 1.55 µm operating wavelength and the bandgap leads to a narrow well width. However the QCSE strongly decreases with decreasing well width. Several methods have been suggested to overcome this constraint, including quaternary InGaAsP/InP QWs [27] and coupled QWs [28]. Dorren et.al [28] studied a chopped InGaAs/InP quantum well, in which the three coupled quantum wells produce a large QCSE at 1.55 µm and hence enhanced the electro-refraction to 2.10^{-4} at 0.2 dB/cm waveguide absorption loss. We further study in Chapter III an asymmetric InGaAs/InP/InAsP coupled quantum well, which provide a third possibility for combining a large QCSE with an operating wavelength of 1.55 µm. This coupled quantum well is indirect in real space and provides a large linear QCSE, which was experimentally verified by Silov et.al. [29]. In Chapter III, we present an enhanced electro-refraction due to the QCSE of $7.8.10^{-4}$ in this structure.

For producing an enhanced electro-refraction in quantum well material, we also combined the Quantum Confined Stark effect and the carrier depletion effect. Both these effects produce a red shift of the absorption spectrum. The combination of these two effects is exploited in reducing the phase shifting region that we explained in Chapter III. In this material, the carrier depletion effect at a doping level of $2.10^{11}/\text{cm}^2$ produces an additional (2.6 times) enhancement of the total electro-refraction (Δn) at an absorption loss of 0.5 dB/cm. Finally, for achieving polarization independent behavior, we must also carefully adjust the amount of strain, which will however also further reduce the design freedom.

In our opinion, quantum dot material is a more promising candidate for electro-refraction due to the following reason. Firstly, the density of states of the QD material is confined into a set of discrete absorption peaks with large peak absorption. Secondly, when applying an electric field, the discrete energy levels in quantum dots will be shifted from a region with high peak absorption towards a region with initially zero absorption. The peculiar behavior in a QD is also reflected by a large electro-refraction. Our calculations in Chapter IV for an InAs pyramidal quantum dots show an increase in the peak electro-refraction by 35 times, compared to the corresponding value in quantum well material. In the wing of the absorption spectrum, at a 0.15

dB/cm residual absorption loss, the electro-refraction is still as large as $1.2.10^{-2}$, indicating the potential of quantum dots for optical switching.

Finally, Aizawa et.al [30] reported a 7% peak refractive index variation at 80 kV/cm applied electric field in a five layer GaInAs/InP etched quantum box (the quantum dots etched in box shape) structure at a wavelength of 1.52 μm. In this experiment, the electro-absorption was quoted to be too small to be observed. This value is about 35 times larger than the electro-refraction in InGaAs/InP quantum well as measured by Zucker et.al. This huge electro-refraction has been largely ignored during the last decade. These values however are in very good agreement with our theoretical calculations, which will be presented in Chapter IV.

1.6 Quantum dots

Quantum dots are a physical realization of a truly 3-dimensional quantum confined system, which has atomic-like properties and is therefore sometimes called an “artificial atom”. In quantum dots, electrons and holes are confined in all the three orthogonal directions. When the characteristic dimension of such a system is less than the Broglie wavelength of the carriers, the energy levels become completely discrete, leading to a Kronecker delta like density of states [31,32]. The optical transitions in such an “artificial atom” depend on the coupling between the electron and hole envelope functions and thus on the spatial distribution of the carriers inside the dot.

The experimental realization of semiconductor quantum dots, made up of a cluster of 10^3-10^4 atoms, opens new possibilities of bandgap engineering at the nanometer scale. [33-36]. Quantum dots were initially fabricated using electron beam lithography and dry etching [37], but the optical properties of these etched QDs remained poor due to excessive nonradiative recombination at the sidewalls. Nowadays, QDs are mainly fabricated by self-assembled growth using modern epitaxial growth technologies like MBE, CBE and MOCVD [38]. The growth of thin layers of highly strained materials slightly above the critical layer thickness results in strain relaxation and subsequent “self-assembled” island formation. The optical properties of these self-assembled dots can be controlled up to a certain extent by clever design and by adjusting the growth parameters. The growth mechanism is further explained in Chapter V. For our studies presented in Chapter V, we used InAs/InP self-assembled quantum dots grown by CBE. For device applications, highly precise, densely packed quantum dots with good optical quality are presently being developed in different laboratories around the world.

Different spectroscopic methods are employed for characterizing the size, shape and quality of the dots. The photoluminescence (PL), photoluminescence excitation (PLE) spectra and the X-ray diffraction measurement routinely provides the composition and dimension of the quantum wells. Atomic Force Microscopy (AFM) gives the density, the spatial distribution and the dimension of the quantum dots.

1.6.1 Optical non-linearities in quantum dots

The truly 3-dimensional optical confinement and the resulting modification of the physical properties of quantum dots attracted many researchers to this field. Numerous groups reported sharp atomic like spectra due to the strong confinement of excitons in quantum dots [31, 32, 39]. In addition, the modifications of the density of states in quantum dots immediately triggered device engineers to exploit these properties in quantum dot amplifiers and lasers, in infrared detectors and spintronic devices. In comparison to the efforts in these fields, a relatively limited amount of work have been devoted towards the applicability of quantum dots for optical switches and memories [40,41]. The optical non-linearities in quantum dots are strongly modified due to the strong confinement of the electron and hole states inside the dot [31,32]. The resulting discrete energy levels can easily be perturbed by injecting charge carriers occupying these discrete states and causing state-filling. Alternatively, the discrete energy levels can be shifted by applying an electric field.

The shape and size of the quantum dots can strongly influence the optical non-linearity. In a cubic quantum dot, many states are degenerate, while quantum dots of arbitrary shape lift the degeneracy. When the size of the dot is reduced, the separation between the levels increases, and strongly influences the bandfilling dynamics [42] as well as the QCSE through the amount of carrier confinement. These changes influence the optical non-linearities in quantum dots. Hence for an optimization of the electro-refraction, we considered the quantum dot density, the dot size and its shape.

Electron-hole pairs in III/V semiconductors form shallow (Wannier) excitons with an exciton binding energy which increases from 4 meV in bulk GaAs towards 30 meV for strongly confined quantum dots. This is further explained in Chapter 2. The existence of bi-excitons

[43,44] and tri-excitons is another source of enhanced all-optical non-linearities in quantum dots, since the addition of one single electron-hole pair is known to annihilate one PL-line, while creating another line at a slightly smaller transition energy. The formation of multiple excitons thus produce a red shift of the absorption spectrum, which is related to the bandgap renormalization in bulk or quantum well materials and which is schematically indicated in Fig. 1.5. It is a big advantage of quantum dots that, in principle, they require a very low injected carrier density for obtaining state-filling. One electron-hole pair will already produce optical transparency, while two electron-hole pairs produce optical gain. Few carriers are thus able to produce a large optical nonlinearity, indicating that a very low switching energy might be achievable.

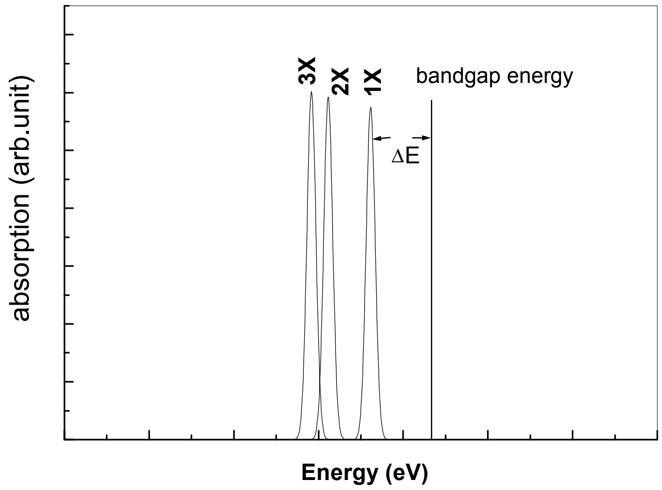

Figure. 1.5: Schematic diagram of the transition energy shift due to exciton (1X), bi-exciton (2X) and tri-exciton (3X) recombinations.

For the device application of quantum dots, including all non-resonant all-optical switching applications, the carrier relaxation within a quantum dot should be as fast as possible. Early calculations of the carrier relaxation rates in quantum dots predicted a phonon bottleneck [45] due to three-dimensional confinement in a quantum dot. The resulting delta function like density of states was predicted to cause blocking of optical phonon emission if the optical phonon energy is not equal to the inter-subband spacing. However, the mere existence of quantum dot lasers proves that such a phonon bottleneck does not exist in practice. Different explanations have been proposed, including Auger scattering is be important at high carrier density as well as lifetime broadening of the hole levels inside the quantum dot in combination with fast electron relaxation through electron-hole scattering. A third important ingredient is that due to non-adiabaticity, there is a strong enhancement of the phonon assisted optical transitions in quantum dots as reported by Fomin and Devreese [46-48]. This strongly increases the number of possible relaxation paths. As a result there is no phonon bottleneck, which could provide any obstacle for device applications.

The optical nonlinearities in quantum dots are proportional to the exciton oscillator strength. The oscillator strength is determined by the spatial extent of the center-of-mass wavefunction. In bulk or quantum well material, the oscillator strength is thus proportional to V/a_0^3, with a_0 the Bohr radius in the bulk. The bulk oscillator strength per unit volume is thus constant. Schmitt-Rink et.al [49] were the first to study the nonlinear optical properties of III/V microcrystallites. They theoretically derived that the strength of the QD absorption peak is enhanced by a factor of a_0^3/V, compared to the bulk material, with a_0 the Bohr radius in the bulk and V the volume of the dot. This is the "giant oscillator strength" which was first reported for bound excitons by Rashba and Gurgenishvili [50] and can be understood by the fact that the center-of-mass wavefunction for a bound exciton is less localized. Schmitt-Rink et.al [49] argue that the Coulombic electron-hole interaction only marginally influences the eigenfunctions of the electrons and holes. Hence, the Coulomb interaction leads to only a small renormalization of the oscillator strength as well as to a small red shift of the transition energy. Banyai et.al [51] evaluated the third order optical nonlinearities in microstructures. These authors also suggested semiconductor materials with large Bohr radius for a strong optical nonlinearity. Andreani et.al. [52] provide a plot of the exciton oscillator strength localized to a monolayer flat island in a quantum well. They observe an increasing oscillator strength for both small islands as for large monolayer flat islands. For small islands, the oscillator strength increases since the exciton spreads out beyond the island, as in the "giant oscillator strength" case, whereas the oscillator strength again increases for large islands since the extent of the center-of-mass wavefunction increases. The second case has been treated by Gotoh and Ando [53]. They calculated the excitonic absorption spectra in quantum boxes. They showed that the Coulomb enhancement factor, which is the enhancement of the oscillator strength by the Coulomb attraction, is mainly concentrated to the lowest exciton transition. Moreover, the Coulomb enhancement factor is shown to substantially increase with dot size, up to dot sizes five times larger than the exciton Bohr radius. These authors say that their theoretical result is again consistent with the “giant oscillator strength” picture, where the center-of-mass of an exciton becomes weakly bound in a wide region. We comment that increasing oscillator strength for large quantum dots is consistent with the argument that the oscillator strength is proportional to the spatial extent of the center-of-mass wavefunction. Another important requirement for optical nonlinearities is the stability of the exciton up to room temperature. The stability of the electron-hole pair recombination inside a quantum dot is found to be considerably higher than in a quantum well. Wang et.al [54] experimentally observed a two times enhancement in the onset energy for thermal quenching of the integrated photoluminescence intensity in high quality InGaAs/GaAs dots as compared to a reference quantum well. The nonlinear optical properties of single quantum dots have been reported by Bonadeo et.al. [55]. These authors show that the dominant optical nonlinearity is due to state-filling which saturates the oscillator strength, while they observed no frequency shift or broadening due to other many body effects.

For achieving fast all-optical switching, the time dependence of the optical nonlinearities is very important. For quantum dots large enough that the oscillator strength is proportional to the volume of the quantum dot, the radiative lifetime becomes inversely proportional to the volume of the quantum dot. Experimental investigations of the quantum dot radiative lifetime report an enhanced exciton lifetime, especially for quantum dots with a small volume. Wang et.al [54] measured a two times enhancement in excitonic life time as compared to a reference quantum well at 1.4 K. Kano et.al measured an increase of the lifetime from 260 to 422 ps if the lateral width of GaAs/AlGaAs quantum wire changes from 25 to 7 nm. Sugawara [56] theoretically modeled these experimental investigations using quantum disk geometry and found an increasing spontaneous emission lifetime as a function of the strength of the lateral confinement potential. Sugawara points out that the spontaneous lifetime increases for small quantum dots since spontaneous emission is prohibited when the wavevector of the exciton center-off-mass motion exceeds $q_c=\omega n/c$, the wavevector of the emitted photon. Fortunately, the exciton lifetime at room temperature is only partly determined by the radiative lifetime. Carrier emission out of the quantum dots and successive non-radiative recombination in the barrier, or even direct non-radiative recombination inside the quantum dot will seriously reduce the total lifetime.

Differential pump-probe transmission measurement at room temperature by Birkedal et.al [57] observed a bleaching decay time of 65 ps in high quality InAs dots. They attributed this effect to carrier emission out of the quantum dot. Nakamura et.al. [58] measured the absorption recovery time in a sample with ten layers of stacked InAs/GaAs dots by means of transient absorption measurement. He found an absorption recovery time of 55 ps at room temperature. Bogaart et.al. [59] find the room temperature bleaching decay times to increase from 80 ps at low wavelength to 220 ps at high wavelength. The observed variation of the bleaching decay time is interpreted [59] as being primarily due to carrier emission at low wavelength arising due to nonradiative recombination at higher wavelength. A more significant increase of the switching speed can be realized by employing techniques like four wave mixing or other coherent effects, which profit from the 260 fs dephasing time at room temperature. This was measured by Borri et.al [60]. However, in our case we need only very low switching energy since the necessary optical nonlinearities are produced by bandfilling.

1.7 Scope of the thesis

This thesis investigates the possibilities of optimizing the phase shifting region in a 2x2 Mach-Zehnder interferometric space switch, starting from a fundamental understanding of the optical properties of quantum wells and quantum dots. We first established a theoretical base for these studies by developing a model for band gap engineering of the above-mentioned nano-structures. We compare the model with different theoretical and experimental predictions. We also present an experimental investigation of the carrier induced refractive index variation in quantum dots by optical pumping. These are employed in a fast and compact all optical switch.

Chapter 2 explains the basic theory of band structure in quantum wells and quantum dots. Our theoretical model is based on the 4x4 Luttinger-Kohn Hamiltonian. We use an expansion in terms of plane wave solutions for obtaining the eigenstates and eigenvectors of this Hamiltonian. The electro-absorption and electro-refraction properties of quantum wells and quantum dots, as well as their polarization dependence are also discussed.

In Chapter 3 we deal with the optical properties of InGaAs/InAsP/InP quantum wells. We investigate an InGaAs/InAsP composite quantum well in which band filling effect and the Quantum Confined Stark Effect are combined to obtain an ultra-short phase shifting region.

Chapter 4 investigates the geometrical dependence of the Quantum Confined Stark Effect in quantum dots. The electro-refraction in both InAs/InP and InAs/GaAs quantum dots is investigated. In this Chapter, we also discuss the potential of quantum dots for photonic switching applications.

Finally, in Chapter 5, we present all-optical switching due to state filling in quantum dots. The InAs/InP quantum dot are embedded in a waveguide structure. Subsequently, a Mach-Zehnder interferometric switch was lithographically etched on the above-mentioned structure. We observe all-optical switching by exciting one of the arms of the MZI. We finally show that the switching energy is as low as 6 fJ.

References

1. " A new method of transporting optical images without aberration", A.C.S. van Heel, Nature 173, pp 39, 1954, "A flexible fiberscope using static scanning", H.H. Hopkins and N.S. Kapani, Nature, 173, pp 39-41, 1954, "Fiber Optics", Narinder Kapani, Scientific American, vol. 203 (5), pp 72-81, 1960
2. "Laser Conditions in Semiconductors", M.G.A. Bernard and G. Duraffourg, Phys. Status. Solidi, vol. 1, pp 699-703,1961
3. "The history and future of semiconductor heterostructures from the point of view of a Russian scientist", Zh.I. Alferov, Physica Scripta, vol. T68, pp 32-45, 1996
4. "Radiation losses in glass optical waveguides" Conf.on Trunk telecommunications by guided waves, F.P. Kapron, IEE Conf.Publ. vol. 71, pp 148-153, London 1970
5. "Transmission characteristics and reliability of pure silica core single mode fibers", H. Kanamori, J. Light wave Tech., vol. LT-4, pp 1144-1150, 1986
6. "The use of fiber optics in cable communications network", J.A. Chinddix, J.A. Vaughan, W. Wolfe, J. Lightwave Tech., vol.11, pp 154-166, 1993
7. ."Photonics transport Network OAM Technologies" K. Sato, IEEE Communication mag. vol. 34, pp 86-94, 1996
8. "100 Gb/s optical time-division multiplexed networks" S.A. Hamilton, B.S. Robinson, T.E. Murphy, S.J. Savage, E.P. Ippen, J. Lightwave. Tech., vol 20, pp2086- 2100, 2002
9. ." A wideband all optical WDM network", I.P. Kaminow, C.R. Doerr, C. Dragone, T. Koch, U. Koren, A.A. M. Saleh, A.J. Kirby, C.M. Ozveren, B. Schofield, R.E. Thomas, R.A. Barry, D.M. Castagnozzi, V.W.S. Chan, B.R. Hemenway, D. Marquis, S.A. Parikh, M.L. Stevens, E.A. Swanson, S.G. Finn, R.G. Gallager, J. Selected areas in Communications, vol. 14, pp 780-799, 1996
10. "Optical cross connect system in broad-band networks: system concept and demonstrators description", S. Johansson, M. Lindblom, P. Granetstrand, B. Lagerstrom, L. Thylen, J. Lightwave. Tech, vol. 11, pp 688-694, 1993
11. "Linear Light wave network: Performance issues", T.E. Stern, K. Bala, S. Jiang, J. Sharoni, J. Lightwave. Tech., vol. 11, pp 962-970,1993

12. ”Integrated-optic versus microscopic devices for fiber optic telecommunication systems: a comparison”, E. Pennings, G.D. Khoe, M.K. Smit and T. Staring, IEEE J.of Selected topics in Quantum.Electron., vol. 2, pp 151-164, 1996
13. **“**Crosstalk in multiwavelength optical cross-connect networks” J. Zhou; R. Cadeddu, E. Casaccia, C. Cavazzoni, M.J. O'Mahony, J. Lightwave. Technol., vol. 14, pp 1423-1435, 1996
14. “Analysis of the device performance of quantum interference transistors utilizing ultra small semiconductor T structures”, S. Subramaniam, S. Bandyopadhyay, W. Porod, J. Appl. Phys., vol. 68, pp 4861-4870, 1990
15. ”All silicon Bistable micromechanical fiber switch based on advanced Bulk micromachining”, M. Hoffmann, P. Kopka, E. Voges, J. Selected topics in Quantum.Electron., vol. 5, pp 46-51, 1999
16. “Fibre-optic interferometer tunable switch using the thermo-optic effect”, A.C. Boucouvalas, G. Georgion, Electron. Lett., vol. 21, pp 512-514, 1985
17. “Very low crosstalk 1X2 digital optical switch integrated with variable optical attenuators”, M.S. Yang, Y.O. Noh, Y.H. Won, W.Y. Hwang, Electron. Lett., vol. 37, pp 587-588, 2001
18. ”Low loss and high extinction ratio strictly non-blocking 16x16 thermo optic matrix switch on 6-in wafer using silica based planar lightwave circuit technology”, T. Goh, M. Yasu, K. Hattori, A. Himeno, M. Okuno, Y. Ohmori, J. Lightwave. Technol., vol. 19, pp 371-379, 2001
19. “Interferometric ultrafast SOA based optical switches: from devices to application”, R.J. Runser, Deyn-Zhon, C. Coldwell, B.C. Wang, P. Toliver, Kung-Li-Deng, I. Glesk, P.R. Prucnal, Optical and Quant. Electron., vol. 33, pp 841-874, 2001
20. “Electroabsorption by Stark effect on room-temperature excitons in GaAs/GaAlAs multiple quantum well structures”, D.S. Chemla, T.C. Damen, D.A.B. Miller, A.C. Gossard, W. Wiegmann, Appl. Phys. Lett., vol. 42, pp 864-866, 1983
21. “Electric-field dependence of linear optical properties in quantum well structure: Waveguide electroabsorption and sum rules”, D.A.B. Miller, J.S. Weiner, D.S. Chemla, IEEE. J. Quantum. Electron., vol. 22, pp 1816-1830, 1986

22. "Refractive index modulation based on excitonic effects in GaInAs-InP couple asymmetric quantum wells", C. Thirstrup, IEEE. J. Quantum. Electron., vol. 31, pp 988-996, 1995
23. "Many-body effects in the absorption, gain, and luminescence spectra of semiconductor quantum-well structures" S. Schimitt-Rink, C. Ell, H. Haug, Phy. Rev. B, vol. 33, pp 1183-1189, 1986
24. "Polarization-independent dilated InP-based space switch with low crosstalk", D.H.P. Maat, Y.C. Zhu, F.H. Groen, H. van Brug, H.J. Frankena, X.J.M. Leijtens, IEEE Photon.Technol.Lett, vol. 12, pp 284-286, 2000
25. "Novel hybrid optically bistable switch: The quantum well self-electro-optic effect device" D.A.B. Miller, D.S. Chemla, T.C. Damen, A.C. Gossard, W. Wiegmann, T.H. Wood, C.A. Burrus, Appl. Phys. Lett, vol. 45, pp 13-15, 1984
26. "Electrorefraction in GaAs and InGaAsP and its application to phase modulators", A. Apling, L.A. Coldren, J. Appl. Phys., vol. 61, 2430-2433, 1987
27. "Quarternary quantum wells for electro-optic intensity and phase modulation 1.3 µm and 1.55 µm", J.E. Zucker, I. Bar-Joseph, B.I. Miller, U. Koren, D.S. Chemla, Appl. Phys. Lett., vol. 54, pp 10-12, 1989
28. "A chopped quantum-well polarization-independent interferometric switch at 1.53µm" B.H.P. Dorren, A.Yu. Silov, D.M.H. Dukers, J.E.M. Haverkort, D.H.P. Maat, Y. Zhu, F.H. Groen and J.H. Wolter, IEEE J.Quantum. Electron., vol. 36, pp 317-324, 2000
29. "Blue stark shift in composite quantumwells",A.Yu. Silov, B. Aneeshkumar, M.R. Leys, B. Vonk, J.H. Wolter, Proc. 25th Int.Conf.Semiconductors Part I, pp 517-518, 2000
30. "Observation of field induced refractive index variation in quantum box structure", T. Aizawa, K. Shimomura, S. Arai, Y. Suematsu, Photon. Technol. Lett., vol. 3, pp 907-909, 1991
31. "Ultra narrow luminescence lines from single quantum dots" M. Grundman, J. Christen, N.N. Ledentsov, J. Bohrer, D. Bimberg, S.S. Ruvimov, P. Werner, U. Ritcher, U. Gosele, J. Heydenreich, V.M. Ustinov, A.Yu. Egorov, A.E. Shukov, P.S. Kop'ev and Zh.I. Alferov, Phys. Rev. Lett., vol. 74, pp 4043-4046, 1995
32. "Strong photoluminescence emission at room temperature of strained InGaAs quantum discs (200-300nm diameter) self-organized on GaAs (311) B substrate", R. Nötzel, J.

Temnyo, H. Kamada, T. Furuta, T. Tamamura, Appl. Phys. Lett., vol. 65, pp 457-459, 1994

33. "InGaAs-GaAs Quantum-dot lasers", D. Bimberg, N. Kristeadter, N.N. Ledentsov, Zh.I. Alferov, P.S. Kop'ev, V.M. Ustinov, IEEE. J.of Selected Topics in Quantum. Electron., vol. 3, pp 196-205, 1997
34. "Room temperature CW operation at the ground state of self-formed quantum dot lasers with multi-stacked dot layer", H. Shoji, Y. Nakata, K. Mukai, Y. Sugiyama, M. Sugawara, N. Yokoyama, H. Ishikawa, Electron. Lett, vol. 32, pp 2023-2024, 1996
35. "Low threshold large T_0 injection laser emission from (InGa)As quantum dots", N. Kristeadter, N.N. Ledentsov, M. Grundman, D. Bimberg, V.M. Ustinov, S.S. Ruvimov, M.V. Maximov, P.S. Kop'ev, Zh.I. Alferov, U. Richter, P. Werner, V. Goselev, J. Heydenreich, Electron.Lett., vol. 30, pp1416-1417, 1994
36. " Lasing at three dimensionally quantum confined sublevels of self organized $In_{0.5}Ga_{0.5}As$ quantum dots by current injection", H. Shoji, K. Mukai, N. Ohtsuka, M. Sugawara, T. Uchida, H. Ishikawa, IEEE Photon. Technol. Lett., vol. 12, pp 1385-1387, 1995
37. "Nanometer patterning of InP using aerosol and plasma etching techniques" A. Wiedensohler, Hans-Christen Hansson, I. Maximov, L.Samuelson, Appl. Phys. Lett., vol. 61, pp 837-839, 1992
38. "Selective growth of single InAs quantum dots using strain engineering", B.C. Lee, S.D. Lin, C.P. Lee, H.M. Lee, J.C. Wu, K.W. Sun, Appl. Phys. Lett. vol. 80, pp 326-328, 2002
39. "Observation of excited (bi-) exciton and multi-exciton features in locally homogeneous quantum dots", F.P.J. de Groote, T.W. Lippen, J.E.M. Haverkort, R. Nötzel, J.H. Wolter, Physica. E, vol. 17, pp 26-30, 2003
40. "Analysis of electric field effect in quantum box structure and its application to low- loss intersectional type optical switch", K.G. Ravikumar, T. Aizawa, K. Matsubara, M. Asada, Y. Suematsu, J. Lightwave. Tech., vol. 9, pp 1376-1385, 1991
41. "Observation of field induced refractive index variation in quantum box structure", T. Aizawa, K. Shimomura, S. Arai, Y. Suematsu, IEEE Photon. Technol. Lett., vol. 3, pp 907-909, 1991

42. “Novel hybrid optically bistable switch: The quantum well self-electro-optic effect device” D.A.B. Miller, D.S. Chemla, T.C. Damen, A.C. Gossard, W. Wiegmann, T.H. Wood, C.A. Burrus, Appl. Phys. Lett, vol. 45, pp 13-15, 1984
43. ”Biexcitons in semiconductor quantum dots”, Y.Z. Hu, S.W. Koch, M. Lindberg, N. Peyghambarian, R. Pollock, F.F. Abraham, Phys. Rev. Lett., vol. 64, pp 1805-1807, 1990
44. ”Theory of optically excited intrinsic semiconductor quantum dots” Y.Z. Hu, M. Lindberg, S.W. Koch, Phys. Rev. B, vol. 42, pp 1713-1723, 1990
45. “Intrinsic mechanism for the poor luminescence properties of quantum-box system”, H. Benisty, C.M. Sotomayor-Torres, C. Weisbuch, Phys. Rev. B, vol. 44, pp 10945-10948, 1991
46. “Photoluminescence of spherical quantum dots”, V.M. Fomin, V.N Gladilin, J.T. Devreese, E.P. Pokalitov, S.N. Balaban and S.N. Klimin, Phys.Rev.B 57, 2415, 1998
47. “Enhanced probalities of phonon assited optical transitions in semiconductor quantum dots”, J.T. Devreese, V.M. Fomin, V.N Gladilin, E.P. Pokalitov and S.N. Klimin, Nanotechnology 13, 163-168, 2002
48. “Froehlich interaction in InAs/GaAs self assembled quantum dots”, A.W.E. Minnaert, A.Yu. Silov, W.van der Vleuten, J.E.M. Haverkort and J.H. Wolter, Phys.Rev. B, vol 63, pp 075303
49. “Theory of the linear and nonlinear optical properties of semiconductor microcrystallites”, S. Schmitt-Rink, D.A.B. Miller, D.S. Chemla, Phys. Rev. B, vol. 35, pp 8113-8125, 1987
50. E.I. Rashba and G.E. Gurgenishvili, Fiz. Tverd. Tela (Leningrad) 4, 1-29 (1962); Sov.Phys.Solid.State. 4, 759 (1962)
51. “Third-order optical nonlinearities in semiconductor microstructures”, L. Banyai, Y.Z. Hu, M. Lindberg, S.W. Koch, Phys. Rev. B, vol. 38, pp 81428153, 1988
52. “Strong coupling regime for quantum boxes in pillar microcavities: Theory”, L.C. Andreani and G.Panzarini, Phys.Rev.B 60, 13276-13279, 1999
53. “Excitonic quantum confined effects and exciton electroabsorption in semiconductor thin quantum boxes”, H. Gotoh, H. Ando, J. Appl. Phys., vol. 82, pp 1667-1677, 1997
54. “Time-resolved optical characterization of InGaAs/GaAs quantum dots”, G. Wang, S. Fafard, D. Leonard, J.E. Bowers, J.L. Merz, P.M. Petroff, Appl. Phys. Lett., pp 2815-2817, 1994

55. "Nonlinear Nano-Optics: Probing one exciton at a time", N.H. Bonadeo, G. Chen, D. Gammon, D.S. Katzer, D. Park, D.G. Steel, Phys. Rev. Lett., vol. 81, pp 2759-2762, 1998
56. "Theory of spontaneous-emission lifetime of Wannier excitons in mesoscopic semiconductor quantum disks", M. Sugawara, Phys. Rev. B, vol. 51, pp 10743-10754, 1995
57. "Femtosecond dynamics and absorbance of self-organized InAs quantum dots emitting near 1.3 µm at room temperature", D. Birkedal, J. Bloch, J. Shah, L.N. Pfeiffer, K. West, Appl. Phys. Lett., vol. 77, pp 2201-2203
58. "Optical nonlinear properties of InAs quantum dots by means of transient absorption measurements", H. Nakamura, S. Nishikawa, S. Kohmoto, K. Kanamoto, K. Asakawa, J. Appl. Phys., vol. 94, pp 1184-1189, 2003
59. "Picosecond time-resolved bleaching dynamics of self-assembled quantum dots", E.W. Bogaart, J.E.M. Haverkort, T. Mano, R. Nötzel, J.H. Wolter, P.Lever, H.H. Tan, C. Jagadish, Proc. IEEE Nano-2003 conference, San Fransisco, USA, pp 663-667, 2003
60. "Dephasing in InAs/GaAs quantum dots", P.Borri, W.Langbein, J.Mork, J.M. Hvam, F.Heinrichsdorff, M.-H. Mao and D. Bimberg, Phys.Rev.B, vol. 60, pp. 7784-7787, 1999

Chapter 2

Theory of electro-refraction in nanostructures

"In Nature's infinite book of secrecy
A little I can read"

William Shakespeare

2.1 Introduction

The electronic and optical properties of low-dimensional semiconductor structures and semiconductor nanostructures are completely determined by size quantization and confinement effects. Physical properties like, for example, the electro-absorption and electro-refraction are thus strongly influenced by the design of the semiconductor nanostructure in all three dimensions. After the pioneering work of Esaki and Tsu [1], the idea of artificially designed semiconductor structures gained momentum. In particular, the progress in epitaxial growth techniques such as chemical beam epitaxy (CBE), molecular beam epitaxy (MBE), metal-organic chemical vapor deposition (MOCVD) or metal organic vapor phase epitaxy (MOVPE) have generated a tremendous development in the semiconductor physics and device technology based on these artificially designed semiconductor nanostructures.

The III-V semiconductor materials are potential candidates for opto-electronic devices, because of their direct bandgap structure. Moreover, semiconductor heterostructures, including quantum wells, super-lattices and modulation-doped heterostructures could easily be exploited in the GaAs/AlGaAs material system due to their negligible lattice mismatch. The high carrier mobility of GaAs based materials makes it attractive for high-speed electronic devices. By exploiting the self-assembled Stranski-Krastanov growth, InAs/GaAs quantum dots could also be realized in these III-V semiconductors, allowing increasing the effective confinement potential towards three dimensions, resulting in completely discrete energy levels. The resulting atomic-like spectra and the zero-dimensional density of states in these quantum dots provide a new opportunity to further tailor the optical properties towards the needs of a specific application.

The material properties of the low-dimensional III/V semiconductors have resulted in a wide range of electronic, opto-electronic and optical devices, including semiconductor lasers, semiconductor optical amplifiers, optical waveguides, electro-optic modulators and photodetectors. In this thesis, we will investigate the electro-refraction and the refractive index nonlinearities in semiconductor quantum wells and quantum dots, which are relevant for photonic switching applications. The III/V material system allows an optimization of these physical properties with respect to various structure parameters such as the quantum well design, the layer composition, the lattice strain and the thickness, as well as the shape, the size and the composition of the quantum dots. A clever manipulation of the strain due to lattice mismatch between the substrate and the epitaxial layers gives the possibility to modify the polarization properties, allowing to design polarization independent devices, which are essential for optical communication systems. As a starting point for these bandgap engineering efforts, a thorough understanding of the band structure is required to make fully use of all relevant material properties for device design.

The present chapter discusses the electro-refraction in III-V semiconductor nanostructures based upon band structure calculations using the 4x4 Luttinger-Kohn Hamiltonian [2]. We will focus on the theory of quantum dots since quantum dots are considered to be the most promising materials for switching applications.

2.2 III-V Semiconductors

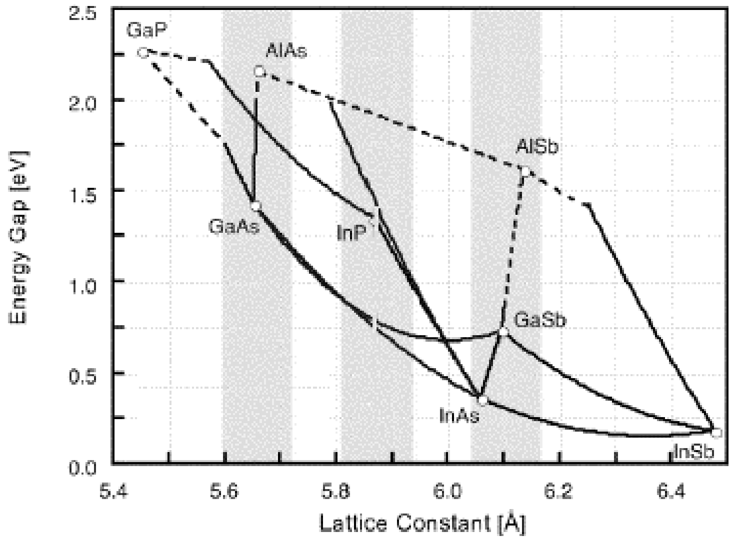

Figure 2.1: The bandgap energy as a function of the lattice constant in III-V semiconductor material at 4K. (Jasprit Singh.)

III-V compound semiconductor materials generally have a zinc blend structure, which is made up out of two face centered cubic units cells, displaced over a quarter diagonal. Many of these compounds have direct band gap and hence a non-phonon assisted optical transition is possible. The resulting high optical transition probability is of utmost importance for device applications in optical communications. The thermodynamic stability of most ternary and quaternary alloys provides a wide opportunity for bandgap tuning towards the optical communication wavelength window. The variation of bandgap with respect to the lattice constant for different alloy composition can be read from figure 2.1.

The lattice constants and the bandgap energy of the ternary compounds can be obtained from the binary constituents by Vegard's law [3]. For $Ga_xIn_{1-x}As$, the lattice constant a(x) can be expressed as

$$a(x)=x.a^{GaAs}+(1-x).a^{InAs} \tag{2.1}$$

where a^{GaAs}, a^{InAs} are the lattice constants of the binary GaAs and InAs compounds, respectively. If the energy gaps of GaAs and InAs are denoted as E_g^{GaAs}, E_g^{InAs}, than the bandgap of the ternary GaInAs compound is

$$E_g(x)=x.E_g^{GaAs}+(1-x)\,E_g^{InAs}-C.x.(1-x) \tag{2.2}$$

where C is the bowing parameter. The lattice constants and the bandgaps of the other compounds follow from the similar relations.

2.3 Strain effects in quantum wells and quantum dots

A lattice mismatch between the epitaxial layer and the substrate leads to a tetragonal distortion of the primitive cell in the growth direction. As long as the lattice mismatch is smaller than a few percent, the lattice constant of the epitaxial layer parallel to the growth interface adjusts itself to the lattice constant of the substrate, as schematically depicted in figure 2.2. If the bulk lattice constant of the epitaxial layer is smaller than that of substrate, the layer becomes tensile strained and if the lattice constant of the epitaxial layer is larger than that of substrate, the layer becomes compressively strained. The strain depends on the orientation of the substrate during the growth. In our calculations, we consider epitaxial layers grown on a (100) substrate. In this case, the strain tensor is diagonal. Hence from elasticity theory, the strain components parallel and perpendicular to the growth interface, can be written as

$$\begin{aligned} \varepsilon_{\parallel} &= \varepsilon_{xx} = \varepsilon_{yy} = \frac{a_s - a_L}{a_L} \\ \varepsilon_{\perp} &= \varepsilon_{zz} = -2\frac{c_{12}}{c_{11}}\varepsilon_{\parallel} \end{aligned} \tag{2.3}$$

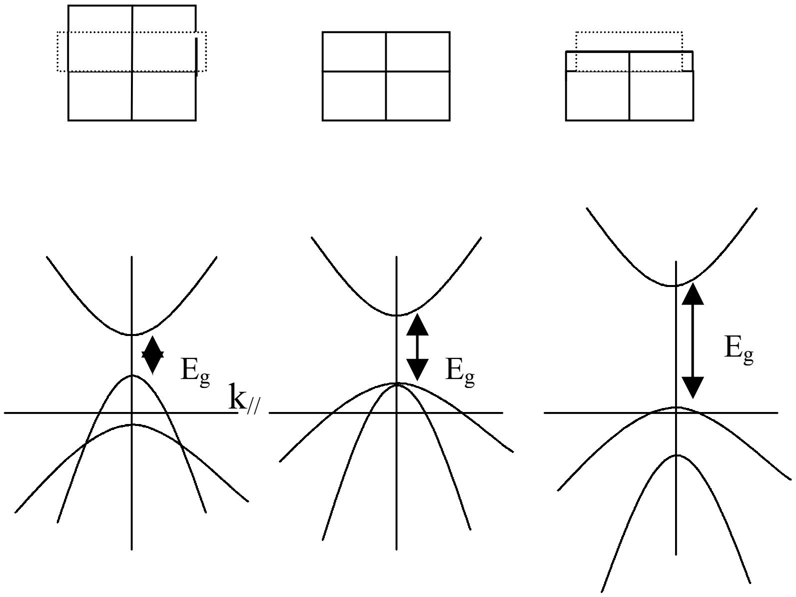

Figure 2.2: The effect of strain on the band structure of a direct bandgap semiconductor. In compression (left), the epitaxial layer is compressed parallel to the growth interface, while it becomes elongated in the growth direction. Due to the hydrostatic stain component, the bandgap is reduced. The shear strain component lifts the lh-subband above the hh-subband. The middle panel shows the unstrained situation and the right panel shows a tensile strained epitaxial layer, which is elongated parallel to the growth interface and compressed in the growth direction.

where a_L is the lattice constant of the epitaxial layer, a_s is the lattice constant of the substrate and c_{ij} are the elastic stiffness constants of the epitaxial layer.

For our band structure calculations, it is useful to decompose the total biaxial strain tensor into a pure hydrostatic component and pure shear strain component, which are given by

$$\varepsilon_{hy} = 2\varepsilon_{\parallel} + \varepsilon_{\perp} \tag{2.4}$$

$$\varepsilon_{sh} = \varepsilon_{\perp} - \varepsilon_{\parallel} \tag{2.5}$$

The hydrostatic strain shifts the hole and electron levels further apart and the shear strain shifts the heavy hole and light holes in the opposite directions, as schematically indicated in figure 2.3.

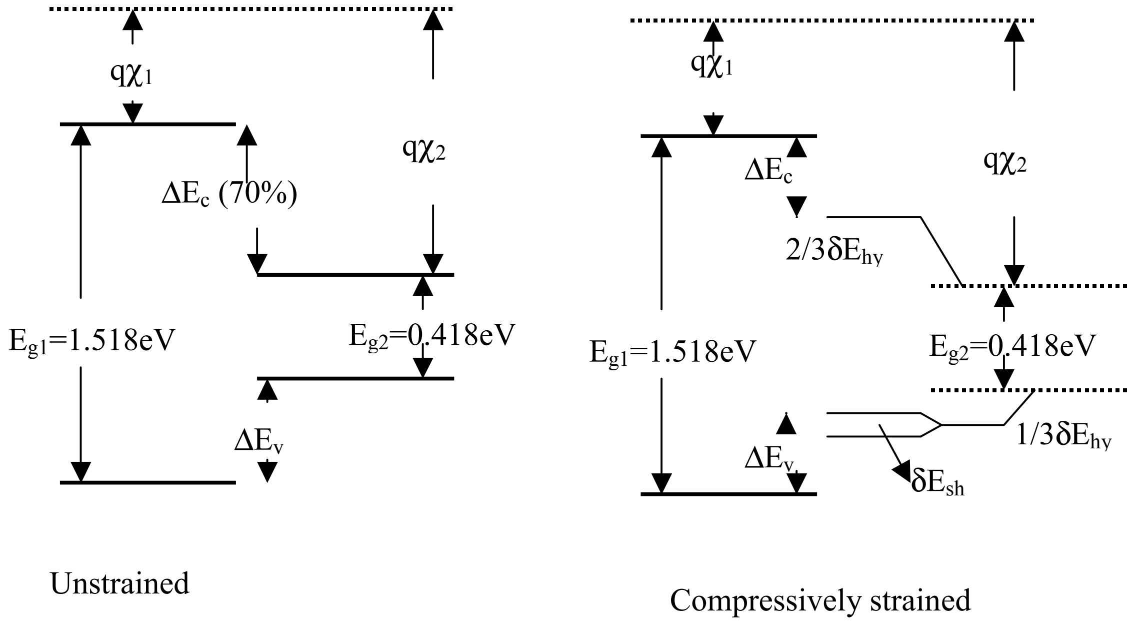

Figure 2.3: Electronic structure of the InAs/GaAs material system

With increasing layer thickness, the strain also increases. Above a critical layer thickness, relaxation of the epitaxial layer to the strain-free lattice constant starts by the formation of misfit dislocations. The critical layer thickness, up to which the growth remains pseudomorphic, is given by

$$L_c = \frac{a_L}{\sqrt{2\pi\left|\varepsilon_{||}\right|}}\left(\frac{1-\frac{1}{4}\nu}{1+\nu}\right)\left[\ln\left(\frac{\sqrt{2}L_c}{a_L}\right)+1\right] \tag{2.6}$$

where ν is the Poisson ratio which is equal to $c_{11}/(c_{11}+c_{12})$.

2.4 Electron and hole confinement levels in semiconductor nanostructures

For InGaAs/InP and InAsP/InP quantum well materials, the conduction band states are well separated from the valence band state and therefore we treat the conduction band in the effective mass approximation as parabolic. In the valence band, the split-off (SO) states are well separated from the other four angular momentum states and hence we also neglect the SO-states in our **k.p** calculation [4]. Due to the near degeneracy of the hole bands, their mutual interaction is large. More importantly, the interaction between the light- and heavy-hole bands determines the polarization dependence. We therefore perform the band structure calculation within the framework of the 4x4 Luttinger-Kohn Hamiltonian. For InAs/GaAs self-assembled quantum dots, it is well known [5] that one, in principle, has to use a 8x8 **k.p** description [6] due to the small (0.4 eV) unstrained InAs bandgap and the large strain-induced corrections, which are of similar magnitude as the unstrained InAs bandgap. Since we are interested in the electro-refraction in quantum dots and not in a precise comparison between theory and spectral position of single dot PL transitions, we decided to use the 4x4 Luttinger-Kohn model, also for the quantum dot case.

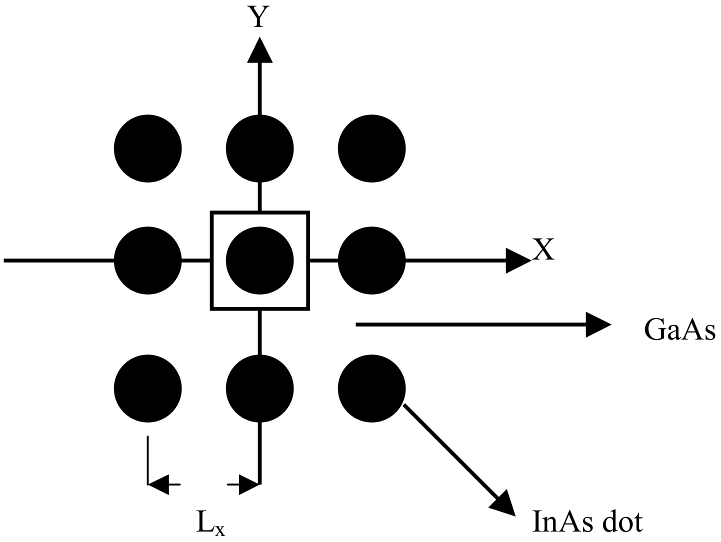

Figure 2.4: Schematic diagram of the quantum dot, including the periodic boundary conditions

This section discusses the band structure calculation for quantum dots in the presence of an applied electric field. A simple transition of operators will also provide the possibility to calculate the quantum well and quantum wire confinement levels (the envelope functions should also change dimensionality). We follow the approach of Su-Shen Li in which a quantum dot is embedded inside a surrounding barrier matrix and we apply periodic boundary conditions, as shown in figure 2.4. The effect of the periodic boundary conditions is that we effectively study an array of isolated quantum dots with a density governed by the dimensions of the box, which is indicated in the Fig. 2.4. In the calculation, we take a box with a length of L_x, L_y, L_z in the x, y, z directions respectively. The model allows dots of different shapes and includes the coupling between the heavy-hole and light-hole valence bands, which is important for calculating the correct polarization dependence.

In the effective mass envelope function approximation [7,8] the electron state in the conduction band is represented by a simple Schrödinger equation

$$H_e = \hbar^2 \nabla \left(\frac{1}{2m^*(x,y,z)}\right) \nabla + V_e(x,y,z) + a_c \Delta E_{hy}(x,y,z) - eFz \tag{2.7}$$

where m^* represents the effective electron mass, which we allow to be position dependent. In the case of an InAs quantum dot within a GaAs or InP matrix, the effective electron mass reads

$$m^*(x,y,z) = \begin{cases} m_1^* & inside\ the\ QD\ (effective\ \ mass\ of\ \ InAs) \\ m_2^* & elsewhere\ \ (effective\ \ mass\ of\ \ GaAs\ or\ \ InP) \end{cases} \tag{2.8}$$

The confinement potential is expressed as

$$V_e(x,y,z) = \begin{cases} 0 & inside\ the\ QD \\ V_{e0} & elsewhere \end{cases} \tag{2.9}$$

where V_{e0} is the conduction band offset. The third term in the Hamiltonian represents the component of the hydrostatic strain [9] acting on the conduction band, as explained in Sec. 2.3. In our calculation, we assign two third of the total hydrostatic strain correction ΔE_{hy} to the conduction band, implying a_c =2/3. The last term in the Hamiltonian represents the Stark shift due to the externally applied electric field of strength F. To solve the envelope function equation we used the numerical matrix-diagonalization [10] scheme by using plane-waves as the expansion basis for the wave function of the confined state. So the electron wave function takes the following form [11].

$$\psi_e(x,y,z) = \frac{1}{\sqrt{L_x L_y L_z}} \sum_{n,m,l} C_{nml} e^{i[(k_x+nK_x)x+(k_y+mK_y)y+(k_z+lK_z)z]} \tag{2.10}$$

where $K_x=2\pi/L_x$, $K_y=2\pi/L_y$, $K_z=2\pi/L_z$ and n, m, l=0,±1, ±2, ±3,…..

In the valence band, the 4x4 Luttinger-Kohn Hamiltonian accounts for the coupling between the light holes (LHs) and the heavy holes (HHs), but neglects the split-off band. With respect to the HH and LH spin up $(\uparrow)$ and spin down $(\downarrow)$ basis vectors $\left|HH\uparrow\right\rangle = \left|3/2, 3/2\right\rangle$,

$\left|LH\uparrow\right\rangle = \left|3/2, 1/2\right\rangle$, $\left|LH\downarrow\right\rangle = \left|3/2, -1/2\right\rangle$ and $\left|HH\downarrow\right\rangle = \left|3/2, -3/2\right\rangle$, the valence band Hamiltonian can be written as

$$H_{hole} = \frac{\hbar^2}{2m_0}\begin{bmatrix} P_+ - \Delta E_{sh} & R & -Q_- & 0 \\ R^+ & P_- + \Delta E_{sh} & C^+ & -Q_+^+ \\ -Q_-^+ & C & P_- + \Delta E_{sh} & -R \\ 0 & -Q_+ & -R^+ & P_+ - \Delta E_{sh} \end{bmatrix} + a_v \Delta E_{hy} + V_h - eFz \quad (2.11)$$

The strain tensor again depends on the crystal symmetry and the substrate orientation. In the [100] direction, the strain tensor is diagonal and we assume that the strain is completely in the dot region. Hence, from the strain effect explained in section 2.3, the strain components can be written as

$$\Delta E_{sh} = \begin{cases} \Delta E_{sh0} & \text{inside the QD} \\ 0 & \text{elsewhere} \end{cases} \quad (2.12)$$

$$\Delta E_{sh0} = -\frac{2}{3} D_u \left(1 + \frac{2c_{12}}{c_{11}}\right)\frac{a_0 - a}{a} \quad \text{shear strain component} \quad (2.13)$$

$$\Delta E_{hy} = -2D_d \left(1 - \frac{c_{12}}{c_{11}}\right)\frac{a_0 - a}{a} \quad \text{hydrostatic strain component} \quad (2.14)$$

a and a_0 are the lattice parameters of bulk dot and barrier material respectively, c_{11} and c_{12} are the elastic moduli of the dot material, while D_d and D_u are the deformation potentials.

$$V_h(x, y, z) = \begin{cases} 0 & \text{inside the QD} \\ V_{h0} & \text{elsewhere} \end{cases} \quad (2.15)$$

where V_{h0} is the valence band offset.

The kinetic energy operator, in which m_0 is the free electron mass, can be written in terms of Luttinger effective mass parameters as

$$P_\pm = p_x(\gamma_1 \pm \gamma_2)p_x + p_y(\gamma_1 \pm \gamma_2)p_y + p_z(\gamma_1 \mp 2\gamma_2)p_z \quad (2.16)$$

The coupling between the subbands is given by the off-diagonal elements in the hole Hamiltonian. From reference [12] the operators in the Hamiltonian are written as

$$Q_{\pm} = 2\sqrt{3}\left[(p_x \pm ip_y)(\sigma-\delta)p_z + p_z\pi(p_z\pi(p_x \pm ip_y)\right] \tag{2.17}$$

$$R = \sqrt{3}\left[(p_x + ip_y)\mu(p_x + ip_y) - (p_x - ip_y)\gamma(p_x \pm ip_y)\right] \tag{2.18}$$

$$C = 2p_z(\sigma-\delta-\pi)(p_x - ip_y) - 2(p_x - ip_y)(\sigma-\delta-\pi)p_z \tag{2.19}$$

and

$$\sigma - \delta = (-1-\gamma_1 + 2\gamma_2 + 6\gamma_3)/6 \tag{2.20}$$

$$\pi = (1+\gamma_1 - 2\gamma_2)/6 \tag{2.21}$$

$$\gamma = (\gamma_2 + \gamma_3)/2 \tag{2.22}$$

$$\mu = -(\gamma_2 - \gamma_3)/2 \tag{2.23}$$

where γ_1, γ_2 and γ_3 are the functions of the spatial position x, y, z. In order to avoid the complications due to the spatial dependence of the effective mass, we calculated the matrix elements of barrier region and well region separately [13]. Hence

$$\gamma_1 \quad \gamma_2 \quad \gamma_3 = \begin{cases} \gamma_{11} \quad \gamma_{12} \quad \gamma_{13} & \textit{inside the} \quad QD \\ \gamma_{21} \quad \gamma_{22} \quad \gamma_{23} & \textit{elsewhere} \end{cases} \tag{2.24}$$

where γ_{11}, γ_{12}, γ_{13} and γ_{21}, γ_{22}, γ_{23} are the Luttinger effective mass parameters of the dot and barrier materials, respectively. The heavy hole- light hole mixing is determined by R^+, C^+ and Q^+ and R, C and Q, which are each other's complex conjugates. If there is no mixing the Hamiltonian becomes diagonal. The mixing exists even when k=0 (at the Γ point) in coupled quantum dots. In the envelope formulism it is usually assumed that the interface potential does not mix the various band edges, but only shifts them [14]. So the electrostatic potential term is added to the diagonal of the Hamiltonian.

Within the matrix diagonalization framework, we also use a plane-wave expansion for the hole envelope wave functions, which reads

$$\Psi_h(x_h, y_h, z_h) = \frac{1}{\sqrt{L_x L_y L_z}} \sum_{n,m,l} \begin{bmatrix} a_{nml} \\ b_{nml} \\ c_{nml} \\ d_{nml} \end{bmatrix} e^{i[(k_x+nK_x)x_h+(k_y+mK_y)y+(k_l+lK_l)z]} \tag{2.25}$$

Further details of this calculation are provided in the Appendix given at the end of the chapter. The quantum dot size dependence of the transition energy for a cylindrical quantum dot is shown in fig. 2.5 and fig. 2.6 as a function of the QD-height and QD-radius. An externally applied electric field will modify the confinement potential, which decreases the effective confinement energies within the quantum dot, and thus yield a red shift of the effective bandgap (fig.2.7). In addition, the applied electric field pulls the electron and the hole envelope wave functions to opposite sides

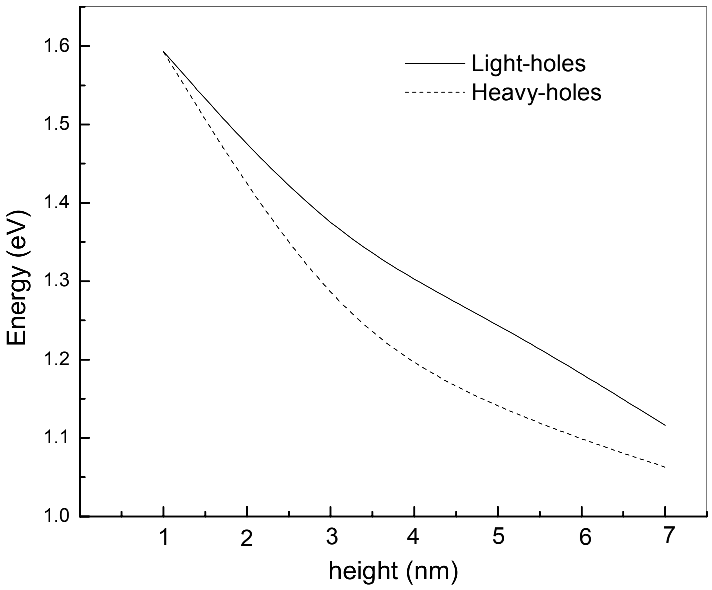

Figure 2.5: The transition energies at 4K as a function of dot height in an InAs/GaAs cylindrical quantum dot with a radius of 5 nm.

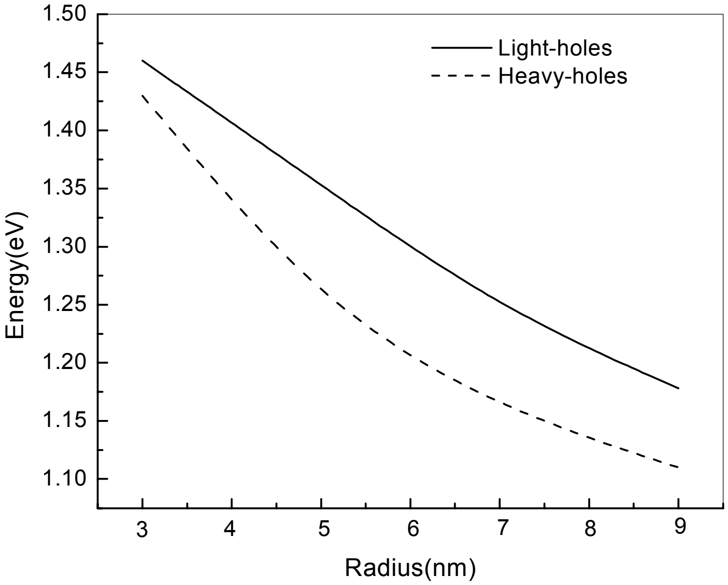

Figure 2.6: Transition energy at 4K, as a function of the dot radius in InAs/GaAs cylindrical quantum dot with a height of 3 nm.

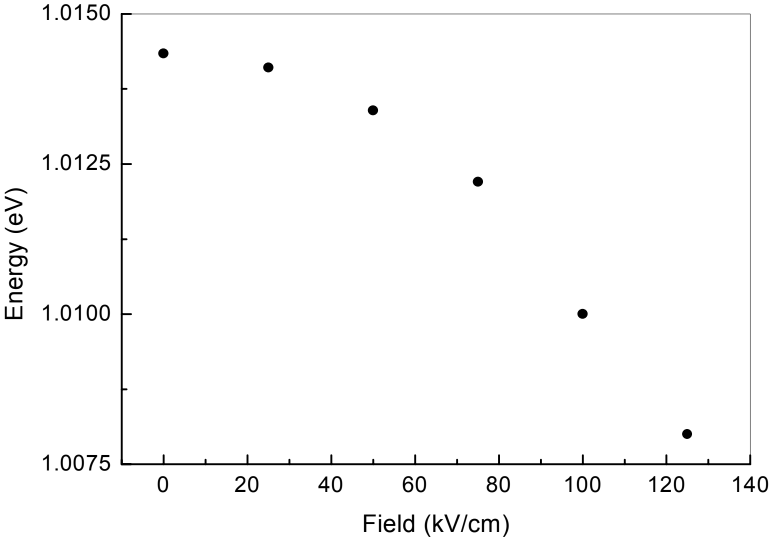

Figure 2.7: Heavy hole transition energy as a function of applied field in an InAs/GaAs quantum dot with a height of 6nm and a radius of 5 nm at 4K

of the potential well, resulting in a decreasing overlap and thus a decreasing absorption strength. As a result, the exciton binding energy also decreases due to the decreased overlap between the hole and the electron wavefunction. This effect is the Quantum Confinement Stark Effect (QCSE) [15]. Forbidden transitions in the absence of field might also become observable in the presence of an electric field.

In highly strained quantum dots, the light hole states will also interact with the split-off states. This interaction is not properly accounted for in our model and needs at least the 6x6 Luttinger-Kohn formalism. In our calculation, we accept this as an error in the light hole transition energy.

2.5 Excitons

A Coulombic bound state of a conduction band electron and a valence band hole is called an exciton [16,17]. In semiconductors, the exciton Bohr-radius amounts to 300 Å, which is much larger than the lattice constant, i.e. the excitons are shallow and called Wannier excitons [17]. The formation of excitons will produce a red shift in the absorption spectrum with respect to the interband transition. Within a quantum dot, the electron and holes are already bound together by the confinement potential of the quantum dot. It is thus impossible to distinguish between an exciton and a bound electron-hole pair. In the remainder of this Thesis, we will refer to the Coulombic and confinement bound electron-hole pair as an exciton. The exciton binding energy in a quantum dot is strongly dependent on the size and shape of the dot. The Hamiltonian describing the exciton states will be expressed as

$$H = -\frac{\hbar^2}{2m_h}\left(\frac{\partial^2}{\partial x_h^2}+\frac{\partial^2}{\partial y_h^2}+\frac{\partial^2}{\partial z_h^2}\right)+V_h(x_h,y_h,z_h)-\frac{\hbar^2}{2m_e}\left(\frac{\partial^2}{\partial x_e^2}+\frac{\partial^2}{\partial y_e^2}+\frac{\partial^2}{\partial z_e^2}\right)+V_e(x,y,z)$$
$$-\frac{e^2}{4\pi\varepsilon_0\varepsilon\sqrt{(x_e-x_h)^2+(y_e-y_h)^2+(z_e-z_h)^2}}+eFz \tag{2.26}$$

The first term and third term are the kinetic energy terms of the valence band and the conduction band states, respectively. The second and fourth terms represent the individual confinement potentials of the hole state and electron state respectively. All these operators are dependent on their respective single particle co-ordinate systems and hence already diagonalized with respect to the basis set of individual single particle wave functions. The Coulombic term depends on the electron-hole distance and thus cannot be diagonalized with respect to the basis of the single particle wave functions. Hence we must form an orthogonal basis set of product wave functions. $|\Psi_e\rangle|\Psi_h\rangle$, where $|\Psi_e\rangle$ and $|\Psi_h\rangle$ are the individual electron and hole wavefunctions used to diagonalize 2.7 and 2.11.

The linear and nonlinear optical properties of quantum wells and quantum dots are strongly affected by the excitonic effect in the spectral region close to the fundamental energy gap. Hydrogen like discrete energy lines can be observed [18] in the photoluminescence spectrum of quantum dots at low temperature, revealing the Coulombic interaction between the electron and the hole state. The spectral weight of the QD lines is inversely proportional to the volume of the dot [19], whereas the oscillator strength of the exciton transition is proportional to the ratio of the exciton volume and the QD volume. The confinement energy varies like L^{-2} and the Coulomb energy scales like L^{-1}.

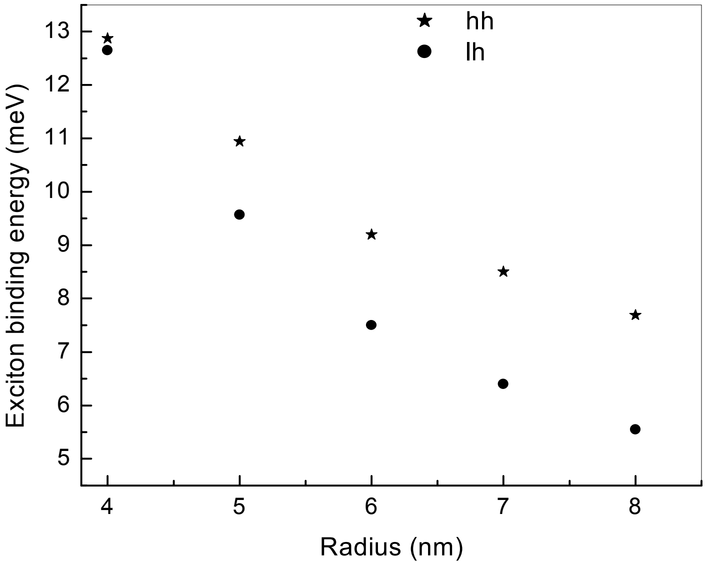

Figure 2.8: Exciton binding energy as a function of the QD-radius for an InAs/InP quantum dot with a height of 6 nm

The inclusion of the Coulomb interaction leads to a small renormalization of the oscillator strength and a red shift of the transition energies The oscillator strength per unit cell of the 1s quasi 2D free exciton has been calculated within the effective-mass approximation.

2.6 Hilbert space

Theoretically the Hilbert space is spanned up by a complete set of basis functions. For numerical computation we have to incorporate as much plane wave states as possible to get a good convergence of the eigenvectors and eigenvalues. This, however, leads to computational difficulties and takes a too long computation time. In our calculations we consider 353 plane waves for the calculation of the electron envelope function. We adopt a numerical matrix diagonalization technique to calculate the energy values and Fourier expansion coefficients of the confined states. When we are considering all the transitions between the conduction and valence band states, the total integrated overlap is given by

$$\sum_{n,m,l} \left| \left\langle \Psi_e^{nml} \middle| \Psi_h^{n'm'l'} \right\rangle \right|^2 = 1 \qquad (2.27)$$

where Ψ_e^{nml} and $\Psi_h^{n'm'l'}$ are the electron and hole envelope functions respectively. This implies that the sum of the optical transition matrix elements for transitions from one electron level to all the light hole or heavy hole levels is a constant, which is known as a sum rule [5]. We primarily employ this sum rule for checking the accuracy of our calculation. For an improved conservation of the sum rule, we need to incorporate more plane-wave states. In small quantum dots with only one or two confined electronic states, convergence is relatively easy, but for a larger quantum dot, many more plane wave states are needed for a proper convergence of the eigenstates. Finally, we want to remark that the plane wave states are not a very good basis sets for an arbitrary quantum dot geometry but it will span up a complete set for square, cylindrical and cone-shaped pyramidal quantum dots.

2.7 The bandfilling effect in quantum wells and quantum dots

In the case of n-type or p-type doping, the bottom of the conduction band or the top of the valence band becomes occupied with carriers. Optical pumping will fill both the valence and conduction bands with an equal amount of carriers. This bandfilling will create a blue shift of the absorption spectrum. Bandfilling through doping might also lead to band bending, which requires a self-consistent bandstructure calculation. We will however assume that charge neutrality is maintained everywhere inside the structure, which can be achieved by, for example doping inside the quantum well. In addition to the bandfilling effect, the Coulombic interaction between the carriers will lead to a band gap renormalization. In addition, the free carrier intra band absorption or plasma effect will also produce a refractive index variation. The bandgap renormalization is incorporated into our model by using the results from Ahn et.al [20]. Since we are interested only in very low carrier concentrations, to avoid an excessive free carrier absorption loss, the refractive index contribution from the plasma effect is taken as more than two orders of magnitude smaller than the bandfilling contribution.

We calculated the bandfilling effect by writing the total absorption probability as [16]

$$P(\omega)=\frac{2\pi}{\hbar}\frac{e^2F^2}{4m_0^2\omega^2}\hbar\omega\sum_{c,v}\delta\left(\varepsilon_c-\varepsilon_v-\hbar\omega\right)\left|\left\langle\Psi_c\left|\hat{\varepsilon}.\vec{p}\right|\Psi_v\right\rangle\right|^2\left[f(\varepsilon_v)-f(\varepsilon_c)\right] \qquad (2.28)$$

in which $f(\varepsilon_j)$ is the Fermi-Dirac distribution, which is written as

$$f(\varepsilon_j)=\frac{1}{1+e^{(\varepsilon_j-\mu)/k_BT}} \qquad (2.29\ )$$

in which T is the temperature and μ the chemical potential.

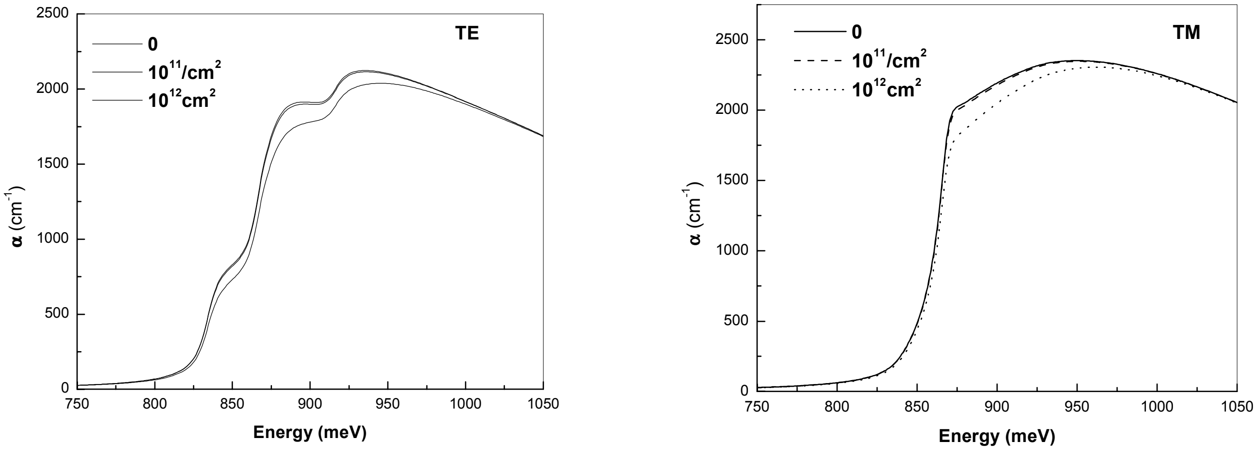

Figure 2.9: Calculated carrier induced changes of the TE and TM absorption spectra in a 110Å InGaAs/InP quantum well at room temperature

The band gap renormalization due to many body effects has been the subject of many theoretical [20] and experimental papers [21]. Since the bandgap shrinkage is basically a minor correction to the electro-refraction compared to the bandfilling effect, we basically followed the theoretical results of Ahn et.al [20] and the experimental data of Park et.al. [21], who reported a bandgap shrinkage proportional to $(n_{2D})^{1/3}$ at high (> 10^{12}/cm^2) carrier density and a bandgap shrinkage proportional to $(n_{2D})^{1/2}$ at low carrier density. With this model, we calculated the quantum well TE and TM absorption spectra, which are shown in figure 2.9. As can be seen from the figures, the bandfilling contribution is dominant, while the bandgap shrinkage is hardly observable.

2.8 Electro-absorption and electro-refraction

The optical absorption in a single inter-band transition can be written as [22,23]

$$\alpha(\hbar\omega) = \frac{4\pi^2 e^2 \hbar}{\varepsilon_0 c n m_0^2 \hbar\omega} \sum_{k_{\backslash\backslash}} \sum_{n,m} F_s \left|\hat{\varepsilon}.p_{nm}(k_{\|})\right|^2 J_{c_n v_m}(k_{\|},\, \hbar\omega) \tag{2.30}$$

where F_s is the Sommerfeld factor, ε is the polarization vector and J_{cv} is the joint density of states (JDOS). The strength of the optical transition is proportional to the square of the inter-band dipole matrix element, which is in turn proportional to the electron-hole envelope function overlap integral, and to the joint density of states. The joint density of states is defined as [23]

$$J_{cv}(\hbar\omega) = \int_{V_{bz}} \frac{2dk}{2\pi^3} \delta\left[E_c(k) - E_v(k) - \hbar\omega\right] \tag{2.31}$$

where $E_c(k)$ and $E_v(k)$ are the dispersion relations for electrons and holes respectively and V_{bz} is the volume of the first Brillouin zone.

In quantum dots, the selection rules [24] will keep the JDOS as a set of Kronecker delta-like functions, because there is no wavevector dependence on the transition energy [25]. In quasi two-dimensional systems, like a quantum well, the JDOS can locally change shape by applying strain or an electric field. In this case the whole dispersion relations in the first Brillouin zone are required for calculating the JDOS. The anticrossings in the dispersion relations of strained quantum well will easily generate numerical instabilities. To reduce computational difficulties in quantum wells, we neglect the in-plane anisotropy in the JDOS. The joint density of states then reads

$$J_{cv}(k_x,\hbar\omega) = \frac{k_x}{2m\dfrac{d}{dk_x}\left(E_c(k_x) - E_v(k_x)\right)} \delta\left[E_c(k_x) - E_v(k_x) - \hbar\omega\right] \tag{2.32}$$

Both 2D and 0D systems, show broadened absorption spectra, due to carrier dephasing, phonon scattering induced broadening and inhomogeneities. Hence in any real absorption spectrum the δ function in Eq. (2.32) must be replaced by a proper broadening function. A number of line-shape functions have been used for broadening the absorption spectra [26-28,22]. We used a Gaussian line shape function with a Lorentian tail. The FWHM of the line-shape function is obtained from the PL spectra. For theoretical calculations we used the experimentally obtained literature values for the dephasing time at room temperature [29]. For a single quantum dot, the homogeneous line width, as determined by the dephasing time, is quite narrow (FWHM< 5meV), even at room temperature. In a quantum dot ensemble, each individual dot has slightly different properties induced by variations in size, shape, strain etc, leading to an inhomogeneous broadening of the absorption spectrum of the ensemble of quantum dots. This inhomogeneous broadening can be described with a Gaussian size distribution, which includes a distribution of both the dot heights and the lateral dimensions (radius) around an average height h_0 and an average radius r_0 with standard deviation σ. Both the average size and the standard deviation in this size can be obtained from the photoluminescence spectrum.

2.8.1 The Urbach tail

In optical modulators and switches which employ semiconductor based waveguides, the residual absorption loss is determined by the Urbach tail. The Urbach tail can be expressed as

$$\alpha(E) = \alpha_0 e^{(h\upsilon - E_g)/E_0(T)} \tag{2.33}$$

in which E_0 (T) is the Urbach parameter. The origin of the Urbach tail has been much debated in literature, but is generally believed to be due to microfields of static origin. These microfields due to doping atoms, imperfections, etc, result in broadening of the absorption edge through the Franz-Keldysh effect. Another mechanism for the Urbach tail in undoped materials is the quasi-static potential variation due to phonons. In our calculations, we broadened the absorption spectrum with an Urbach tail to correctly calculate the waveguide absorption loss far away from the optical transition.

2.9 Polarization dependence

The polarization dependence of optical transition in quantum dots grown on a (001) substrate depends on the Bloch part of the matrix elements.

Within the dipole approximation, the transition matrix elements for the TE-waveguide mode are given by [30]

heavy hole to conduction band $$\left|\langle U_e | \hat{\varepsilon}.\vec{p} | U_{hh} \rangle\right|^2 = \left(\frac{\Pi}{\sqrt{2}}\right)^2 \tag{2.34}$$

light hole to conduction band $$\left|\langle U_e|\hat{\varepsilon}.\vec{p}|U_{lh}\rangle\right|^2 = \left(\frac{\Pi}{\sqrt{6}}\right)^2 \tag{2.35}$$

For the TM-waveguide mode, the matrix elements are

heavy hole to conduction band $$\left|\langle U_e|\hat{\varepsilon}.\vec{p}|U_{hh}\rangle\right|^2 = 0 \tag{2.36}$$

Light hole to conduction band $$\left|\langle U_e|\hat{\varepsilon}.\vec{p}|U_{lh}\rangle\right|^2 = \left(\frac{2\Pi}{\sqrt{6}}\right)^2 \tag{2.37}$$

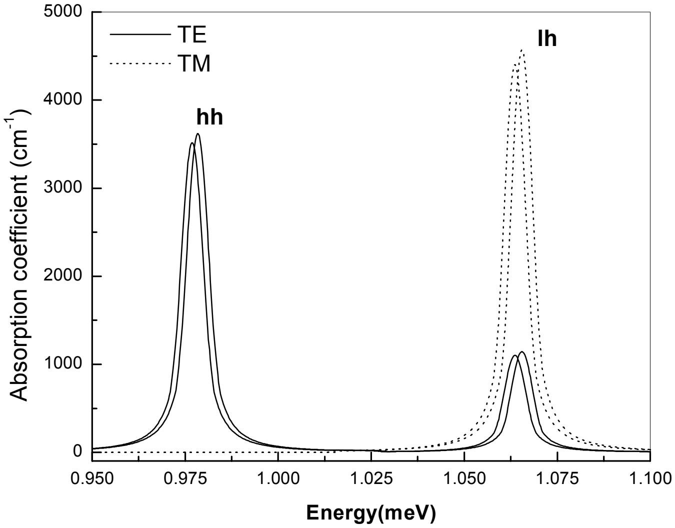

Figure 2.10: Calculated absorption spectra for TE and TM polarization for cylindrical InAs/GaAs quantum dot with a radius of 5nm and a height of 6nm at an electric field 0 and 100kV/cm (red shifted).

Polarization independent behavior can be realized by applying tensile strain, which lifts up the light-hole band above the heavy-hole band. Since the heavy-hole transition shows a TE-polarization and the light-hole transition is mainly TM-polarized, one can find a particular value of the tensile strain for which the absorption is polarization independent. The polarization dependence of absorption spectra for InAs/GaAs cylindrical quantum dot is shown in Fig. 2.10

2.10 Kerr effect and Pockels effect

In this Thesis, we are primarily concerned with the electro-refraction in nanostructures due to the QCSE and/or carrier depletion. We should however also consider the Pockels effect, which is present in semiconductor structures of any dimensionality. The optical properties of an anisotropic crystal can be described by the refractive index ellipsoid. The shape of the index ellipsoid in the presence of an electric field, when not referred to its principal axis, has the general form, [31]

$$\left(\frac{1}{n^2}\right)_1 x_i^2 + \left(\frac{1}{n^2}\right)_2 x_j^2 + \left(\frac{1}{n^2}\right)_3 x_k^2 + 2\left(\frac{1}{n^2}\right)_4 x_i x_j + 2\left(\frac{1}{n^2}\right)_5 x_j x_k + 2\left(\frac{1}{n^2}\right)_6 x_i x_k = 1 \qquad (2.38)$$

where x_i, x_j, x_k are the principal dielectric axis. The impermeability tensor $(1/n^2)_\alpha$ depends on the distribution of charges in the crystal. The application of an electric field results in a redistribution of bond charges and possibly a slight deformation of the lattice. This redistribution of charges results in the electro-optic effect.

In addition to the Pockels effect, a quadratic dependence of the index of refraction on the electric field is also observed. This effects is known to be the Kerr effect, which can be expressed as

$$\Delta\left(\frac{1}{n^2}\right)_\alpha = \sum_{k,l=x,y,z} s_{\alpha kl} F_k F_l \qquad (2.39)$$

In a Zinc-Blend crystal, which belongs to the $\overline{4}3m$ crystal symmetry group, only the electro-optic tensor component r_{41} is required for the Pockels effect while s_{11} and s_{12} are required for Kerr effect. [31]. If n_0 is the refractive index in the absence of an electric field, and $r_{41}E_z << n_0^{-2}$, the refractive index variation due to Pockels effect can be written as

$$n_x^{'} = n_0 - \frac{1}{2} n_0^3 r_{41} E_z \qquad (2.40)$$

$$n_y^{'} = n_0 + \frac{1}{2} n_0^3 r_{14} E_z \qquad (2.41)$$

$$n_z^{'} = n_0 \qquad (2.42)$$

Hence for the structures grown in (100) substrate TE polarized light will experience a refractive index enhancement while propagating in the $[110]$ direction and a refractive index reduction while propagating in the $[1\bar{1}0]$ direction. The Pockels effect for the TM polarized wave is zero.

For the Kerr effect, both TE and TM-polarized waves experience a refractive index variation.

$$\Delta n_{TM} = \frac{1}{2} s_{11} n_0^3 E_z^2 \tag{2.43}$$

and

$$\Delta n_{TE} = \frac{1}{2} s_{12} n_0^3 E_z^2 \tag{2.44}$$

Since the origin of the Pockels effect and the QCSE are completely different, both effects are additive and we have to add the Pockels effect to our calculated electro-refraction in order to calculate for example the switching voltage. Ghosh et.al. [32] have measured the electro-optic coefficients of InAs/GaAs self-assembled quantum dots in a single mode ridge waveguide structure. They obtained a value of 2.438x10^{-10} m/V for r_{41} and 3.37x$10^{-17}$$m^2/V^2$ for s_{12}. Qasaimeh et.al [33] measured the electro-optic coefficients in self-organized $In_{0.4}Ga_{0.6}As/GaAs$ quantum dots. They obtained r =2.58x10^{-11} m/V and s =6.23x$10^{-17}$$m^2/V^2$, respectively. These values are much larger than the bulk values. Hence an enhanced electro-optic effect is observed in quantum dots. In the case of GaAs/AlGaAs quantum well, Glick et.al [34] have measured values of r and s as -1.6x10^{-12} m/V and 6x10^{-20} m^2/V^2 respectively. Zucker et.al [35] reported values of r=5.4x10^{-12} m/V and s=–3.01x10^{-18} m^2/V^2, respectively at a wavelength of 1.537 µm, in a high quality $In_{1-x}Ga_xAs_yP_{1-y}/InP$ quantum well.

References

1. "A one-dimensional "superlattice" in semiconductors" L. Esaki, L.L. Chang and R. Tsu, in *Proc.12th Int. Conf. Low Temp. Phys*., Kyoto, Japan, pp 551-553, 1970
2. "Quantum theory of cyclotron resonance in semiconductors: general theory", J.M. Luttinger, Phys. Rev, vol. 102, pp1030-1041, 1956
3. "Band gap versus composition and demonstration of Vegards's law for $In_{1-x}Ga_xAs_yP_{1-y}$ lattice matched to InP", R.E. Nahory, M.A. Pollack, W.D. Johnston, R.L. Barns, Appl. Phys. Lett., vol. 33, pp 659-661, 1978
4. "Theory of Optical Processes in semiconductors", P.K. Basu, Oxford Science publications, 1997
5. "Strain distribution and electronic spectra of InAs/GaAs self-assembled dots: an eight-band study" H. Jiang, J. Singh, Phys. Rev. B, vol. 56, pp 4696-4701, 1997
6. "Development of an eight-band theory for quantum dot heterostructures", E.P. Pokatilov, V.A. Fonoberov, V.M. Fomin, J.T. Devreese, Phys. Rev. B, vol. 64, pp 245328-1-245328-16, 2001
7. "Optical absorption in the presence of a uniform field", K. Tharmalingam, Phys. Rev., vol. 130, pp 2204-2206, 1963
8. "Theoretical investigation of superlattice band structure in the envelope-function approximation", G. Bastard, Phys. Rev. B, vol. 25, pp 7584-7597, 1982
9. "Determination of the lattice constant of epitaxial layers of III-V compounds", J. Hornstra and W.J. Bartels, J. Cryst. Growth, vol. 44, pp 513-517, 1978
10. "Eigenfunction-expansion method for solving the quantum-wire problem: Formulation", G.A. Baraff and D. Gershoni, Phys. Rev. B, vol. 43, pp 4011-4022, 1991
11. "Effective-mass theory for InAs/GaAs strained coupled quantum dots", S.S. Li, J.B. Xia, Z.L. Yuan, Z.Y. Xu, W. Ge, X.R. Wang, Y. Wang, Y. Wang, and L.L. Chang, Phys. Rev. B, vol. 54, pp 11575-11581, 1996
12. "Quantum theory of cyclotron resonance in semiconductors: General theory", J.M. Luttinger, Phys. Rev., vol. 102, pp 1030-1041, 1956
13. "Presentation and experimental validation of a single-band, constant-potential model for self-assembled InAs/GaAs quantum dot", M. Califano, P. Harrison, Phys. Rev. B, vol. 61, pp 10959-10965, 2000

14. "Superlattice band structure in the envelope-function approximation", G. Bastard, Phys. Rev. B, vol.24, pp 5693-5697, 1981
15. "Electro-absorption by Stark effect on room-temperature excitons in GaAs/GaAlAs multiple quantum well structures", D.S. Chemla, T.C. Damen, D.A.B. Miller, A.C. Gossard, W. Wiegmann, Appl. Phys. Lett., vol. 42, pp 864-866, 1983
16. "Condensation effect of excitons", E. Hanamura, and H. Haug, Phys. Report, vol. 33, pp 209-284, 1977
17. "Wannier excitons in low-dimensional microstructures: Shape dependence of the quantum size effect", Y. Kayanuma, Phys. Rev. B, vol. 44, pp 13085-13088, 1991
18. "Ultra narrow luminescence lines from single quantum dots", M. Grundman, J. Cristen, N.N. Ledentsov, J. Bohrer, D. Bimberg, S.S. Ruvimov, P. Werner, R. Ritcher, U. Gosele, J. Heydenreich, V.M. Ustinov, A.Yu. Egorov, A.E. Shukov, P.S. Kop'ev, Zh.I. Alfereov, Phys. Rev. Lett., vol. 74, pp 4043-4046, 1995
19. "Theory of the linear and nonlinear optical properties of semiconductor microcrystallites", S. Schmitt-Rink, D.A.B. Miller, D.S. Chemla, Phys. Rev. B, vol. 35, pp 8113-8125, 1987
20. "The theory of strained-layer quantum-well lasers with bandgap renormalization", D. Ahn, S.L. Chuang, IEEE. J. Quantum. Electron., vol. 30, pp 350-364, 1994
21. "Bandgap shrinkage in GaInAs/GaInAsP/InP multi-quantum well lasers", S.H. Park, J.I. Shim, K. Kudo, M. Asada, S. Arai, J. Appl. Phys., vol. 72, pp 279-281, 1992
22. "Theoretical and experimental studies of optical absorption in strained quantum-well structures for optical modulators", S.C. Hong, G.P. Kothiyal, N. Debbar, P. Bhattacharya, J. Singh, Phys. Rev. B, vol. 37, pp 878885, 1988
23. "Electronic state and optical transitions in solids", F. Bassani, G.P. Parravicini, R.A. Ballinger, Oxford: Pergamon, 1975
24. "Quantum dots", L. Jacak, P. Hawrylak, A. Wojs, Springer, 1997
25. "Electronic structure of cubic lattice quantum dots", S.S. Li, J.B. Xia, J. Appl. Phys., vol. 84, pp 3710-3713, 1998
26. "Broadening factor due to electron-phonon collisions in semiconductor quantum wells", M.P. Houng, Y.H. Wang, C.H. Chu, J. Appl. Phys., vol. 77, pp 6338-6344, 1995
27. "Theoretical and experimental study of the optical-absorption spectrum of exciton resonance in $InGa_{0.53}As_{0.47}/InP$ quantum wells", M. Sugawara, T. Fujii, S. Yamazaki, K. Nakajima, Phys. Rev. B, pp 9587-9597, 1990

28. "Theoretical and experimental studies of optical absorption in strained quantum-well structures for optical modulators", S.C. Hong, G.P. Kothiyal, N. Debbar, P. Bhattacharya, J. Singh, Phys. Rev. B, vol. 37, pp 878885, 1988
29. "Dephasing in InAs/GaAs quantum dots", P. Borri, W. Langbein, J. Mork, J.M. Hvam, F. Heinrichsdorff, M.-H. Mao, and D. Bimberg, Phys. Rev. B., vol. 60, pp 7784-7787, 1999
30. "Wave mechanics applied to semiconductor heterostructures", G. Bastard, Les editions de physique, France, 1988
31. "Quantum Electronics", A. Yariv, John Wiley, New York, 1967
32. "Nonlinear optical and electro-optic properties of InAs/GaAs self –organized quantum dots", S. Ghosh, A.S. Lenihan, M.V.G. Dutt, O. Qasaimeh, D.G. Steel, P. Bhattacharya, J. Vac. Sci. Technology. B., vol. 19, pp 1455-1458, 2001
33. "Linear and quadratic electro-optic coefficients of self-organised $In_{0.4}Ga_{0.6}As/GaAs$ quantum dots", O. Qasaimeh, K. Kamath, P. Bhattacharya, J. Phillips, Appl. Phys. Lett., vol. 72, pp 1275-1277, 1998
34. "Quadratic electro-optic light modulation in GaAs/AlGaAs multiple quantum well heterostructure near the excitonic gap", M. Glick, F.K. Renihart, G. Weimann, W. Schlapp, Appl. Phys. Lett, vol. 49, pp 989-991, 1986
35. "Quarternary quantum wells for electro-optic intensity and phase modulation and 1.3 and 1.55µm", J.E. Zucker, Bar-Joseph, B.I. Miller, U. Koren, D.S. Chemla, Appl. Phys. Lett., vol.54, pp 10-12, 1989

APPENDIX

Electron states:

Using the electron wavefunction given by Eq. 2.10, the matrix elements of Hamiltonian given by Eq. 2.7 can be written as

$$\langle H\rangle_{ij}=\left[\frac{\hbar^2}{2m_2^*}\delta_{nn'}\delta_{mm'}\delta_{ll'}+\frac{\hbar^2}{2m_{12}^*}\langle S\rangle_{ij}\right]\left(k_{nx}k_{n'x}+k_{my}k_{m'y}+k_{lz}k_{l'z}\right)+$$
$$\left(\delta_{nn'}\delta_{mm'}\delta_{ll'}-\langle S\rangle_{ij}\right)\left(V_{e0}+a_c\varepsilon_{hy}\right)+F_{ll'}$$

where

$$\langle S\rangle_{ij}=\frac{1}{\sqrt{L_xL_yL_z}}\iiint e^{i(K_{nn'}x+K_{mm'}y+K_{ll'}z)}dxdydz$$

and the contribution $F_{ll'}$ due to the applied electric field F is

$$F_{ll'}=\begin{cases}0 & for\quad l=l'\\ \dfrac{ieF\cos(\pi(l-l'))L_z}{2\pi(l-l')} & for\quad l\neq l'\end{cases}$$

in which the effective masses are expressed as

$1/m_{12}^*=1/m_1^*-1/m_2^*$,

and the components of the k-vector read

$k_{nx}=(k_x+nK_x)$, $k_{n'x}=(k_x+n'K_x)$ etc,

and finally

$K_{nn'}=(n-n')(2\pi/L_x)$

Hole states:

Using the plane wave functions given by Eq. 2.25, the matrix elements of $P_\pm$, $Q_\pm$, R, C, ($a_v\varepsilon_{hy}$ +V_h) and (-eFz) within the hole Hamiltonian (Eq. 2.11) can be expressed as

$$(P_\pm \mp \varepsilon_{sh})_{nml,n'm'l'} = \left(\gamma_\pm^1 \delta_{nn'}\delta_{mm'}\delta_{ll'} + \gamma_\pm^2 \langle S\rangle_{ij}\right)\left(k_{nx}k_{n'x} + k_{my}k_{m'y}\right) + \left(\gamma_\pm^3 \delta_{nn'}\delta_{mm'}\delta_{ll'} + \gamma_\pm^4 \langle S\rangle_{ij}\right)\left(k_{lz}k_{l'z}\right) \mp \varepsilon_{sh0}\langle S\rangle_{ij}$$

$$(Q_\pm) = 2\sqrt{3}\{[(\sigma_2-\delta_2)\delta_{nn'}\delta_{mm'}\delta_{ll'} - (\sigma_1-\delta_1-\sigma_2+\delta_2)\langle S\rangle_{ij}] (k_{n'x} \pm k_{m'y})k_{lz} + [\pi_2\delta_{nn'}\delta_{mm'}\delta_{ll'} - (\pi_1-\pi_2)\langle S\rangle_{ij}](k_{nx} \pm ik_{my})k_{l'z}\}$$

$$R_{nml,n'm'l'} = \sqrt{3}\{[\mu_2\delta_{nn'}\delta_{mm'}\delta_{ll'} - (\mu_1-\mu_2)\langle S\rangle_{ij}](k_{nx}+ik_{my})(k_{n'x}+ik_{m'y}) - [\gamma^2\delta_{nn'}\delta_{mm'}\delta_{ll'} - (\gamma^1-\gamma^2)\langle S\rangle_{ij}](k_{nx}-ik_{my})(k_{n'x}-ik_{m'y})\}$$

$$C_{nml,n'm'l'} = 2(\sigma_1-\delta_1-\pi_1-(\sigma_2-\delta_2-\pi_2))\langle S\rangle_{ij}[(k_{nx}-ik_{my})k_{l'z} - (k_{n'x}-ik_{m'y})k_{lz}]$$

$$(a_v\varepsilon_{hy}+V_h)_{nml,n'm'l'} = a_v\varepsilon_{hy}\langle S\rangle_{ij} + (\delta_{nn'}\delta_{mm'}\delta_{ll'} - \langle S\rangle_{ij})V_{h0}$$

$$(-eFz)_{nml,n'm'l'} = F_{l,l'}$$

in which the Luttinger parameters are

$$\gamma_\pm^1 = \gamma_{21} \pm \gamma_{22} \quad \gamma_\pm^2 = (\gamma_{11} \pm \gamma_{12}) - \gamma_\pm^1 \quad \gamma_\pm^3 = \gamma_{12} \mp 2\gamma_{22} \quad \gamma_\pm^4 = (\gamma_{11} \mp 2\gamma_{12}) - \gamma_\pm^3$$

$$\sigma_i - \delta_i = (-1-\gamma_{i1}+2\gamma_{i2}+6\gamma_{i3})/6 \qquad \pi_i = (1+\gamma_{i1}-2\gamma_{i2})/6$$

$$\gamma^i = (\gamma_{i2}+\gamma_{i3})/2 \quad \mu_i = -(\gamma_{i2}-\gamma_{i3})/2 \quad \sigma_i - \delta_i - \pi_i = (-1-\gamma_{i1}+2\gamma_{i2}+3\gamma_{i3})/3$$

For square and cylindrical quantum dots, the $\langle S\rangle_{ij}$ term can be solved analytically. For square (etched) quantum dots the $<S>_{ij}$ term become $S_nS_mS_l$ where

$$S_n = \begin{cases} \dfrac{L}{L_x}\, for \quad n = n' \\[2ex] \dfrac{\sin[\pi(n-n')\dfrac{L}{Lx}]}{\pi(n-n')}\, for \quad n \neq n' \end{cases}$$

$$S_m = \begin{cases} \dfrac{L}{L_y} \, for \quad m = m^{'} \\ \dfrac{\sin[\pi(m-m^{'})\dfrac{L}{L_y}]}{\pi(m-m^{'})} \, for \quad m \neq m^{'} \end{cases}$$

$$S_l = \begin{cases} \dfrac{L}{L_z} \, for \quad l = l^{'} \\ \dfrac{\sin[\pi(l-l^{'})\dfrac{L}{L_z}]}{\pi(l-l^{'})} \, for \quad l \neq l^{'} \end{cases}$$

Self-assembled quantum dots can be approximated as cylinders or discs. In that case, <S>$_{ij}$ can be easily solved in the cylindrical coordinate system. If we consider the length of the cylinder in the z direction to be L_z and the radius R, the <S>$_{ij}$ term becomes equal to $S_{nm}S_l$ with

$$S_{nm} = \begin{cases} \dfrac{\pi R^2}{L_x^2} \, for \quad n = n^{'} \; and \quad m = m^{'} \\ \dfrac{R}{\lambda L_x} J_1(\lambda K_x R) \, for \quad n \neq n^{'} \; and \quad m \neq m^{'} \end{cases}$$

$$S_l = \begin{cases} \dfrac{L}{L_z} \, for \quad l = l^{'} \\ \dfrac{\sin[\pi(l-l^{'})\dfrac{L}{L_z}}{\pi(l-l^{'})} \, for \quad l \neq l^{'} \end{cases}$$

where $\lambda = \sqrt{(n-n^{'})^2 + (m-m^{'})^2}$

These analytical equations significantly reduce the computation time.

Chapter 3

An ultra-short MZI space switch based on a composite quantum well

"…There are certain situations in which the peculiarities of quantum mechanics can come out in a special way on large scale"

Richard Feynman

3.1 Introduction

Many attempts have been made by researchers to further miniaturize photonic components such as a Mach-Zehnder Interferometric (MZI) space switch. Semiconductor nanostructures provide several possibilities for such a miniaturization by tailoring the nonlinear optical properties towards a high switching efficiency. In Maat et.al [1], the combination of the Pockels effect and the carrier depletion effect have been employed by using a bulk quaternary layer doped up to $6.10^{17}/\mathrm{cm}^2$ as the active switching medium. Kimura et.al [2] measured a large refractive index variation of 0.016 in a tensile strained InGaAs/InGaAsP multiple quantum well with a carrier density of the order of $10^{13}/\mathrm{cm}^2$. However, these high carrier densities also result in a very high free-carrier absorption. Dorren et.al. [3] suggested a chopped quantum well, in which the magnitude of the Quantum Confined Stark Effect (QCSE) and the operating wavelength could be separately optimized. Dorren et.al. showed that the phase shifter length could be reduced down to 0.64 mm in an MZI-switch in push-pull operation, at the expense of a 11 V switching voltage. Asymmetrically coupled InGaAs/InP [4,5] quantum wells do provide a new degree of freedom for optimizing the QCSE at the required wavelength region. This chapter presents an asymmetric n-doped InGaAs/InAsP/InP quantum well. This structure is indirect in real space, thus providing either a red shift or a blue shift [6] depending on the polarity of the applied electric field. In addition, we combined the carrier depletion effect and electro-refraction due to QCSE in this structure. The combination of the QCSE and the carrier depletion effect in a quantum well is very useful for optimizing the switching voltage at one hand and maintaining a low waveguide loss at the other hand. Finally, in an InGaAs/InAsP quantum well, the InAsP layer is compressively strained while the InGaAs layer is tensile strained, which will provide both polarization independence and strain balancing [7].

3.2 Calculation of the electro-absorption and electro-refraction in coupled quantum wells

As discussed in Chapter 2, the conduction band in III-V semiconductor quantum well materials is well separated from the valence band. Hence we can use a parabolic dispersion relation, which is given by

$$E_n(k) = E_n(0) + \frac{\hbar^2 k_{\|}^2}{2m_{well}^*} \tag{3.1}$$

where m_{well}^* is the effective electron mass in the plane of quantum well. The electron confinement energies and the envelope functions can be calculated from the equation 2.7

The interaction between the light hole and heavy hole states leads to a non-parabolic dispersion relation given by the 4X4 Luttinger-Kohn formalism, as explained in Chapter 2

$$H_0 = \begin{bmatrix} H_{hh} & b & c & 0 \\ b^* & H_{lh} & 0 & -c \\ c^* & 0 & H_{lh} & b \\ 0 & -c^* & b^* & H_{hh} \end{bmatrix} \tag{3.2}$$

where

$$H_{hh} = E_{v,hh}(z) - \frac{\hbar^2}{2m_0}\left[(\gamma_1+\gamma_2)(k_x^2+k_y^2) - (\gamma_1-\gamma_2)k_z^2\right] \tag{3.3}$$

$$H_{lh} = E_{v,hh}(z) - \frac{\hbar^2}{2m_0}\left[(\gamma_1-\gamma_2)(k_x^2+k_y^2) - (\gamma_1+\gamma_2)k_z^2\right] \tag{3.4}$$

$$b = \frac{\sqrt{3}\hbar^2}{2m_0}\left[\gamma_2\left(k_x^2-k_y^2\right) - 2i\gamma_3 k_x k_y\right] \tag{3.5}$$

$$c = \frac{\sqrt{3}\hbar^2}{2m_0}\gamma_3\left(-k_x - ik_y\right)k_z \tag{3.6}$$

At the zone center, the light hole and heavy hole mixing is zero and hence the values of b and c also become zero. Hence, at the zone center the matrix becomes diagonal. Away from the zone center the light hole and heavy hole states start mixing and produce non-parabolic dispersion relations.

The electro-absorption and electro-refraction can be obtained from the optical susceptibility [8, 9]. Using the density matrix formalism the optical susceptibility can be written as

$$\chi(\omega)=\sum_{n}\sum_{J}\int_{E_g+E_{cn}+E_{vn}^J} dE\overline{C}(E)\rho_r^J M_J^2[f_{cn}^J(E)-f_{vn}^J(E)]\left(\frac{i}{\pi}\right)\frac{\hbar/\tau_{in}-i(E_{ph}-E)}{(E_{ph}-E)^2+\left(\hbar/\tau_{in}\right)^2} \tag{3.7}$$

where E_{ph} is the photon energy, E is the transition energy and τ_{in} is the inter-band relaxation time. M_J is the momentum matrix element as determined in the framework of the 4x4 Luttinger Kohn matrix for the transition from the n^{th} light hole (LH) or heavy hole (HH) subband in the valence band to the n^{th} subband in the conduction band. J represents the hole subband type. f_{cn}^J and f_{vn}^J are the corresponding Fermi-Dirac distribution functions for the n^{th} conduction and valence band, respectively and ρ_r^J is the density of states. The constant $\overline{C}(E)=\hbar\pi e^2/\left(m_0^2 k_0 c_0 \varepsilon_0 E\right)$, where m_0, k_0, and ε_0 are the free electron mass, vacuum wave number, and susceptibility, respectively. The absorption and the refractive index change due to the QCSE and carrier induced effects, using the bulk refractive index n_r, is

$$\alpha=-(k/n_r)\,\mathrm{Im}(\chi) \tag{3.8}$$

$$\delta n=(1/2n_r)\,\mathrm{Re}(\chi) \tag{3.9}$$

These two parameters are connected through the well-known Kramers-Kroning relation. Hence we can calculate the index of refraction change (δn) from the absorption change (δα) due to the QCSE or the carrier depletion effect.

$$\delta n(\omega)=\frac{c}{\pi}P\int_{\omega_1}^{\omega_2}\frac{\delta\alpha(\omega')}{(\omega')^2-(\omega)^2}d\omega \tag{3.10}$$

where c is the vacuum speed of light. From this relation it is clear that within a spectral range [ω_1 ω_2], a local change in absorption leads to a refractive index variation over the entire spectrum. The refractive index change is high near to the maximum of the electro-absorption $\delta\alpha$ (ω) spectrum and decreases inversely proportional with the detuning ω'-ω.

The Hamiltonians, in the case with and without an applied electric field, operate on the same Hilbert space. Moreover, the two sets of orthonormal eigenfunctions span the same space. This leads to a sum rule [19], which states that the integrated surface area under the absorption spectra remains constant irrespective of the applied electric field

$$\Delta A = \int_0^{\infty} \left[\alpha_f(\omega) - \alpha_0(\omega)\right] d\omega = 0 \qquad (3.11)$$

Hence a positive absorption change at some spectral region will always be compensated by a negative absorption change at another spectral region. In the QCSE, the red shift of the bandgap will contribute positively while the decreased oscillator strength will contribute negatively to the electro-refraction. These contributions of opposite sign demand for a large enough integration range for calculating the refractive index variation using the Kramers-Kroning relations.

3.3 $In_{1-x}Ga_xAs$/InP quantum wells

The well-known properties of InGaAs/InP strained quantum wells attracted much attention for device design [10,11]. Since $In_{0.53}Ga_{0.47}As$ is lattice matched to InP, a higher Ga composition will produce tensile strain and a lower Ga composition produces compressive strain. In this material system, the ease in growing strained epitaxial layers of several monolayers on an InP substrate allows to shift the heavy-hole exciton transition relative to the light-hole exciton transition. Tensile strain will lift the otherwise lower lying light-hole states above the heavy-hole state. We will use this behavior to produce a polarization insensitive switching in a composite quantum well. Because $In_{0.53}Ga_{0.47}As$ is lattice matched to InP, the bandgap can be tuned over a wide wavelength range by adjusting the quantum well thickness. Since the QCSE is in a simple model proportional to the well thickness to the fourth power, a large QCSE can easily be achieved with this material system [12]. However, waveguide transparency requires that the well width is limited to below 3.5 nm, for obtaining a low-loss waveguide at 1550 nm [3]. Such a small maximum allowed quantum well thickness seriously limits the QCSE. A better design is required to enhance the refractive index variation within the limits of the allowed waveguide loss.

3.4 $InAs_xP_{1-x}/InP$ quantum wells.

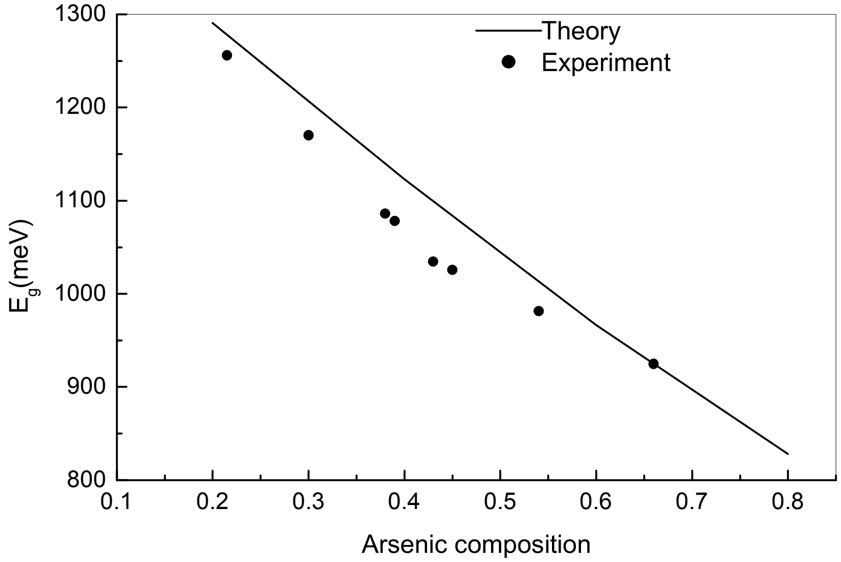

Figure 3.1: Theoretical and experimental curves showing the band gap variation with arsenic composition in a 4nm InAsP/InP quantum well at 4K

$InAs_xP_{1-x}/InP$ is a promising material for device applications in the 1.55 μm region. In particular, the large conduction band-offset ratio is expected to provide novel opportunities for device design. Relatively few studies have been performed to the pseudomorphic $InAs_xP_{1-x}/InP$ system. All material parameters of InAsP can be approximately obtained by linear interpolation of the InAs and InP parameters [13], except the band offset, which has been reported to be 70:30 [14, 15]. High quality InAsP/InP multiple quantum wells can be grown by chemical beam epitaxy. PL measurements show a wide tunability of the bandgap by changing the well width or the strain by changing the composition. Good agreement between the measured bandgap and the interpolated values are obtained as shown in Figure 3.1. The InAs interface layers which in particular appear at high arsenic concentration, greatly influence the transition energies especially in narrow quantum wells [16]. In our structure, we used $InAs_{0.65}P_{0.35}$ quantum wells with an in plane compressive strain of 2%. Such a high strain yields a critical layer thickness of 3.5 nm.

3.5 InGaAs-InP-InAsP composite quantum wells

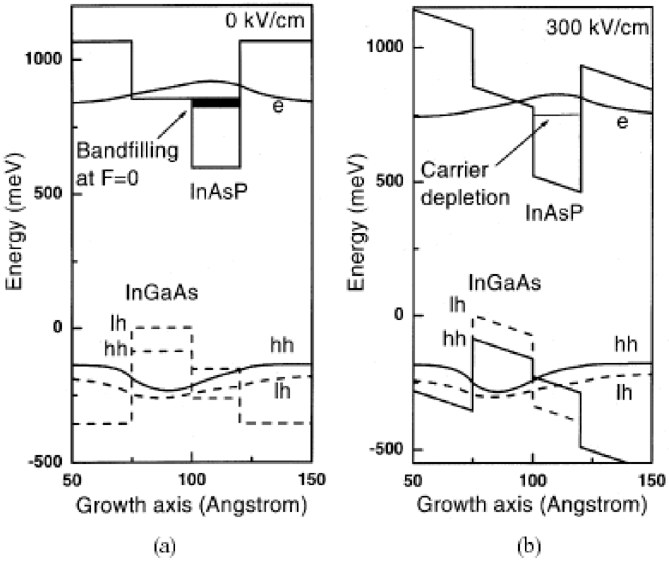

Figure 3.2 : Indirect in real-space InGaAs-InAsP quantum well showing the lowest lying envelope functions of the electrons and heavy holes (solid lines) and light holes (dotted lines) at (a) zero bias and (b) at 300kV/cm. At zero bias, bandfilling due to n-type doping is schematically included. An applied field results in both carrier depletion and the QCSE, which shifts the electron-heavy hole transition energy down by 50meV. The heavy-hole and light-hole confining potentials are also shown. The band offset is 40:60 in InGaAs and 70:30 in InAsP. The polarization independence is achieved by tensile strain in InGaAs layer

Coupled quantum wells provide a higher degree of freedom for optimising the QCSE. Hence, we investigate “indirect in real space (IRS)” (figure. 3.2) InGaAs/InP/InAsP quantum wells [17] which can be grown between InP barriers. In these quantum wells, the lowest electron level is confined in the $InAs_xP_{1-x}$ layer which has a conduction band offset of 70%, while the highest hole state is confined inside the $In_{1-y}Ga_yAs$ layer which has a valence band offset of 60%. As a consequence, this quantum well is indirect in real space, resulting in a linear Stark shift which is proportional to the product of the external applied field times the average electron-hole separation. Another advantage of these layers is that they exhibit both a red shift and a blue shift [6], depending on the sign of the applied electric field (Fig. 3.3). The QCSE in this quantum well depends on the total well width, the asymmetry of the wells and the width of the InP barrier layer.

In this coupled quantum well, the compressively strained $InAs_xP_{1-x}$ layer will balance the tensile strain of the tensile strained $In_{1-y}Ga_yAs$ quantum well. Since the holes are confined in the tensile strained $In_{1-y}Ga_yAs$ layer, the InGaAs layer primarily determines the polarization behavior and polarization insensitivity can be obtained by applying tensile strain. The coupled quantum well thus allows a separate optimization of the polarization behaviour, the average electron-hole separation and the transition energy.

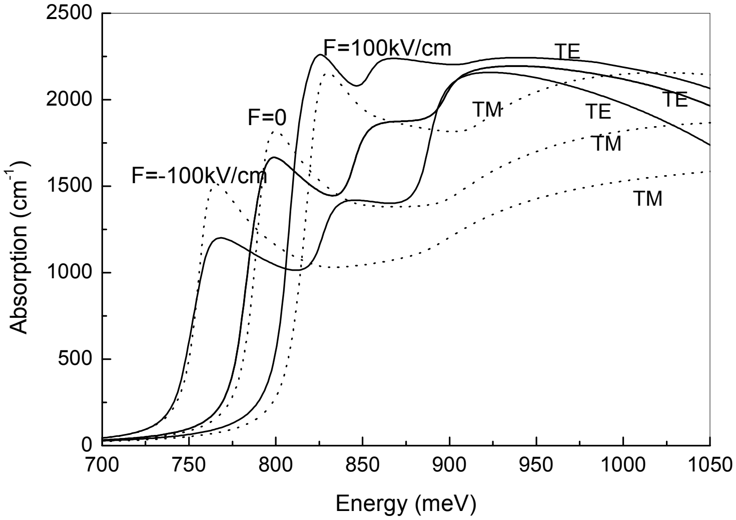

Figure 3.3 : Absorption spectra of a 4nm $In_{0.38}Ga_{0.62}As$/3.7nm $InAs_{0.65}P_{0.35}$/InP composite quantum for TE (solid) and TM (dotted) polarization. With this "indirect in real space" coupled quantum well, both a blue shift and a red shift can be realized.

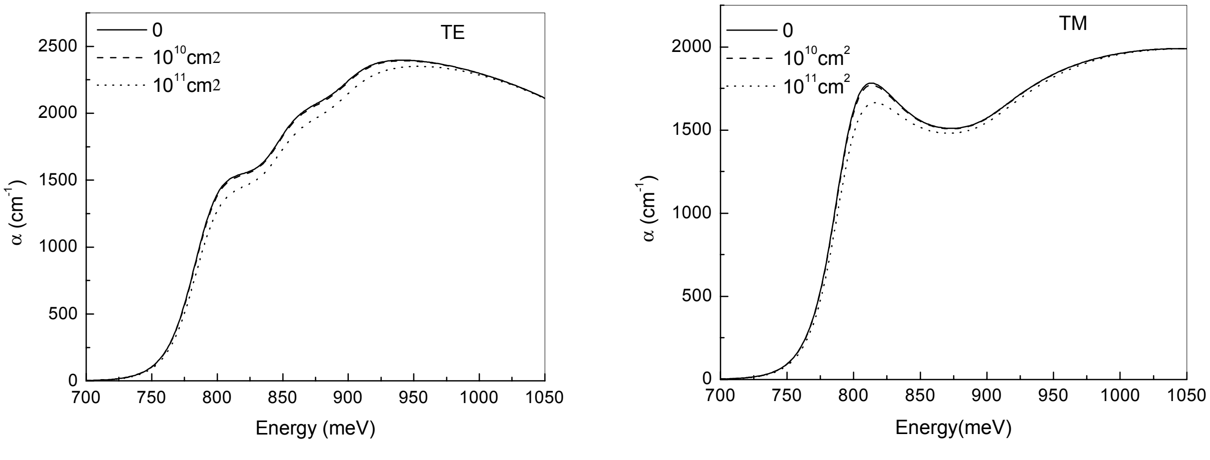

Figure 3.4 : Carrier induced TE and TM absorption change in 4nm $In_{0.38}Ga_{0.62}As$/3.7nm $InAs_{0.65}P_{0.35}$/InP quantum well.

3.6 Design criteria

For achieving an efficient and compact phase shifting region operating at a low bias voltage, the first design issue is the enhancement of the electro-refraction. Polarization independent electro-refraction is a second design criterion, which can be realized by applying tensile strain to the InGaAs quantum well. A third design criterion is wave-guide transparency at 1550nm in the quantum well material, which requires an effective bandgap below 1400 nm [18]. A high electro-absorption in the material results in a high refractive index variation. But the electro-absorption is also a parasitic effect, which leads to an intensity imbalance between the two arms of the MZI switch, which ends up in crosstalk. As a fourth design criterion, we choose to limit the crosstalk to below –25 dB.

We choose to limit the excess waveguide absorption loss due to a combination of inter-band absorption in the Urbach tail and free carrier absorption to 0.5 dB/cm. Consequently, the doping inside the quantum well material within the waveguide core should remain limited to below $2.10^{11}/\mathrm{cm}^2$, assuming that the waveguide core is filled up with 50 quantum wells. For this carrier density, the index of refraction variation due to the combined effect of bandfilling at zero field and carrier depletion at an applied field is comparable to the index of refraction variation due to the QCSE.

3.7 Electro-refraction due to the QCSE

For optimizing the index of refraction variations in doped quantum wells, the QCSE and the bandfilling effects should be independently optimized. The QCSE will produce either a red shift or a blue shift in the absorption spectra (Fig. 3.3), where as bandfilling effect produces a blue shift (Fig. 3.4). In this paragraph, we will first consider the QCSE only. Since the magnitude of the Stark shift in IRS coupled QW's is proportional to the average separation of the electron and hole wavefunctions, we first investigated the Stark shift and the magnitude of the electro-refraction in undoped $\mathrm{In_{0.38}Ga_{0.62}As}$(4nm)/InP/$\mathrm{InAs_{0.65}P_{0.35}}$(2.5 nm) quantum well as a function of the InP intermediate barrier.

It can be observed from Figure 3.5 that the QCSE red shift increases for an increasing InP barrier thickness since the effective separation of the electron and hole envelope function also increases. The electro-refraction however decreases for an increasing InP barrier as shown in

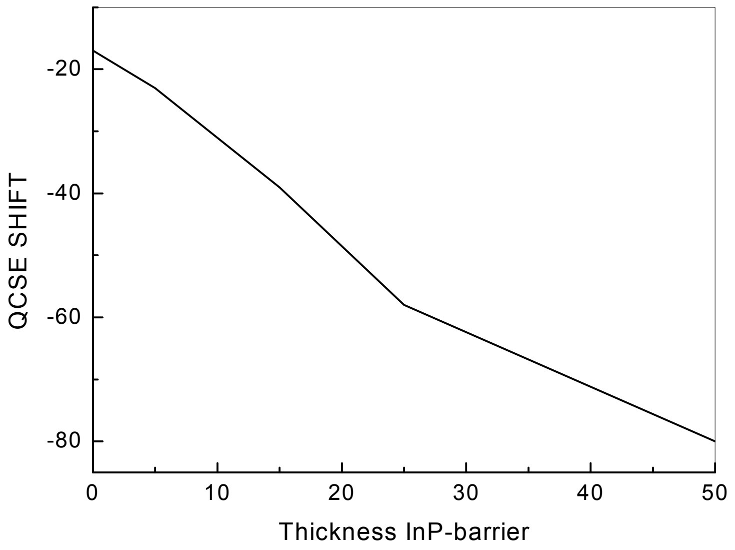

Figure 3.5 : The QCSE versus the InP intermediate barrier thickness in a (4nm) $In_{0.38}Ga_{0.62}As$-InP-$InAs_{0.65}P_{0.35}$(3.7 nm) composite quantum well at 100kV/cm

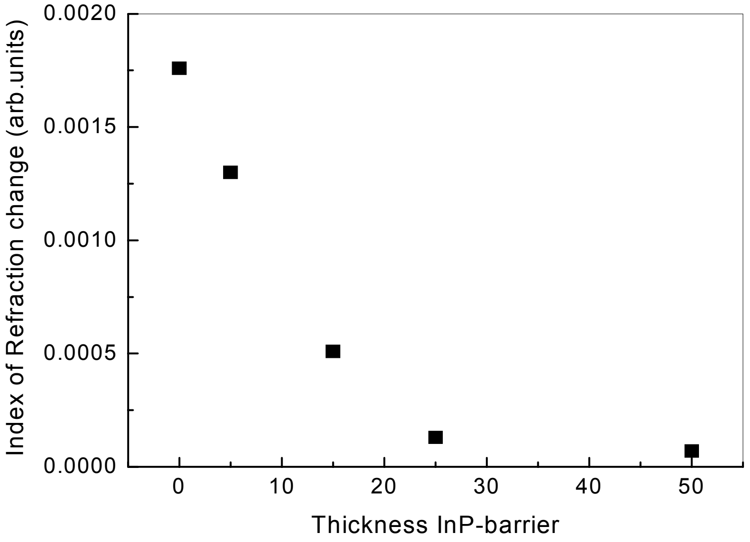

Figure 3.6 : The Electro-refraction versus the InP intermediate barrier thickness in a (4nm) $In_{0.38}Ga_{0.62}As$-InP- (3.7nm) $InAs_{0.65}P_{0.35}$ (3.7 nm) composite quantum well at 100 kV/cm

Figure 3.6, which is due to the strongly decreasing oscillator strength arising out of the decreasing overlap between the electron and hole envelope functions. It is also observed that a red shift generates a slightly larger electro-refraction than a blue shift at the same InP barrier thickness. For further calculations, we investigated a $In_{0.38}Ga_{0.62}As/InAs_{0.65}P_{0.35}$ quantum well with a zero InP barrier, as shown in Figure 3.2, since this structure yields the largest electro-refraction. The absorption spectra of this structure both at zero field and at an applied bias of 100 kV/cm is presented in Figure 3.7

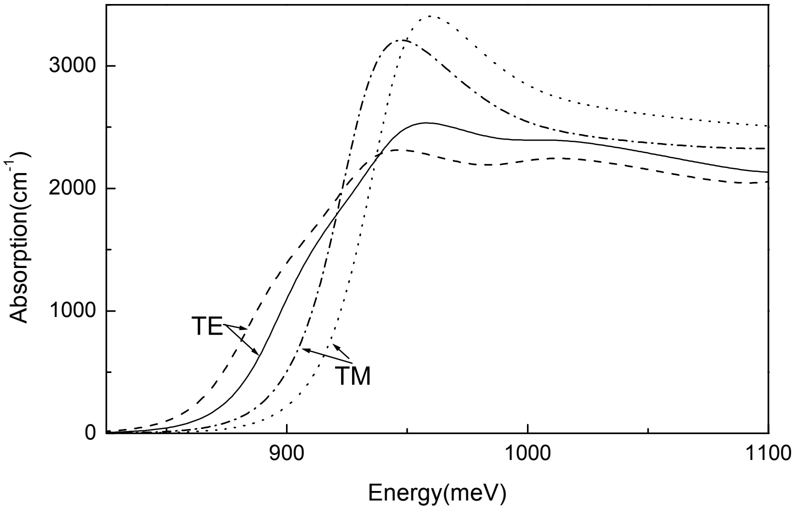

Figure 3.7 : TE and TM absorption spectrum of undoped (2.5nm) $In_{0.38}Ga_{0.62}As$-(2nm) $InAs_{0.65}P_{0.35}$ QW and a field of 0 and 100kV/cm

The electro-refraction of an undoped $In_{0.38}Ga_{0.62}As$ (2.5 nm) /$InAs_{0.65}P_{0.35}$ (2 nm) quantum well is shown in Figure 3.8. Since the hole levels are primarily confined inside the InGaAs layer, the polarization dependence of the electro-refraction is determined by the heavy–hole light-hole splitting inside the InGaAs well. A polarization independent behaviour can thus be realized by applying a tensile strain towards the InGaAs well, which can be compensated by a compressive strain inside the InAsP layer. We found that an $In_{0.38}Ga_{0.62}As$ layer yields an almost polarization independent behaviour of the electro-refraction. This effect is shown in figure 3.8 where we observe an approximately polarization independent electro-refraction at 827 meV (1500 nm) at an applied bias of 100 kV/cm. The operating wavelength of this structure has been determined by allowing an absorption loss of 0.2 dB/cm in the unbiased waveguides and an electro-absorption loss of 0.1dB/mm in the phase section of the Mach-Zehnder, assuming a confinement factor of

0.25. These losses can be read from the Urbach tail of the quantum well bandgap, which extends to lower energy as shown in the Figure 3.9. It should be emphasized that the excess waveguide loss and the electro-absorption loss play an entirely different role in the performance of an MZI space switch. The excess waveguide loss, which comes on top of the usual processing-induced scattering losses due to sidewall roughness, should be kept low to limit the excess loss in the input and output waveguides of the MZI. The electro-absorption loss will however introduce an imbalance within the MZI, which results into crosstalk. Dorren et.al [3] showed that 1 dB electro-absorption results in –25dB excess crosstalk, while 0.5 dB electro-absorption results in –31 dB excess crosstalk due to imbalance in the MZI. These excess crosstalk values will also come on top of the crosstalk due to light scattering at imperfections, crosstalk due to unwanted multimode behaviour of the waveguides and crosstalk due to processing induced imbalance of the MZI.

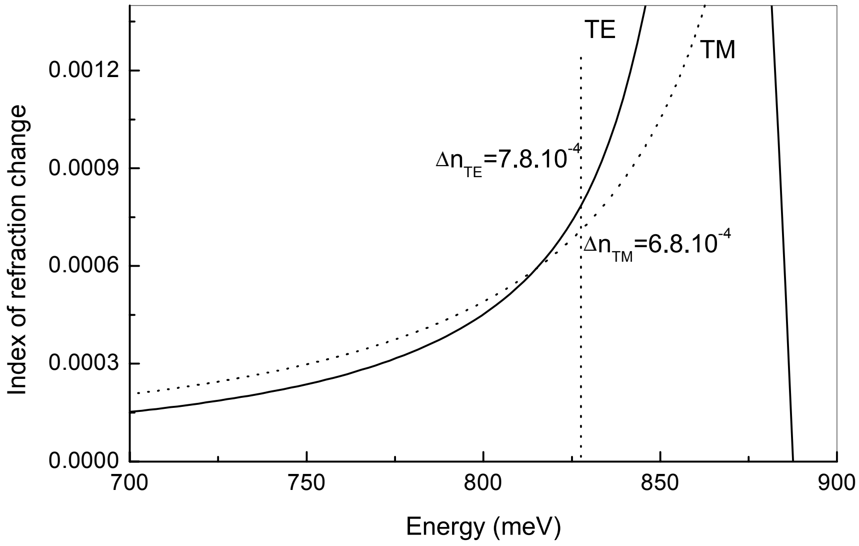

Figure 3.8 : Electro-refraction as a function of energy (wavelength) for an undoped (2.5nm) $In_{0.38}Ga_{0.62}As$-(2nm) $InAs_{0.65}P_{0.35}$ QW. At 827meV, the absorption loss is 0.2dB/cm as deduced from the Urbach tail of the absorption spectrum. TE electro-refraction is $7.8.10^{-4}$ and TM electro-refraction is $6.8.10^{-4}$ at 827meV for 100kV/cm

In order to estimate the length of the phase shifting section of the MZI, we assume a 10 nm InP barrier in between the $In_{0.38}Ga_{0.62}As$ (2.5 nm)/$InAs_{0.65}P_{0.35}$ (2 nm) quantum wells, resulting in a confinement factor of approximately 0.31. We also take into account the Pockels effect with an estimated r_{41} of -1.5×10^{-12} m/V, resulting in an index of refraction change of 2.5×10^{-5}/Volt over the entire waveguide core. All effects together result in a phase shifter length of 1.7 mm.

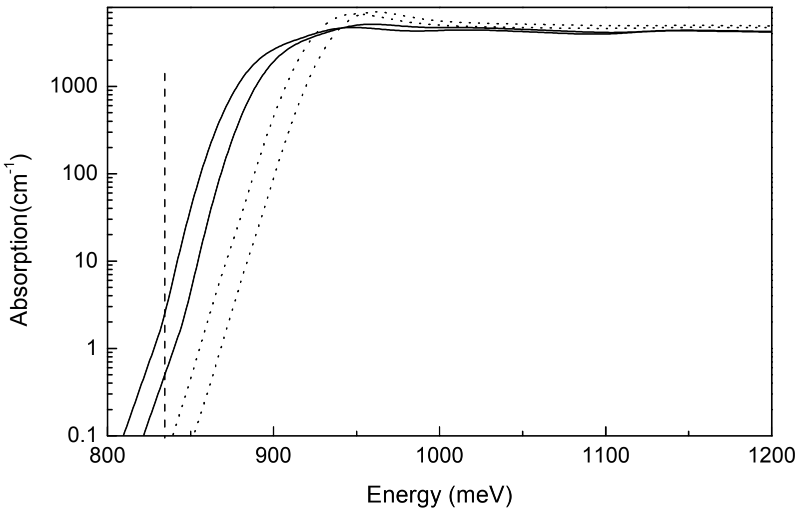

Figure 3.9: Urbach tail of the absorption spectra of (2.5nm) $In_{0.38}Ga_{0.62}As$- (2nm) $InAs_{0.65}P_{0.35}$ QW, for TE (solid) and TM (doted) polarization with zero field and 100 kV/cm (red shift). The operating wavelength is selected at 827 meV

3.8 Combination of the QCSE and carrier depletion

It is well-known that carrier depletion effects are able to generate large refractive index variations. Unfortunately, these refractive index variations are accompanied by free carrier absorption effects, which will deteriorate both the waveguide absorption loss and the imbalance-induced crosstalk in an MZI. It will be shown below, that the electro-refraction due to the QCSE and the electro-refraction due to carrier depletion are almost equal if one chooses to keep the total electro-absorption loss below approximately 0.5 dB. If one imposes the amount of electro-absorption, which is the source of imbalance induced crosstalk, as a boundary condition in the design of the quantum well material; it is necessary to optimise both the QCSE and the carrier depletion effects in a single structure. For investigating the combination of carrier depletion and the QCSE, we take $2.10^{11}/cm^2$ n-type doped InGaAs/InAsP quantum wells. These doped quantum wells will be fully depleted at an applied bias of 100 kV/cm. The field induced carrier depletion yields an effective red shift of the band edge, which adds to the red shift due to the quantum confined Stark effect as schematically shown in Figure 3.10.

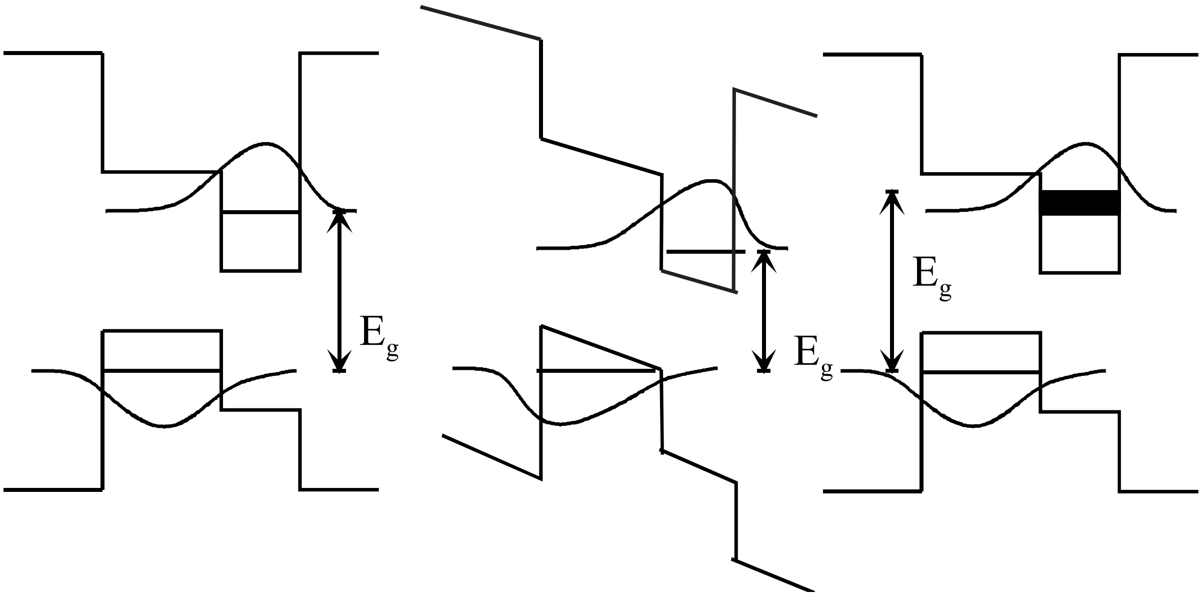

Figure 3.10: Schematic diagram illustrating the additional red shift due to carrier depletion in a composite quantum well. With carrier depletion, the effective bandgap changes from case (c) to (b) with an applied electric field, while the effective bandgap reduces from case (a) to (b) in the case without carrier depletion.

The absorption spectra due to the QCSE at a bias of 100 kV/cm has already been presented in Figure 3.7 while absorption spectra for doped QWs are presented in Figure 3.11. By comparing both figures, it can be seen that the electric field induced red shift is considerably enhanced due to the carrier depletion effect. In addition, we observe that the absorption strength for the doped QWs at an applied field of 100 kV/cm is now larger than at zero field. This behaviour is opposite to the undoped QW where the absorption strength decreases with applied field. It is very important to realize that the waveguide loss requirements as well as the requirement for a small electro-absorption loss do not allow realizing a similar red shift with a carrier-induced effect alone. A typical waveguide core of approximately 0.7 µm thickness contains fifty InGaAs/InAsP quantum wells in between 10 nm InP barriers. A doping level of $2.10^{11}/\text{cm}^2$ in each of these quantum wells, results in a total doping level of 1.10^{13}/cm^2 in the waveguide core or an average bulk doping level of $1.4.10^{17}$/cm^3 within the waveguide core. Such a doping level results in a free carrier loss of 0.4 dB/cm and also in an additional electro-absorption loss of 0.4 dB/cm in the phase shifter.

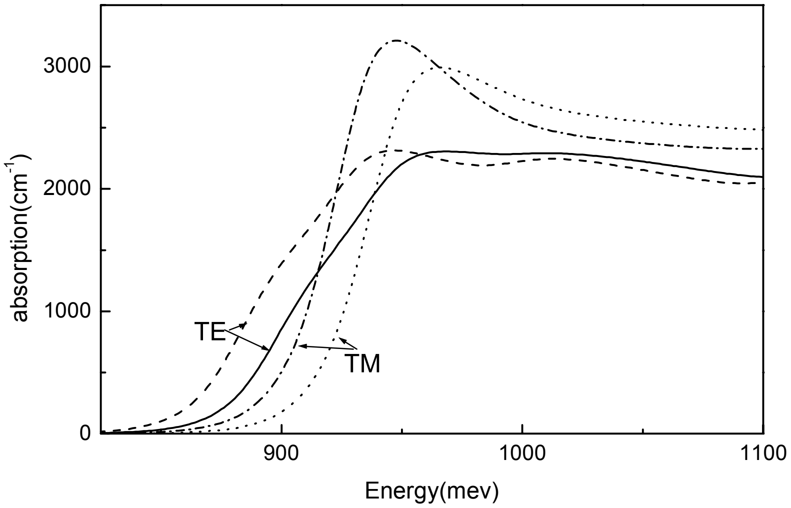

Figure 3.11: TE and TM absorption spectrum of 2.10^{11}cm^{-2} n-doped (2.5nm) $In_{0.38}Ga_{0.62}As$-(2nm) $InAs_{0.65}P_{0.35}$ QW and a field of 0 and 100kV/cm

We finally calculate the electro-refraction in doped $In_{0.38}Ga_{0.62}As$(2.5nm)/$InAs_{0.65}P_{0.35}$ (2 nm) quantum wells. We observe that the TE electro-refraction at 827 meV (1500 nm) increases from $0.76.10^{-3}$ for an undoped QW to $2.02.10^{-3}$ and $3.19.10^{-3}$ for doping levels of 2.10^{11}/cm^2 and 4.10^{11}/cm^2 respectively, as shown in Fig 3.12. We thus observe a 2.6 times increase in the TE electro-refraction by doping the InGaAs/InAsP quantum well with a carrier concentration of 2.10^{11}/cm^2. This again shows that both the Quantum Confined Stark Effect and the bandfilling effect are essential to reach large total electro-refraction. A further increase of the doping level inside the quantum wells would not only increase the waveguide loss and electro-absorption-induced crosstalk, but is enhances the electro-refraction only in a sublinear way as can be seen from the curve at 4.10^{11}/cm^2.

We finally calculate the length of the phase shifting section for a 2.10^{11}/cm^2-doped quantum well. Again also taking the Pockels effect into account, we find a phase shifter length of 0.92 mm for this quantum well. We note that this phase shifter length applies for a MZI, which is not used in push-pull configuration [10]. In the push-pull configuration, the length of the phase shifter can be decreased to 0.46 mm as will be shown in the next section.

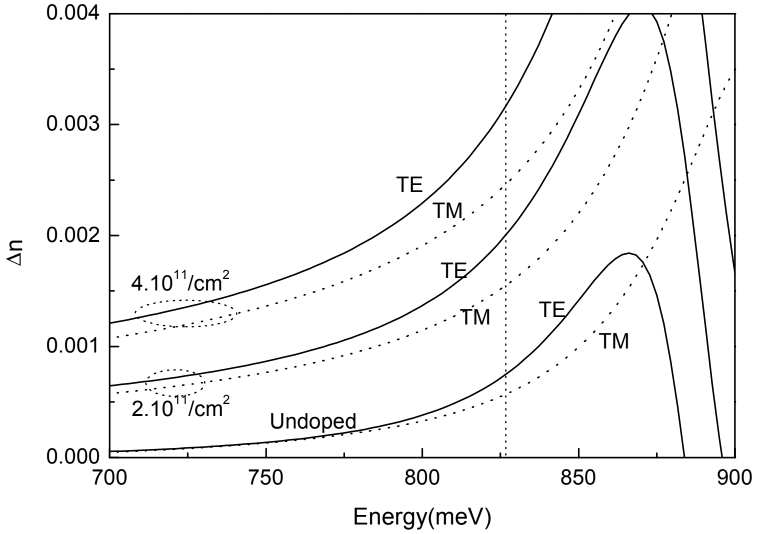

Figure 3.12: TE (solid curve) and TM (dotted curve) electro-refraction for undoped (2.5nm) $In_{0.38}Ga_{0.62}As$-(2nm) $InAs_{0.65}P_{0.35}$ QW at 100kV/cm. At an operating wavelength of 1500nm (827meV), The electro-refraction increases from $0.76.10^{-3}$ for an undoped QW to $2.02.10^{-3}$ and $3.19.10^{-3}$ for doping levels of $2.10^{11}cm^{-2}$ and $4.10^{11}cm^{-2}$, respectively

3.9 An asymmetric Mach-Zehnder interferometric space switch

An asymmetric MZI space switch as shown in figure 3.13 which can be operated in push-pull operation allows to further reduce the length of phase shifting region with more than a factor of two. The π/2 phase difference produced in the input multi-mode interference (MMI) coupler is balanced by an additional path length provided in the lower arm of the MZI. Hence with no bias voltage, the second MMI divides the output light equally over the two output arms of the MZI. In other words, the MZI acts like a 3 dB coupler. When a bias voltage is applied to one of the phase shifters, a π/4 phase shift will switch the light to the cross or bar output [20]. This reduces the length of the shifter by a factor of two to 0.46 mm. Moreover, in push-pull operation one can allow a 0.5 dB electro-absorption in both the push and the pull state at a phase shift of only π/4. This allows furthering reduction in the length of the phase shifter below 0.46 mm.

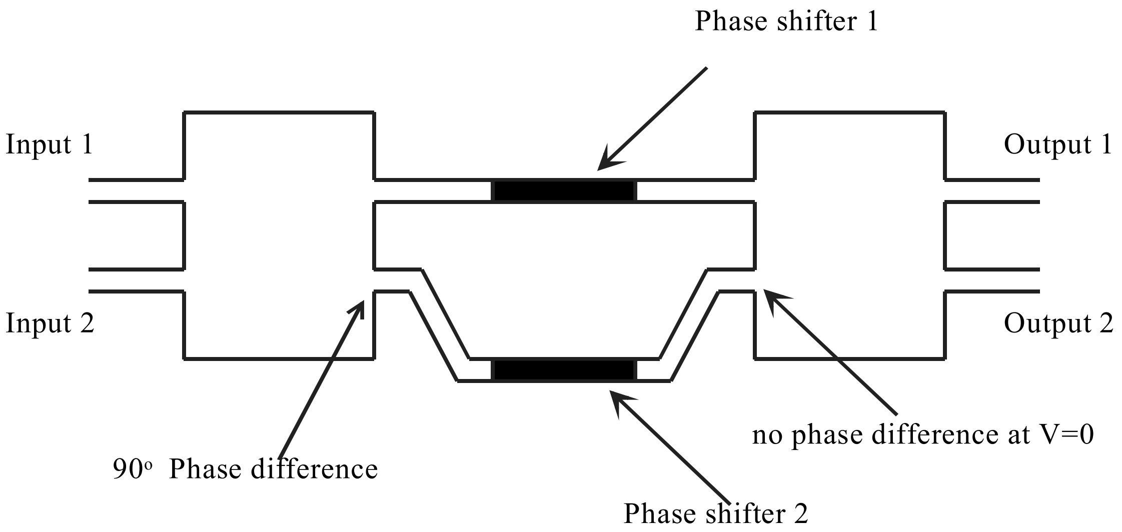

Fig 3.13: Layout of an asymmetric MZI switch allowing for push-pull operation.

3.10 Conclusions

In conclusion, we have investigated the electro-refraction in a doped InGaAs/InAsP quantum well within InP. We first optimised the magnitude of the electro-refraction due to the Quantum Confined Stark Effect (QCSE) alone, which resulted in a nearly polarization independent electro-refraction Δn of $7.8.10^{-4}$ for TE polarization at 100 kV/cm, combined with a waveguide loss of 0.2 dB/cm and an electro-absorption of only 0.1 dB/mm due to inter-band absorption.

In this quantum well material, carrier depletion effects can further enhance the electro-refraction while keeping the absorption induced waveguide loss below 0.6 dB/cm and the imbalance-induced crosstalk below 0.5 dB. We find that the carrier depletion of a n-doped quantum well at an applied bias, increases the TE electro-refraction with a factor 2.6 to 2.10^{-3}, resulting in a phase shifter length in an MZI of 0.92 mm for achieving a $\pi/2$ phase shift. The length of the phase shifter can be further reduced in push pull operation where one only needs a $\pi/4$ phase shifter, resulting in a phase shifter with a length of 0.46 mm. We finally conclude that for an n-doped quantum well, the electro-refraction due to the QCSE and carrier depletion together is a factor 2.8 larger than the Pockels effect for bulk material.

References

1. “Polarization-independent dilated InP based space switch with low crosstalk” D.H.P. Maat, Y. Zhu, F.H. Groen, H.van Brug, H.J. Frankena and X.J.M. Leijtens, IEEE Photon. Technol. Lett., vol.12, pp 284-286, 2000
2. “Tensile-strained multiple quantum-well structures for a large refractive index change by current injection” A. Kimura, M. Nido, A. Suzuki, IEEE.Photon. Technol. Lett, 6, pp 1101-1104, 1994
3. “A chopped quantum-well polarization-independent interferometric switch at 1.53 μm”, B.H.P. Dorren, A.Yu.Silov, D.M.H. Dukers, J.E.M. Haverkort, D.H.P. Maat, Y. Zhu, F.H. Groen and J.H. Wolter, IEEE J. Quantum. Electron., vol.36, pp 317-324, 2000
4. “Gain switching enhancement in asymmetric coupled quantum well”, S.J.Yoon, and I. Lee, Jpn. J. Appl. Phys., vol. 40, pp 3124-3130, 2001
5. “ Quantum Confined Stark Effect for differently shaped quantum wells”, W. Chen, T.G. Andersson, Semicond. Sci. Technol, vol. 7, pp 828-836, 1992
6. “Blue Stark shift in composite quantum wells” A.Yu.Silov, B.Aneeshkumar, M.R. Leys, B.Vonk, J.H.Wolter, in *Proc. 25th International Conference on the Physics of Semiconductors, part I,* pp.517-518, 2000
7. “Strain-balanced InAsP/InP/InGaAs multiple quantum well structures for mid- infrared photodetectors”, M.Wada, S.Araki, T.Kudou, T.Umezawa, S.Nakajima, and T.Ueda, Electron. Lett., vol. 38, pp 1744-1745, 2002
8. “Gain switching enhancement in asymmetric coupled quantum well”, S.J.Yoon, and I. Lee, Jpn. J. Appl. Phys., vol. 40, pp 3124-3130, 2001
9. “The theory of strained layer quantum-well laser with band gap renormalization”, IEEE J. Quantum. Electron., vol. 30, pp 350-365, 1994
10. “Polarization-independent switching operation in directional coupler using tensile- strained multi-quantum well”, T.Aizawa, Y.Nagasawa, K.G.Ravikumar, and T.Watanabe, IEEE.Photon. Technol. Lett., vol. 7, pp 47-49,1995
11. “Dependence of polarization, gain, line width enhancement factor, and K factor on the strain of InGaAs/InP strained-layer multiquantum well lasers”, L.F.Tiemeijer, P.J.A.Thijs, P.J.de Waard, J.J.M.Binsma, and T.v.Dongen, Appl. Phys. Lett., vol. 58, pp 2738-2740, 1991

12. "Polarization-independent quantum-confined stark effect in an InGaAs/InP tensile-strained quantum well", T.Aizawa, K.G.Ravikumar, S.Suzaki, T.Watanabe, and R.Yamauchi, IEEE J. Quantum. Electron., vol. 30, pp 585-592, 1994
13. "Polarization-independent quantum-confined stark effect in an InGaAs/InP tensile-strained quantum well", T.Aizawa, K.G.Ravikumar, S.Suzaki, T.Watanabe, and R.Yamauchi, IEEE J. Quantum. Electron., vol. 30, pp 585-592, 1994
14. "Photocurrent and photo luminescence spectroscopy of $InAs_xP_{1-x}$/InP strained quantum wells grown by chemical beam epitaxy", C.Monier, M.F.Vilela, I.Serdiukova, A.Freundlich, J. Cryst. Growth., vol. 188, pp 332-337, 1998
15. "Band discontinuity in strained In(As,P)/InP heterostructures", C. Monier, M.F. Vilela, I. Serdiukova, A. Freundlich, Appl. Phys. Lett., Vol. 72, pp 1587-1589, 1998
16. "Growth of InAs/InP and InAsP/InP heterostructures by chemical beam epitaxy", A.Freundlich, A.H.Bensaoula, and A.Bensaoula, J. Cryst. Growth, vol. 127, pp 246-250, 1993
17. "Strong blue shift of the excitonic transition in the InGaAs/InP/InAsP antisymmetric coupled quantum wells", Y.Huang, Y.Chen, C.Lien, Appl. Phys. Lett., vol. 67, pp 2603-2605
18. "Low loss InGaAs/InPmultiple quantum well waveguides", U.Koren, B.I.Miller, T.L.Koch, G.D.Boyd, R.J.Capik, and C.E.Soccolich, Appl. Phys. Lett., vol. 49, pp 1602-1604, 1986
19. "Electric-field dependence of linear optical properties in quantum well structure: Waveguide electroabsorption and sum rules", D.A.B. Miller, J.S. Weiner, D.S. Chemla, IEEE. J. Quantum. Electron., vol. 22, pp 1816-1830, 1986
20. " Low-crosstalk penalty MZI space switch with a 0.64-mm phase shifter using quantum-well electrorefraction", B.H.P. Dorren, J.E.M. Haverkort, R. Prasanth, F.H. Groen, J.H. Wolter, IEEE Photon. Technol. Lett., vol. 13, pp 37-39, 2001

Chapter 4

Electro-refraction in quantum dots

"...for without the making of theories I am convinced there would be no observations"
Charles Darwin

4.1 Introduction

In chapter 3 we showed that reducing the dimensionality of the semiconductor structure from bulk towards a quantum well, provided improved performance phase shifters. We presented a quantum well structure, which decreases the length of the phase shifting section down to 0.46 mm, by combining carrier depletion and the QCSE.

In this chapter, we theoretically analyze the possibility of using quantum dots for providing electro-refraction in the phase shifter of an MZI. The conceptual advantage of QDs is the discrete density of states, resulting in narrow absorption peaks with high exciton oscillator strength. These narrow peaks shift with an applied electric field due to the QCSE. When choosing the operating wavelength to coincide with the peak of such a discrete absorption peak, both the QCSE and bandfilling result in a quickly decreasing absorption strength. On resonance, we thus expect a large electro-absorption. On the other hand, when the operating wavelength is selected just outside the discrete absorption peak, a clear electro-refraction effect is expected. Measurements of the electro-optic coefficients in quantum dots have suggested large electro-optic coefficients [1, 2]. Aizawa [3] has measured a 35 times larger refractive index variation in an etched quantum box as compared to a quantum well. In particular we investigate the influence of the geometry of the QD as well as of the QD-size on the QCSE and the exciton oscillator strength [4, 5]. The geometry and size dependence is studied for optimizing the electro-refraction using a numerical model based on the 4x4 Luttinger-Kohn Hamiltonian, as presented in Chapter 2.

4.2 QCSE in quantum dots

Using the numerical model explained in Chapter 2, we first compare the magnitude of the Quantum Confined Stark Effect (QCSE) in InAs/GaAs and InAs/InP quantum dots. Due to the high lattice mismatch between InAs and GaAs, the strain in the InAs/GaAs system is 6.8%, whereas the lattice mismatch in the InAs/InP system is only 3.2%. The strain will strongly modify the confinement potential. In our calculations, we assume two third of the strain-induced shift in the conduction band state as explained in ref [6]. The effective confinement energies in the strained system are tabulated in Table. I. For comparing the results with other experimental and theoretical investigations, we calculated the QCSE at low temperature. Figure 4.1 shows the Stark shifts of the heavy hole and light hole transitions in InAs/GaAs and InAs/InP cylindrical quantum dots at low temperature.

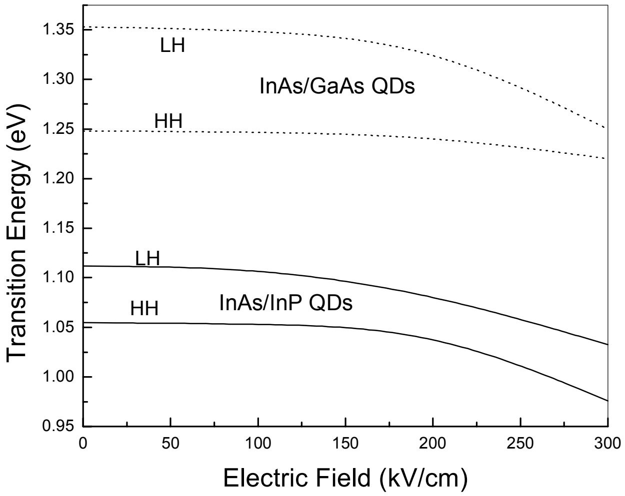

Figure 4.1: QCSE in cylindrical InAs/GaAs (dotted) and InAs/InP (solid) quantum dots with a radius of 5 nm and a height of 3 nm.

	E_g (eV)	V_e (eV)	V_{hh} (eV)	V_{lh} (eV)
InAs/InP	0.562	0.547	0.292	0.176
InAs/GaAs	0.72055	0.492	0.3367	0.086

Table I: Effective confinement energies (band offset parameters) for InAs QDs at room temperature

The light hole resonance is close to the bulk GaAs valence band, resulting in a larger QCSE as compared to the heavy hole resonance in InAs/GaAs QDs. For the InAs/InP quantum dots, both the heavy hole and light hole states leak more easily into the barrier with an applied field, due to the lower confinement as a result of the smaller strain, thus showing a larger Stark shift. We checked our calculations and computer codes with the experiments of Fry et.al [7] below 200 kV/cm as well as with the calculation of Su-Shen Li [6], both showing good agreement.

4.3 Geometrical dependence of the QCSE

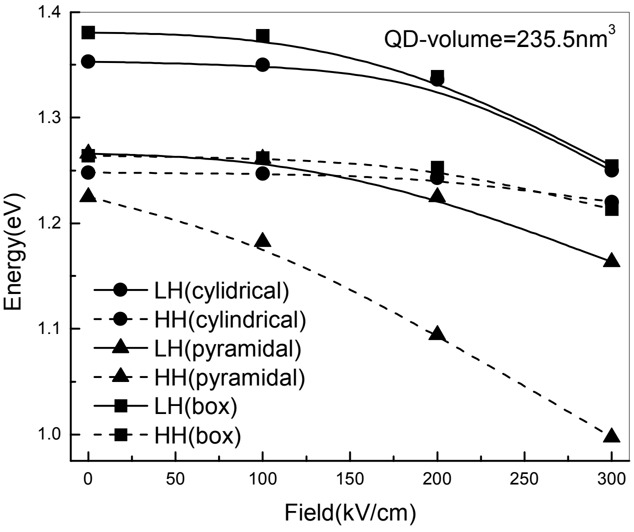

Figure 4.2: Quantum Confined Stark Effect in InAs/GaAs quantum dots at low temperature, for box, cylindrical and pyramidal geometries with the same QD-volume of 235 nm^3.

For optimizing the Quantum Confined Stark Effect, we consider quantum dots with different geometries, a cylinder with r= 5 nm, a cone-shaped pyramid with r =10 nm base and a box with a 8.9x8.9 nm base, all with 3 nm height and equal QD volume. In order to keep the effect of the surrounding matrix constant in all calculations, we employ the same barrier height for all geometries. For converging the eigenstates and eigenvalues we consider 343 plane wave states with n, l, m values –3…0…3. In the pyramidal structure, the QCSE for the heavy holes is five times larger than for the other geometries. Also in the pyramidal geometry, the heavy hole states, which are located more towards the base of the pyramid, will experience a larger QCSE as compared to the light hole states, which are confined near the top of the cone. Figure 4.2 shows the QCSE of InAs/GaAs quantum dots for different geometries, where the transition energies have been calculated at low temperature. Since the application of a high electric field will eventually create a second potential minimum in the barrier region, we will restrict our electro-refraction calculations to ≤100 kV/cm. With such a restriction, the sum rule for conservation of absorption strength with field [4] will also be conserved. Since all devices are operating at room temperature, we calculated the electro-absorption and electro-refraction at room temperature.

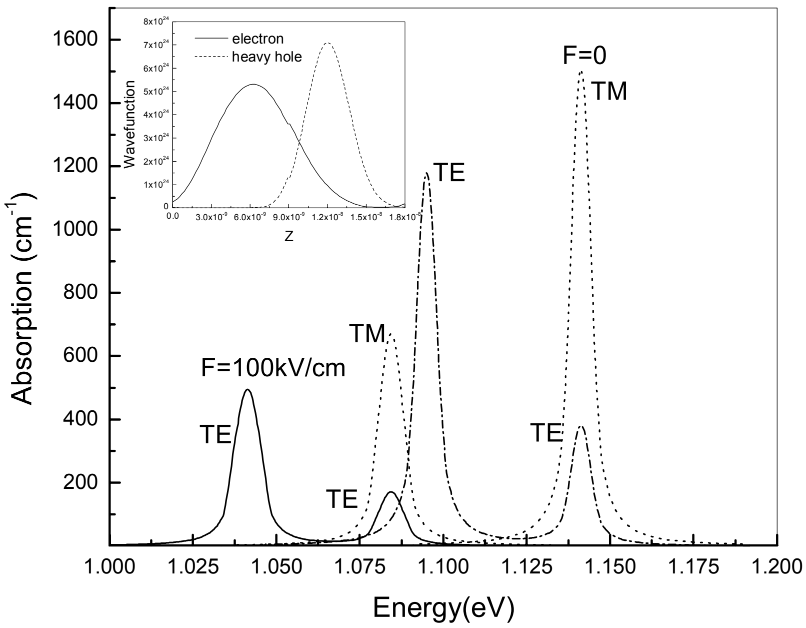

Figure 4.3: TE and TM absorption spectra of a pyramidal quantum dot with a radius of 8.7 nm and a height of 6 nm at room temperature. A cut along the z-axis of the electron (dotted) and heavy hole (solid) wavefunctions at 100 kV/cm is plotted in the inset

The heavy hole and light hole excitonic absorption spectra with and without applied electric field are shown in figure 4.3 for a pyramidal quantum dot at room temperature. The electron and heavy hole wave functions at an applied electric field of 100 kV/cm are shown in inset. In order to obtain the correct spectrum, we substantially broadened the delta like absorption with a Gaussian function. Using the room temperature dephasing time of 260 fs as measured by Borri et.al. [8] for InAs/GaAs quantum dots, we employ a FWHM of 10 meV at room temperature. Further away from the transition, we include an Urbach tail in order to be able to properly calculate the waveguide absorption loss. At electric fields below 100 kV/cm, the oscillator strength will change only marginally since the confinement potential is much larger than the electric field induced changes to that potential. However, when the shift of the excitonic absorption spectrum is larger than its FWHM, such a red shift will still produce large electro-refraction.

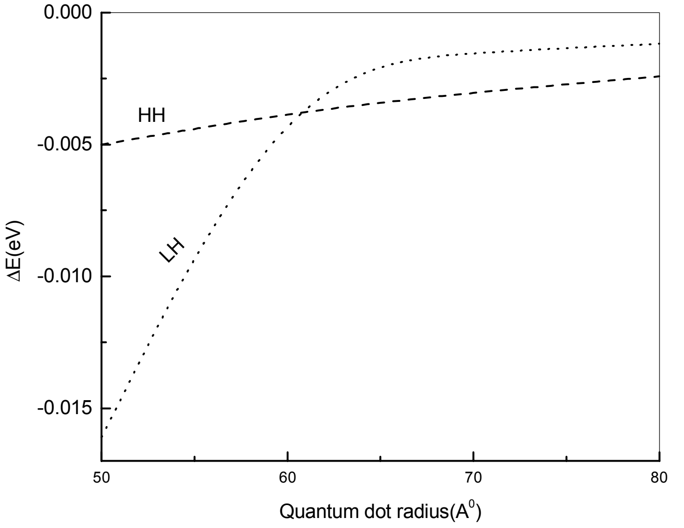

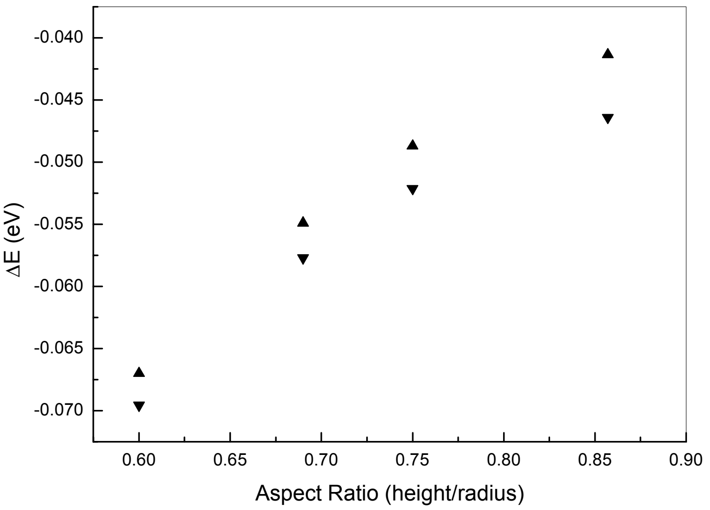

Figure 4.4: (Top) Calculated QCSE Stark shifts for an applied field of 200 kV/cm as a function of the QD radius for cylindrical QDs with a height of 3nm. (Bottom) Calculated QCSE for heavy-holes (▲) and light-holes(▼) at an applied field of 100 kV/cm as a function of the aspect ratio for pyramidal QDs with a height of 6 nm.

For optimizing the Stark shift, we observe that the Stark shift sharply increases with increasing height of the QD. Moreover, the Stark shift increases for small aspect ratio as shown in the bottom panel of figure 4.4. We also find that the Stark shift is optimized for small radius in the cylindrical QDs, which is in particular true for the light hole level as shown in the top panel of figure 4.4.

The QCSE increases for small QD radius since the envelope function will leak more strongly into the barrier layers, thus increasing the Stark shift. This suggests that one should employ the light-hole resonance for switching applications. The electro-refraction spectrum using the Kramers-Kronig relations is presented in figure 4.5. Since we have calculated the envelope wavefunctions in a box of 20x20x8 nm^3, the calculated electro-refraction corresponds to a QD-density of $2.5x10^{11}/cm^2$ or $3.12x10^{17}/cm^3$. We observe a very large peak electro-refraction of 0.35 for TE-polarization and 0.43 for TM-polarization. For comparison, the quantum well structure explained in chapter 3 shows a peak $\Delta n < 0.005$ due to the QCSE at 100 kV/cm and $\Delta n < 0.01$ when combining the QCSE with the carrier depletion effect at a carrier density of $4x10^{11}/cm^2$. The very large peak electro-refraction in quantum dots clearly proves that properly designed quantum dots

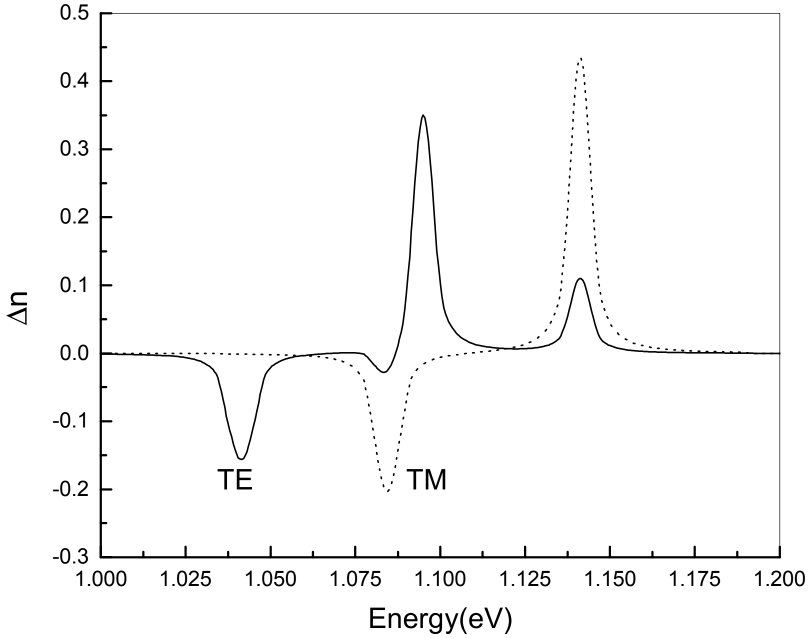

Figure 4.5 Electro-refraction at 100 kV/cm in an InAs/GaAs a pyramidal quantum dot with a radius of 8.7 nm and a height of 6 nm at room temperature.

allow to enhance the electro-refraction >35 times compared to quantum well material. This enhancement in QDs as compared to QWs happens to coincide with the reported enhancement of the electro-refraction by Aizawa [3].

It should be noted that in a waveguide device or in a Mach-Zehnder switch, one employs the electro-refraction in the transparent part of the absorption spectrum below the heavy hole resonance. We assume a high optical confinement factor of 0.1, which assumes that 10% of the waveguide mode volume is filled with a high-density QD-array of $3.1.10^{17}/cm^3$.

Using the data presented in figure 4.3 on a logarithmic scale and using an Urbach parameter of 8 meV, the waveguide absorption loss without electric field decreases to 0.15 dB/cm at 1.030eV. Figure 4.6 shows the calculated electro-refraction spectrum on an expanded scale. We now observe a large electro-refraction of $\Delta n=1.3.10^{-2}$ at 1.030eV where the absorption loss is limited to 0.15 dB/cm. For comparison, in quantum well case for a similar absorption loss of 0.2 dB/cm we calculated a quantum well electro-refraction due to the QCSE of 8.10^{-4} [2, Chapter 3 of this Thesis] at 0.827 meV. However, in the case of quantum dots, the waveguide absorption loss at 1.030 eV increases to 42/cm in the presence of an applied electric field of 100 kV/cm, which is a major drawback in this case.

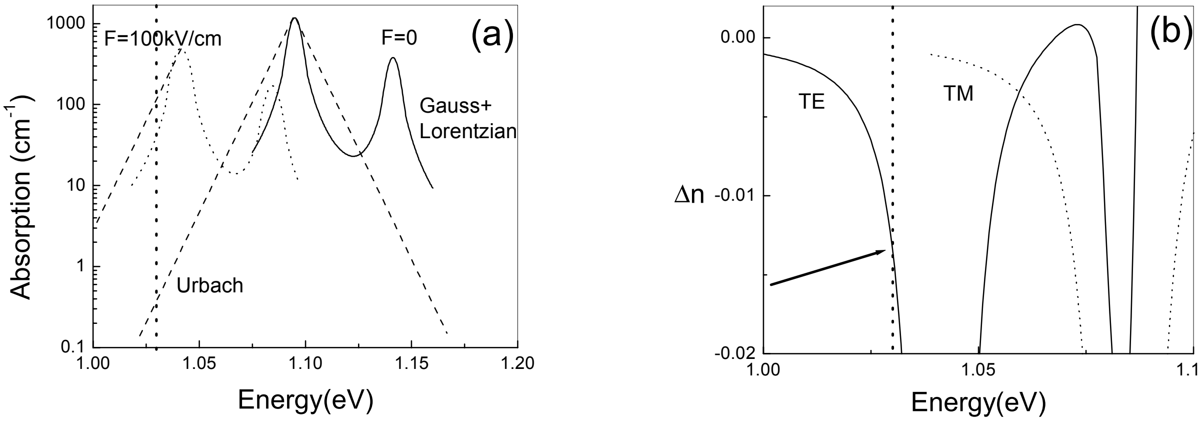

Figure 4.6: (a) The QD absorption spectra without field (solid) and at an applied electric field of 100 kV/cm (dotted) plotted on a logarithmic scale. The operating wavelength is chosen at 1.03 eV where the absorption loss is 0.15 dB. (b) The electro-refraction spectrum of Fig 4.5 plotted at an expanded scale, showing the residual electro-refraction at 1.03 eV for TE (solid) and TM-polarization (dotted).

Conclusions

In conclusion, we have calculated the electro-refraction in quantum dot materials with different geometrical shapes. We found that the shift due to QCSE is considerably larger in pyramidal QDs as compared to square or cylindrical QDs. Moreover, we found that the QCSE is optimized for large heights and small radius. We calculated both the electro-absorption and electro-refraction spectra for TE and TM-polarization. We found very high peak values for the electro-refraction of 0.35 for TE and 0.43 for TM-polarization, which is considerably larger than for the quantum well case [2,.Chapter 3 of this Thesis]. For application in a waveguide, the electro-absorption in the tail of the QD absorption spectrum is most relevant. At 1.030 eV, where the waveguide absorption loss reaches an acceptable value of 0.15 dB/cm, we found $\Delta n=1.3.10^{-2}$ at a QD-density of $2.5.10^{11}/cm^2$ with an 8 nm layer separation.

References

[1] "Nonlinear optical and electro-optical properties of InAs/GaAs self-organized quantum dots", S.Ghosh, A.S. Lenihan, M.V.G. Dutt, O. Qasaimeh, D.G. Steel, P. Battacharya, J.Vac.Sci.Technol.B., vol. 19, pp 1455-1458, 2001

[2] "Linear and quadratic electro-optic coefficients of self organized InGaAs/GaAs quantum dots", O.Qasaimeh, K. Kamath, P. Bhattacharya, J. Philips, Appl.Phys.Lett., vol. 72, pp 1275-1277, 1998

[3] "Observation of field-induced refractive index variation in quantum bos structure", T. Aizawa, K. Shinomura, A. Arai, Y. Suematsu, IEEE Photon.Technol. Lett., vol 3, pp 907-909, 1991

[4] "Electroabsorption of highly confined systems: Theory of Quantum-confined Franz-Keldish effect in Semiconductor Quantum Wires and Dots", D.A.B. Miller, D.S. Chemla, S. Schmitt-Rink, Appl.Phys.Lett vol52, no.25, pp 2154-2156, 1988

[5] "Electrorefraction in Quantum Dots" R. Prasanth, J.E.M. Haverkort, J.H. Wolter, IEEE/LEOS, Benelux Chapter, pp 234-237, Dec, 2002

[6] "Effective-mass Theory for InAs/GaAs Strained Coupled Quantum Dots" Shu-Shen Li, Jian-Bai Xia, Z.L.Yuan, Z.Y. Xu, Wekun Ge, Xiang Rong Wang, Y. Wang, J. Wang, L.L. Chang, Phys.Rev.B, vol 54, no:16, pp 11575-11581, 1996

[8] "Inverted Electron-hole alignment in InAs-GaAs Self-Assembled Quantum dot", P.W. Fry, I.E. Itskevich, D.J. Mowbray, M.S. Skolnick, J.J. Finley, J.A. Barker, E.P. O'Reilly, L.R. Wilson, I.A. Larkin, P.A. Maksym, M. Hopkinson, M. Al-Khafaji, J.P.R. David, A.G. Cullis, G. Hill, J.C. Clark, Phys. Rev. Lett. Vol. 84, pp. 733-736, 2000

[9] "Dephasing in InAs/GaAs quantum dots", P. Borri, W. Langbein, J. Mork, J.M. Hvam, F. Heinrichsdorff, M.-H. Mao and D. Bimberg, Phys.Rev.B Vol 60, pp. 7784-7787, 1999

Chapter 5

All optical switching in quantum dots

"An experiment is a question which science poses to Nature,
And a measurement is the recording of Nature's answer"
Max Plank

5.1 Introduction

Many interesting proposals have been suggested by researchers to exploit all-optical nonlinearities for ultra fast signal processing [1]. Multiple quantum wells gathered much attention in all optical signal processing because of their remarkably large optical non-linearity due to bleaching of the excitonic absorption [2]. The prospective of quantum dots for ultra-fast all-optical signal processing has yet to be demonstrated [3,4]. The large optical non-linearity, which is expected from the delta like density of states, strongly positions quantum dot material as a promising material for device applications.

All optical switching has mainly been performed using active elements such as semiconductor optical amplifier gates [2, 5,6]. Photonic switching in passive materials [1,4] usually suffered from too small all-optical nonlinearities, which required a too high switching energy. Semiconductor QDs are expected to provide improved all-optical nonlinearities. The delta-function like density of states in quantum dots results in sharp excitonic absorption peaks with considerably larger peak absorption than in a bulk or quantum well structures. Moreover, when the QD is filled with a single electron-hole pair, the ground state becomes transparent, while two electron-hole pairs within a single QD already generate optical gain. This behaviour is expected to result in an extremely small switching energy in quantum dots. This chapter explains the switching in the 1550 nm wavelength window due to a single layer of InAs/InP QDs embedded in an InGaAs/InP waveguide structure, which have been processed into a Mach-Zehnder Interferometric (MZI) switch.

5.2 Chemical beam epitaxial growth of quantum dots

A monolayer (ML) by monolayer growth technique is required to grow quantum dots with a sufficiently high material quality. In Chemical Beam Epitaxy (CBE), the In, Ga, As, and P constituents are transported to the growth chamber in gaseous form, i.e. TMIn, TEGa, Arsine and Phosphine [figure 5.1]. These gases are subsequently evaporated in effusion cells and directed towards the substrate, which is located in the CBE chamber under ultrahigh vacuum conditions. These pre-cursor materials are either cracked in the oven or are thermally decomposed near the substrate, which is kept at a high growth temperature (~500^0C). In principle the growth can be performed on a substrate cut along any crystallographic direction. A suitable Growth Interruption (GI) sequence will minimise the interface layer thickness by allowing some time for surface diffusion.

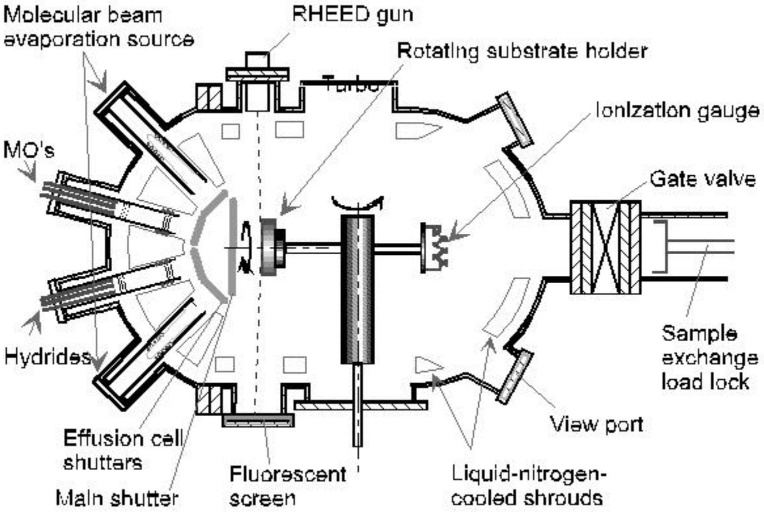

Figure 5.1: Schematic diagram of the CBE chamber

In the Stranski-Krastanov growth process, self-assembled quantum dots can be formed due to a strain relaxation of a highly lattice mismatched epitaxial InAs layer. For growing InAs quantum dots in between an InP barrier, a few monolayers of InAs are grown on top of an InP substrate. When the InAs layer thickness exceeds the critical layer thickness, strain relaxation will lead to island formation or quantum dot formation. Subsequently, the quantum dots are optically characterized by photoluminescence measurement while their structural quality is judged by AFM measurements together, these characterization techniques will provide information about the size, the geometry and the composition of the InAs/InP quantum dots.

In our experiments, we use a QD structure (Fig. 5.2), which was grown on a (100) oriented InP substrate. For the growth of InAs/InP quantum dots AsH_3, PH_3, and TMI precursors have been used. The AsH_3, and PH_3 are cracked at 900^0C to get As and P. For the structure investigated in this Chapter, a lattice matched quaternary layer of $Ga_xIn_{1-x}As_yP_{1-y}$ (x= 0.2515, y= 0.546) with a thickness of 185 nm is deposited on a (100) oriented InP substrate. After the growth of the lower quaternary layer, a 2 sec GI is provided. Then 4.3 ML of InAs is grown on top of the quaternary layer, by a controlled flow of TMI and AsH_3. After that, a 10 sec GI is applied under AsH_3 conditions. Subsequently, 5 ML's (0.62 nm) of InP are grown to cap the dots and to shift the PL down from 1600 nm to 1500 nm. After that, a 5-minute GI is provided under PH_3 condition. Then the upper quaternary layer with a thickness of 185 nm was deposited on top of the quantum dot layer. Finally, a 1.3 μm InP layer is grown on the top, which will act as the cladding layer of the waveguide. A quantum dot density of $\sim 1.4.10^{10}/cm^2$ has been estimated in the guiding layer from the AFM picture of similar uncapped QDs shown in figure 5.2.

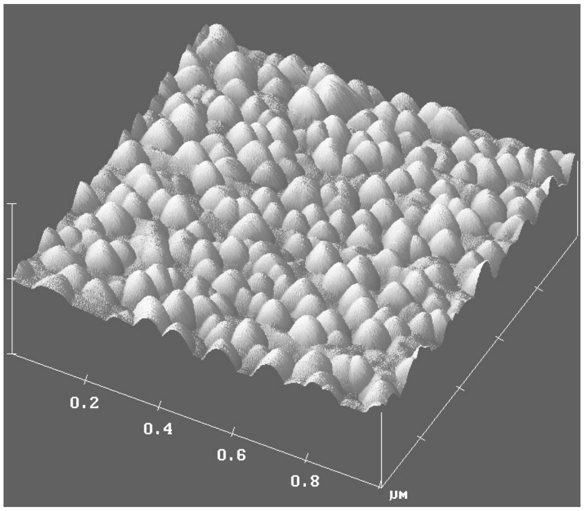

Figure 5. 2: AFM Picture of InAs Quantum dot

5.3 Mach-Zehnder interferometric space switch.

The waveguide structure consists of a 370 nm thick Q1.3 InGaAsP layer, which together with the single quantum dot layer, forms the waveguide core. The 1.3 μm InP layer on the top will act as the cladding layer. The sample structure before and after etching is shown in figure 5.3 (a) and (b) respectively. A 2x2 Mach-Zehnder Interferometeric (MZI) switch [7,8] was then developed on this CBE grown quantum dot sample. The MZI based switch consisted of a Multi Mode Interference

(MMI) [9] type 3 dB splitter and a 3 dB combiner connected by two interferometer arms. The structure was defined in 100 nm SiN_x using contact photolithography on positive photoresist. The SiN_x-mask layer was etched employing CHF_3 reactive ion etching (RIE) process. The ridge waveguides were etched using a CH_4/H_2 RIE process and an O_2 descumming process. The input Multi-Mode Interference coupler divides the incoming light equally into the two parallel waveguide arms of the switch, with a length of 605 µm. By tuning the effective refractive index of one of the arms, the phase difference at the 3 dB combiner can be changed such that light switches from one output port to the other. Typical dimensions for the waveguide are a width of 2.8 µm for the lower arm and a width varying between 3.5 to 3.7 µm for the upper arm. The separation between the two arms of the switch was 30 µm. The waveguide was 30 nm shallow etched into the upper quaternary layer of the sample. This shallow etching helped to reduce the waveguide attenuation loss [10].

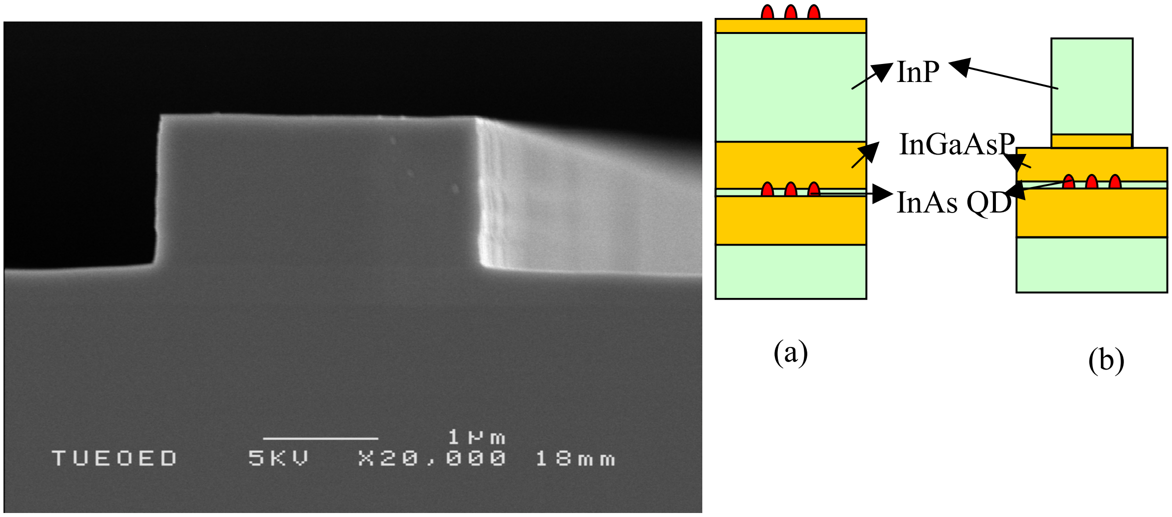

(a)

(b)

Figure 5.3: SEM picture of the wave-guide structure. The schematic diagram shows the CBE grown waveguide structure (a) before etching (b) after etching

The experimental setup for all-optical switching is represented in figure 5.4. The output from a solid-state frequency-doubled Nd:YAG laser is used to pump a femtosecond mode-locked Ti-Sapphire laser, which in turn was used to pump the tunable femtosecond optical parametric oscillator

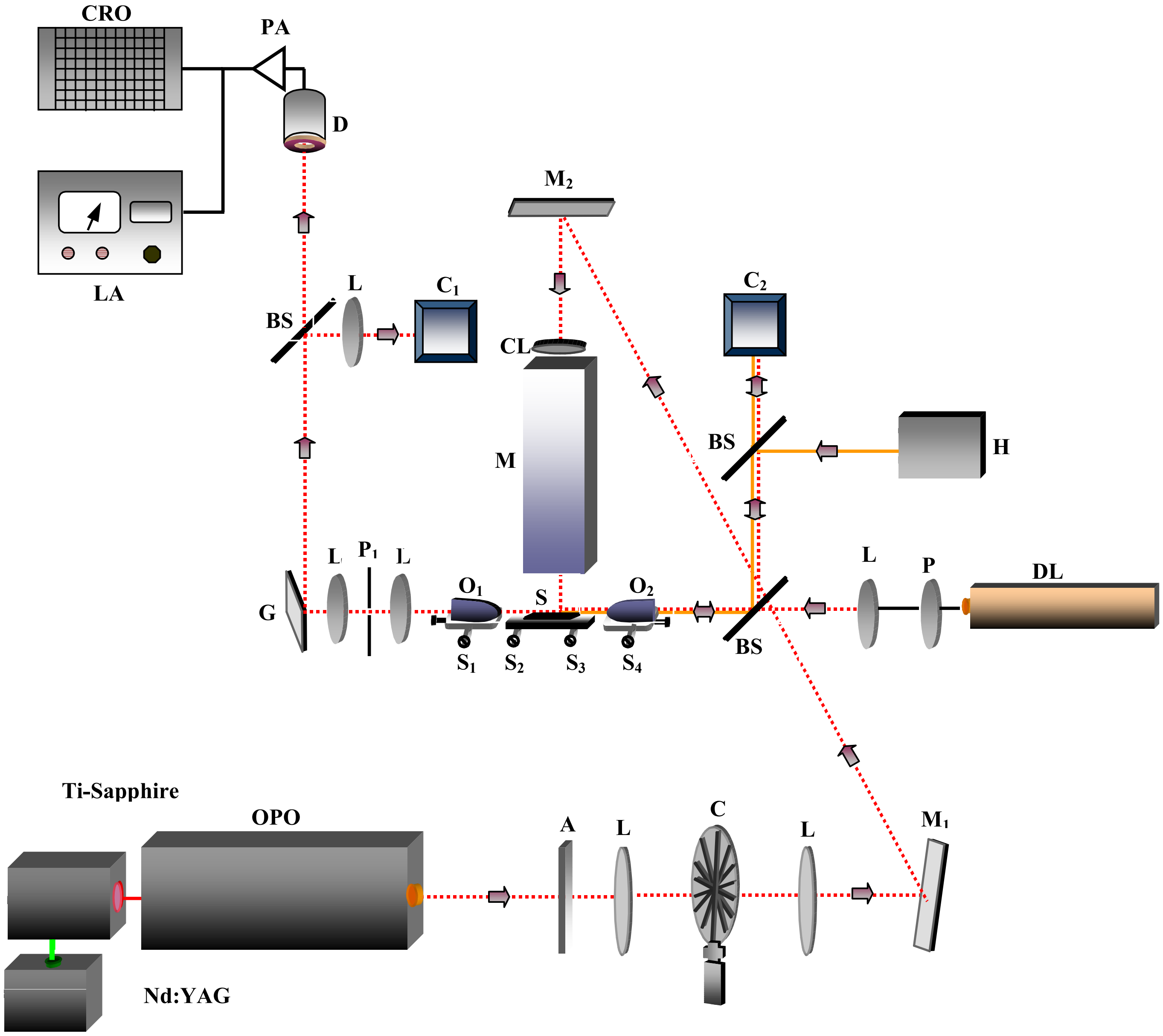

Figure 5.4: The experimental setup for all-optical switching in a Mach-Zehnder space switch

OPO	**: Optical Parametric Oscillator**	**H**	**: Halogen Lamp**
L	**: Achromatic Lens**	**M**	**: Optical Microscope**
C	**: Chopper**	**BS**	**: Beam Splitter**
$M_{1,2}$	**: Silver Mirrors**	**$C_{1,2}$**	**: CCD Camera**
DL	**: Tunable Diode Laser**	**LA**	**: Lock-in Amplifier**
$O_{1,2}$	**: Objectives**	**D**	**: Photodiode**
S	**: Quantum Dot Sample**	**G**	**: Grating**
$S_{1,2,3,4}$	**: Electrostrictive Screws**	**P**	**: Polarizer**
P_1	**: Micrometer Slit**	**CL**	**: Cylindrical Lens**
A	**: Attenuator**	**PA**	**: Pre-amplifier**

(OPO) using a CTA crystal. The output of the OPO with a maximum power of 280 mW served as the pump beam in this experiment. The power level was attenuated using a variable attenuator and chopped at about 2000 Hz. The pump power on the sample was measured using a power meter. This pump beam was deflected by silver mirrors and focusing lenses to the microscope output of an Olympus Zoom Stereo Microscope. The microscope was used to position and focus the pump beam on one of the arms of the MZI. We used a cylinder lens to change the focus on the sample into a stripe of 600x25 μm^2. A CW tunable diode laser with polarization maintaining output up to a maximum of 2 mW is used as the probe laser. A Glan-Thomson prism was used to select the polarisation of the probe beam. A halogen lamp helped to illuminate the input facet of the sample and thereby helped to observe the input coupling of the probe beam onto the input facet of the waveguides with an IR Camera. A microscope objective lens with a 20X magnification provided the coupling of the probe beam into the required waveguide of the MZI switch. At the output side of the sample, a similar microscope objective served to focus the beam spot onto a 100 μm slit using a 50 mm lens. This slit helped to select the output from one of the two arms of the MZI switch. A grating (300 lines/mm) was inserted to remove the photoluminescence signal arising from the quantum dots in the core of the waveguide. The transmitted probe signal is detected using an InGaAs detector. After pre-amplification, the probe signal is monitored on an oscilloscope (CRO) and the modulated part of the probe signal is measured with a Lock in Amplifier. For alignment purposes, an IR camera was employed to monitor output pattern at the output facet of the sample.

5.4 All-optical switching in a MZI

The Mach-Zehnder space switch is very sensitive to refractive index variations and is able to produce fast and polarization insensitive switching. Like in any other waveguiding device, the propagation loss due to material absorption, dispersion and the waveguide scattering losses are a parasitic effect. Imbalance between the two arms of the MZI switch due to these parasitic effects will lead to cross talk. Differences in the material absorption loss between the two arms of the MZI, due to bleaching of the quantum dot transition is the most significant factor causing imbalance. Usually in InAs quantum dot material, the excitonic peak absorption is 2000 cm^{-1}. So for device applications a proper detuning to the Urbach tail of the absorption peak is required. This detuning will exponentially reduce the absorption loss inside the waveguide by

$$\alpha = \alpha_0 e^{-\left(\frac{\hbar\omega - E_g}{E_0}\right)} \tag{5.1}$$

where $\hbar\omega - E_g$ is the detuning energy from the band edge and E_0 is the Urbach parameter which is 8 meV for GaAs.

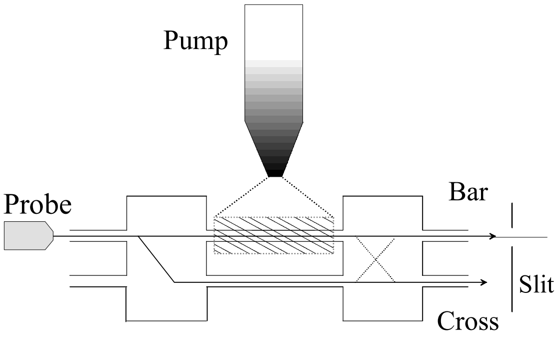

Figure 5.5: Schematic diagram of the quantum dot MZI switch, which is used for all optical switching.

The scattering losses are mainly sensitive to the sidewall roughness of the waveguides. These losses can be minimised by proper etching of the waveguides. We used a shallow etched waveguide in which the waveguide attenuation is much less than in deeply etched ones for single mode operation. For switching the signal from one output to the other, a π/2 phase shift is required between the two arms of the MZI. So the optical path difference for a complete switching is $\lambda_{vac}/2$. Hence the required length of the phase-shifting region, for an optical mode with confinement factor Γ is

$$l = \frac{\lambda_{vac}}{2\Delta n \Gamma} \tag{5.2}$$

The confinement factor depends upon the overlap between the active quantum dot material and the waveguide optical mode. In our structure, the quantum dot height is approximated to be 7 nm and the width of the optical mode is approximately 370 nm, yielding a confinement factor of 2.7%. A stack of multiple layers of quantum dots will improve the coupling between the optical mode and the quantum dots.

5.4.1 Switching principle of a MZI switch

If two signals of equal intensity are mixed in a 2x2 coupler, like at the output of the MZI [11,12], the amplitude of the output signal in arm 1 is

$$E_1 = \left(\tfrac{1}{2} i + \tfrac{1}{2} e^{i\Delta\varphi} \right) \tag{5.3}$$

where the two terms represent contributions from each of the two branches (the "i" in the first term represents the 90 degrees phase shift of the MMI coupler, $\Delta\varphi$ is the phase shift between the two signals). The power is then given by

$$P_1 = \tfrac{1}{2} - \tfrac{1}{2} \sin(\Delta\varphi) \tag{5.4}$$

The amplitude of the signal in the second arm reads

$$E_2 = \left(\tfrac{1}{2} + \tfrac{1}{2} i e^{i\Delta\varphi} \right) \tag{5.5}$$

and the power is given by:

$$P_2 = \tfrac{1}{2} + \tfrac{1}{2} \sin(\Delta\varphi) \tag{5.6}$$

Now if the two signals are unequal, the same analysis can be done, and the result for the amplitude E_1 in the first arm is

$$E_1 = \left(\tfrac{1}{2} iA + \tfrac{1}{2} e^{i\Delta\varphi} \right) \tag{5.7}$$

Where "A" is the amplitude ratio between both branches. The power is then:

$$P_1 = \tfrac{1}{4} A^2 + \tfrac{1}{4} - \tfrac{1}{2} A \sin(\Delta\varphi) \tag{5.8}$$

The power leaving the second arm is

$$P_2 = \tfrac{1}{4} A^2 + \tfrac{1}{4} + \tfrac{1}{2} A \sin(\Delta\varphi) \tag{5.9}$$

Let us now assume originally equal signals (so Eqs [5.4] and [5.6] hold), but with an external small modulation, which changes both the amplitude due to bleaching and the phase due to refraction index nonlinearity. Then we have to use Eqs.[5.8] and [5.9] with a small amplitude difference due to bleaching of the quantum dot absorption $A \rightarrow 1 + \partial A$ and phase difference $\Delta\varphi \rightarrow \Delta\varphi + \partial\varphi$ due to the all-optical nonlinearity, where ∂A and $\partial\varphi$ are considered as a small correction to the equal signal case. Inserting this in Eqs, [5.8] and [5.9], and performing some differential calculus and keeping only the linear terms gives us:

$$P_1 = \tfrac{1}{2} - \tfrac{1}{2}\cos(\Delta\varphi)\partial\varphi + \partial A\left(\tfrac{1}{2} - \tfrac{1}{2}\sin(\Delta\varphi)\right) \qquad (5.10)$$

and

$$P_2 = \tfrac{1}{2} + \tfrac{1}{2}\cos(\Delta\varphi)\partial\varphi + \partial A\left(\tfrac{1}{2} + \tfrac{1}{2}\sin(\Delta\varphi)\right) \qquad (5.11)$$

showing that an all-optical nonlinearity $\partial\varphi$ provides an asymmetric contribution which is switching from output “2” to output “1”, while bleaching of the QD absorption provides a contribution which is symmetric for both output arms.

5.5 Experiment

Photoluminescence (PL) studies carried out at low temperature (5K) on this sample showed a luminescence peak at 1250 nm from the quaternary InGaAsP layer and a broad luminescence peak at 1425 nm from the quantum dot layer. PL measurements at room temperature exhibit an absorption peak at 1300 nm with 50 meV FWHM due to the quaternary InGaAsP layer and a second peak between 1400-1600 nm with 90 meV FWHM due to the quantum dot layer. The broadening of the photoluminescence of the quantum dots is due to QD size variations. For this sample, the QD-size distribution was kept broad for obtaining a wavelength insensitive switching behaviour. The PL spectrum suggests that this sample will not be transparent around 1550 nm. The excitation power dependence of the PL spectra showed that for high excitation density the photoluminescence due to the quaternary InGaAsP layer is dominant over the quantum dot PL because of the high density of states of the bulk quaternary layer. At low pump power, the carrier occupation of the bulk quaternary layer reduces. Hence, we expect from the PL-data that the carrier occupation in the quantum dots will be dominant as compared to the carrier occupation in the bulk quaternary layer at low excitation levels. At high excitation density, the quantum dot absorption will be bleached [6], which leads to a spectrally flat refractive index nonlinearity. Waveguide characterization measurements at 1550 nm showed a TM loss of 11 dB/cm and a TE loss of approximately 30 dB/cm. Hence for our measurement we choose a TM-polarized probe beam. Unfortunately, the end-facets of the optical chip have not been AR-coated, resulting in Fabry-Perot resonances due to multiple reflections between the end facets of the chip. Due to the large waveguide loss, Fabry-Perot effects are expected to be small compared to the all-optical switching signal.

Since the quaternary absorption peak is well below 1400 nm, as is evident from our PL data, a pump wavelength tuned to >1400 nm avoids absorption in the cladding layer. At the maximum pump power of 0.125mW, the excitation density of the pump beam is estimated to be 83 mW/cm^2, which corresponds to an average carrier occupation of 5.10^{-4} carriers per QD per laser pulse, assuming an estimated absorption of 8.10^{-4} [12] for a single QD-layer. The probe beam is tuned to the 1530-1570 nm wavelength region, resulting in small TM-absorption in the quantum dot waveguide and large refractive index nonlinearity. For optimising the refractive index nonlinearity, we choose the probe wavelength as close as possible to the bandgap for TM-polarization. The bandfilling effect produced a change in absorption within the quantum dots and hence a carrier induced refractive index change within the waveguide. This resulted in a phase shift, which manifest itself as a switching of the probe beam in the MZI-switch. At a zero phase shift, the probe beam will be in the cross output port of the MZI-switch, while a π/2 phase shift switches the probe signal to the bar output port. The all-optical switching takes place due to refractive index nonlinearity in one of the arms of the MZI

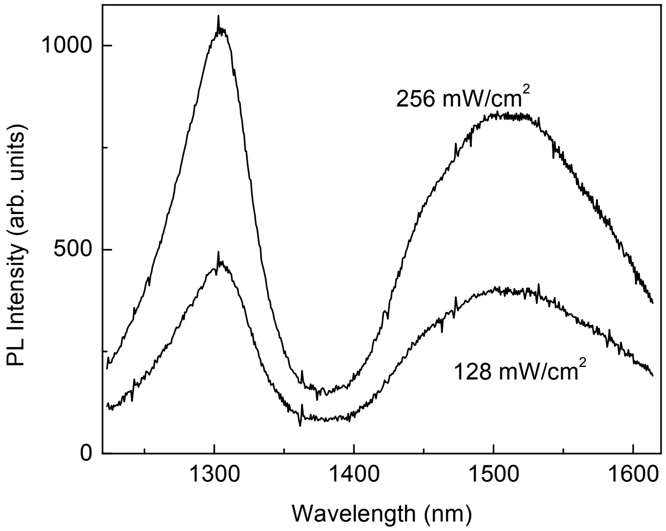

Figure5.6: Excitation Power dependence of PL spectra of InAs/InP quantum dots at 300K

due to the pump beam. As a result, the probe beam will be partially switched, in synchronism with the chopping frequency, from the cross to the bar output, which we detect with the Lock-in amplifier.

5.6 Results and discussion

Figure 5.7 shows the all-optical switching results for excitation of the QDs at 1450 nm and detection between 1530 nm and 1570 nm. The pump laser excitation density of 83 mW/cm^2 corresponds to a relative QD occupation of 0.05% at the highest power of 0.125 mW presented in figure 5.7. Since the PL spectrum shows a maximum at 1500 nm, one cannot expect a pure all-optical refractive index variation at 1570 nm without a bleaching component. We discriminate between bleaching and all-optical switching by using the switching principle explained in section 4.2

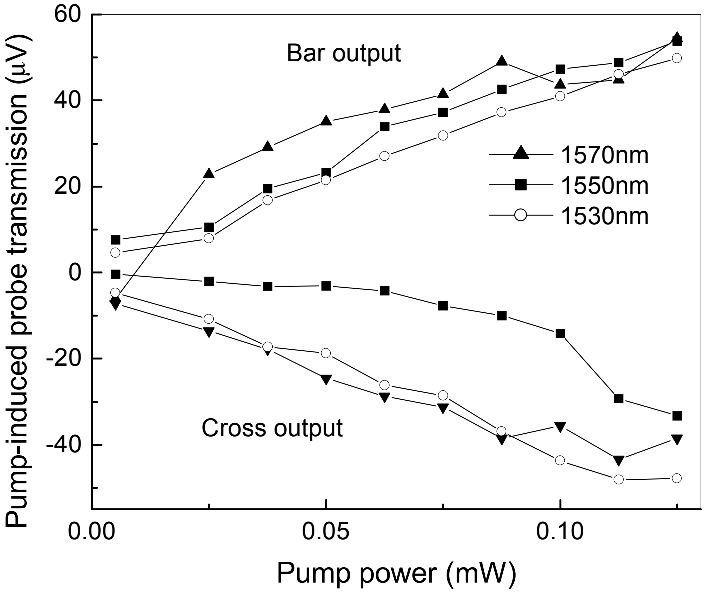

Figure 5.7: Demodulated probe transmission versus pump power, showing QD all-optical switching at a pump wavelength of 1450 nm and at probe wavelengths indicated in the figure

1. If only bleaching is present, both pump-induced probe transmission signals should have the same sign, but might be different in amplitude if the MZI-switch is not ideal.
2. If only a phase shift is present, both pump-induced probe transmission signals have the same magnitude, but opposite sign.

Since we observe demodulated probe signals of approximately opposite sign for both output arms of the MZI, we conclude that we observe mainly all-optical switching. A second argument for index of refraction nonlinearities are the strong oscillations of the demodulated probe transmission when we fine-tune the probe wavelength through the transmission characteristics of the MZI, which oscillate as a function of probe wavelength.

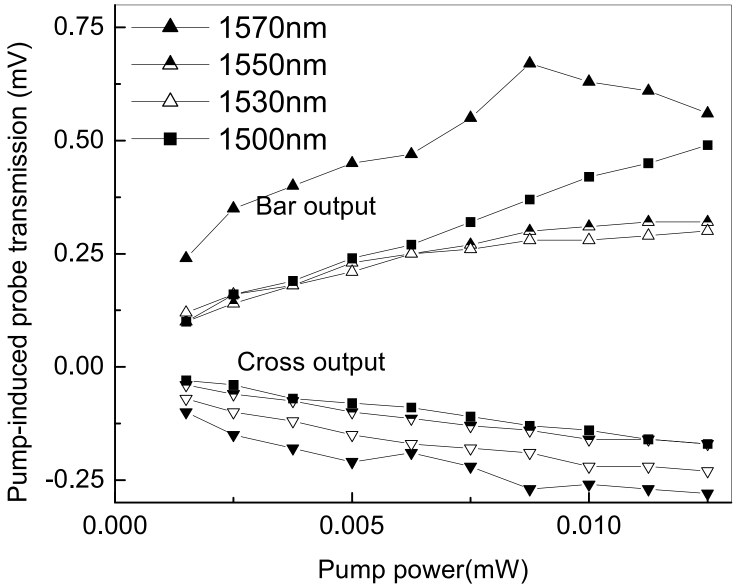

Figure 5.8: Demodulated probe transmission versus pump power at a pump wavelength of 1150 nm and at probe wavelengths indicated in figure

A third argument for the observation of all-optical switching is provided by the switching results presented in figure 5.8 using a 1150 nm pump laser wavelength. In this case, the photon energy is above the barrier of the InGaAsP waveguide core. In comparison to the result in figure 5.7 where only 0.05% of the QDs were excited, now an estimated 10% of all QDs will be populated due to the much larger absorption probability in the 0.37 μm InGaAsP waveguide core and the subsequent capture into the QDs. At this excitation wavelength, we could observe switching from the cross output to the bar output of the MZI on an infrared camera, which cannot be due to bleaching. The all-optical switching results presented in figure 5.8 cannot be completely attributed to state-filling in the QDs. At this excitation wavelength, there might also be a bandfilling contribution in the bulk InGaAsP due to carriers, which have not been captured into the QDs.

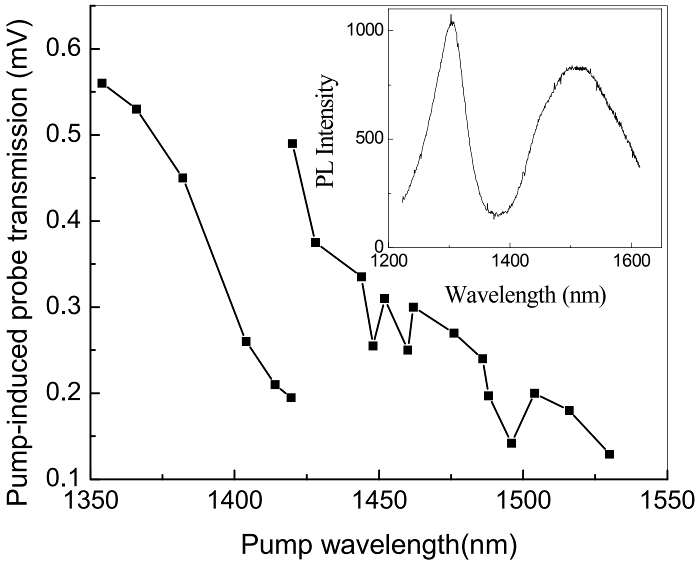

Figure 5.9: Pump wavelength dependence of the all-optical switching signal showing two measurement series. The inset shows the PL spectrum recorded at 256 mW/cm^2

The pump-wavelength dependence of the all-optical switching signal is presented in figure 5.9. It is shown that we observe a clear all-optical switching signal at pump wavelengths above 1400 nm, i.e. in the wavelength region where the absorption in the InGaAsP waveguide core decreases exponentially with the Urbach tail. The slow decrease of the all-optical switching signal thus cannot be explained by the residual absorption in the InGaAsP. Moreover, at our excitation density, we do not expect bandfilling in the InAs wetting layer. We thus interpret the observed all-optical switching as being due to state-filling in the InAs/InP QDs. The observed pump wavelength dependence is interpreted as being due to the integrated density of states of the QDs. At λ > 1500 nm, the pump laser can only excite the larger QDs, resulting in small pump absorption. At λ = 1400 nm, the pump laser is able to excite the full QD size distribution, including the excited states of the larger QDs and possibly also phonon replicas of these excited state [14], resulting in a larger expected pump absorption than at >1500 nm. The integrated density of states of these large InAs/InP QDs, which is defined as the number of QD-states in resonance with a laser, is thus expected to be a decreasing function with wavelength, in accordance with our experimental observation.

The probe wavelength dependence of the all-optical switching signal is shown both in figure 5.7 and 5.8. We observe that the switching efficiency is relatively wavelength insensitive due to the intentionally broad size distribution of the InAs/InP QDs giving rise to a 90 meV

FWHM PL-linewidth. From the PL-spectrum, we observe that the QD PL varied less than 10% in the range 1470-1550 nm. Within the experimental uncertainty, similar wavelength insensitivity is observed for the probe wavelength dependence.

We finally estimate the switching efficiency of the all-optical switch. From the switching curve presented in figure 5.7, we observe $2.6.10^{-4}$ rad phase shift at 0.125 mW pump power. Since 10% of this power directly excites the waveguide and the duty cycle in time is 0.5%, we find a phase shift of 4.2 rad/mW incident power. We finally corrected for the estimated 8.10^{-4} absorption strength [13] of a single QD-layer with a QD-height of 7 nm, yielding a switching efficiency of 5 rad/(μW absorbed power) or an absorbed energy of 6 fJ for a π phase change. The estimated index of refraction nonlinearity is $n_2 = 0.08$ /(μW absorbed power). We present the nonlinearity as a function of the amount of absorbed laser power since the absorbed laser power is a relevant quantity for all-optical switching [2,5]. This switching efficiency we obtained corresponds to 600 μm long phase shifter with a single QD-layer. Filling the waveguide core with multiple layers of QDs can further enhance the switching efficiency.

5.7 Conclusion

We observed all-optical switching due to the state filling effect in a single layer of InAs/GaAs quantum dot, embedded in an InGaAsP waveguide within a Mach Zehnder switch. An analysis of the switching principle of the MZI shows that the observed switching is clearly from refractive index nonlinearity, and not by the bleaching effect. The decreasing switching efficiency as a function of the pump wavelength in the wavelength region > 1400 nm mirrors the effective density of states of the quantum dot sample. The switching energy is finally calculated as 6 fJ which is interpreted as being due to the fact that a low pump intensity is already capable of saturating the quantum dot ground state transition by filling all quantum dots with 2 electron-hole pairs.

References

1. “A mechanism for low-power all-optical switching in multiple-quantum-well structures”, C. Knorr, U. Wilhelm, V. Harle, D. Ottenwalder, F. Scholz, and A. Hangleiter”, Appl.Phys.Lett., vol. 69, pp 4212-4214, 1996
2. “Demultiplexing of 168-Gb/s Data Pulses with a Hybrid-Integrated symmetric Mach-Zehnder All-Optical Switch”, S. Nakamura, Y. Ueno, K. Tajima, J. Sasaki, T. Sugimoto, T. Kato, T. Shimoda, M. Itoh, H. Hatakeyama, T. Tamanuki and T. Sasaki, IEEE Photon.Technol.Lett, vol. 12, pp 425-427, 2000
3. “Coherent Nonlinear Optical response of single quantum dots studied by ultra-fast near-field spectroscopy”, T. Guenther, C. Lienau, T. Elsaesser, M. Glanemann, V.M. Axt and T. Kuhn, Phys.Rev.Lett, vol.89, pp 057401-1-157401-4, 2002
4. “Optical nonlinear properties of InAs quantum dots by means of transient absorption measurements”, H. Nakamura, S. Nishikawa, S. Kohmoto, K. Kanamoto, and K. Asakawa, J.Appl.Phys., vol.94, pp 1184-1189, 2003 “Enhanced probabilities of phonon-assisted optical transitions in semiconductor quantum dots”, J.T. Devreese, V.M. Fomin, V.N. Gladilin, E.P. Pakatilov, S.N. Klimin, Nanotechnology, vol. 13, pp 163-168, 2002
5. “All-optical switching at multi-100-Gb/s data rates with Mach-Zehnder interferometer switches”, R.P. Schreieck, M.H. Kwakernaak, H. Jaeckel, H. Melchior, IEEE J. Quantum. Electron., vol. 38, pp 1053-1061, 2002
6. “Ultrafast refractive-index dynamics in a multiquantum-well semiconductor optical amplifier”, H.J.S. Dorren, X. Yang, D. Lenstra, H. de Waardt, G.D. Khoe, T. Simoyama, H. Ishikawa, H. Kawashima, T. Hasama, IEEE Photon.Technol.Lett, vol. 15, pp 792-794, 2003
7. “A chopped quantum-well polarization-independent interferometric switch at 1.53 μm “, B.H.P. Dorren, A.Yu. Silov, M.R. Leys, D.M.H. Dukers, J.E.M. Haverkort, D.H.P. Maat, Y. Zhu, F.H. Groen, J.H. Wolter, IEEE J. Quantum. Electron., vol. 36, 317, 2000
8. “ Polarization-independent dilated InP-based space switch with low crosstalk”, D.H.P. Maat, Y.C. Zhu, F.H. Groen, H. van Brug, H.J. Frankena, X.J.M. Leijtens, IEEE Photon.Tech.Lett., vol. 12, pp 284-286, 2000
9. “Reflection properties of multimode interference devices”, E.C.M. Pennings, R. van Roijen, M.J.N. van Stralen, P.J. de Waard, R.G.M.P.Koumans, B.H. Verbeek, IEEE Photon. Technol. Lett. Vol. 6, pp 715-718, 1994

10. “A compact PHASER with low central channel loss”, Y.C. Zhu, F.H. Groen, D.H.P. Maat, Y.S. Oei, J. Romijn, I. Moerman, Proc. ECIO, 1999, pp 219-222
11. “Novel 1 X N and N X N integrated optical switches using self-imaging multimode GaAs/AlGaAs waveguides”, R.M. Jenkins, J.M. Heaton, D.R. Wight, J.T. Parker, J.C.H. Birbeck, G.W. Smith, K.P. Hilton, Appl. Phys. Lett., vol. 64, pp 684-686, 1994
12. This analysis is based on a private communication by dr.J.J.G.M. van der Tol.
13. “Femtosecond dynamics and absorbance of self-organized InAs quantum dots emitting near 1.3 μm at room temperature”, D. Birkedal, J. Bloch, J. Shah, L.N. Pfeiffer, K. West, Appl. Phys. Lett, vol. 77, 2201-2203, 2000
14. “Enhanced probabilities of phonon-assisted optical transitions in semiconductor quantum dots”, J.T. Devreese, V.M. Fomin, V.N. Gladilin, E.P. Pakatilov, S.N. Klimin, Nanotechnology, vol. 13, pp 163-168, 2002

Summary

Optical communications requires fast, compact and polarization independent photonic switches. III/V semiconductor nano-structured materials such as self-assembled InAs/GaAs or InAs/InP quantum dots provide a great opportunity to enhance the performance of these photonic switches. However good theoretical understanding of the electro-refraction in the presence of an electric field and the index of refraction nonlinearities in these nanostructures is required to increase the switching efficiency. Since the absorption loss is a parasitic effect in the device performance, a main design criterion is to keep the absorption loss below an acceptable level of –25dB. However, since the index of refraction and the absorption are connected through the Kramers_Kronig relations, an optimum should be found between the undesired absorption loss and the required large refractive index variation.

In our theoretical model to understand the optical nonlinearities in quantum dots, we used the 4x4 Luttinger-Kohn Hamiltonian for calculating the band structure. We also incorporated lattice strain to achieve polarization independence. We substantially calculated the eigenvalues and eigenvectors of the electron and hole states by using a plane wave expansion. From the transition matrix elements, we calculated the absorption spectra and the refractive index variations, both due to the Quantum Confined Stark Effect (QCSE) and due to the carrier depletion effect.

Using the above-mentioned model, we optimized the electro-refraction in an "indirect in real space" $InAs_xP_{1-x}$ /InP/$In_{1-y}Ga_yAs$ quantum well by combining the QCSE and the carrier depletion effect. In this composite quantum well, the hole states are confined in the InGaAs quantum well, whereas the electronic states are confined in the InAsP well. Hence, polarization independent switching can be achieved by applying compressive strain to the InGaAs quantum well. The tensile strained InAsP quantum well provides strain compensation. The calculations show that a quantum well material which consists out of fifty (2 nm) $InAs_{0.65}P_{0.35}$/ (2.5 nm) $In_{0.38}Ga_{0.62}As$ quantum wells, allows to reduce the length of the phase shifting region in a symmetric Mach Zehnder Interferometer down to 0.92 mm. Using a MZI in push-pull configuration, the phase shifting region can be further reduced down to 0.46 mm.

We also investigate whether the discrete energy levels and the high peak absorption in quantum dots (QDs) provide an opportunity for increasing the electro-optic and nonlinear optical

properties. For this purpose we calculate the electro-refraction spectra of QDs, starting from the Luttinger-Kohn Hamiltonian and using a plane-wave expansion for solving the eigenstates of the QD. For a pyramidal InAs/GaAs quantum dot, we find a high peak electrorefraction of 0.35 for TE-polarization, which is 35x larger than in a quantum well. In the tail of the quantum dot absorption spectrum, we find an electrorefraction of 1.3×10^{-2} at an absorption loss of 0.15 dB/cm.

Finally, we experimentally investigate all-optical switching due to state filling in InAs/InP quantum dots. A monolayer of InAs quantum dots was embedded inside the core region of an InGaAsP/InP waveguide. The waveguide structure was grown by Chemical Beam Epitaxy. Photoluminescence shows that the quantum dots have an inhomogeneous size distribution with a peak at 1500 nm. Subsequently, a Mach-Zehnder Interferometric space switch has been etched in this structure, using reactive ion etching. In the switching experiment, the quantum dots are excited from the top, perpendicular to the MZI structure, by a beam from a femtosecond optical parametric amplifier, which can be tuned in the 1400-1600 nm wavelength region. The probe beam from a tunable diode laser is carefully coupled into one of the input waveguides of the MZI switch. We experimentally observe all-optical switching due to state-filling in the QDs. By exciting below the InGaAsP bandgap, we prove that the refractive index nonlinearity is entirely due to the QDs. The switching efficiency is 5 rad/(µW absorbed power), corresponding to a 6 fJ switching energy. Probe wavelength insensitivity was obtained using a broad size distribution of the QDs.

Samenvatting

In de optische telecommunicatie is er behoefte aan snelle en compacte optische schakelaars. III/V halfgeleider nano-gestructureerde materialen zoals zelf-organiserende InAs/GaAs of InAs/InP quantumdoosjes vormen een kansrijk materiaal om de eigenschappen van deze schakelaars te verbeteren. Een goed fysisch begrip van de variaties in de brekingsindex ten gevolge van een aangelegd elektrisch veld of ten gevolge van toestandsvulling in de quantumdoosjes is echter noodzakelijk om een hoge schakelefficiëntie te bewerkstelligen. Het is tevens een belangrijke ontwerpeis om het absorptieverlies in de golfgeleiders, met daarin de quantum doosjes, kleiner dan –25 dB te houden. Omdat het absorptieverlies en de brekingsindex niet-lineariteit aan elkaar gekoppeld zijn via de Kramers-Kronig relaties, dient een optimum tussen beide te worden gevonden.

In dit proefschrift worden de niet-lineaire eigenschappen van quantumdoosjes gemodelleerd met behulp van een model gebaseerd op de 4x4 Luttinger-Kohn hamiltoniaan. In dit model is de roosterspanning meegenomen om de optische eigenschappen polarisatie onafhankelijk te kunnen maken. De eigenwaarden en toestanden van de elektronen en gaten in de quantum doosjes zijn berekend met behulp van een expansie in vlakke golven. De absorptiespectra alsmede de brekingsindex veranderingen zijn vervolgens berekend met behulp van de overgangs-matrixelementen. Tenslotte hebben we hieruit de verandering in de brekingsindex berekend t.g.v. een extern elektrisch veld (Quantum Confined Stark Effect) en t.g.v. het ontrekken van ladingsdragers (depletie).

De variatie in de brekingsindex in een “indirecte” $InAs_xP_{1-x}$ /InP/$In_{1-y}Ga_yAs$ quantumput, t.g.v. van de combinatie van een extern elektrisch veld en het onttrekken van ladingsdragers zijn berekend. In deze “composiet” quantumput zitten de gaten opgesloten in de InGaAs put en de elektronen in de InAsP put. Polarisatie onafhankelijk schakelen kan in deze structuur worden bereikt door een compressie spanning aan te leggen in de InGaAs put. De rekspanning in de InAsP put zorgt voor compensatie van de opgebouwde roosterspanning. De berekeningen laten zien dat een 0.92 mm fase-sectie bestaande uit 50 InAsP/InP/InGaAs quantumputten in staat is om brekingsindex veranderingen van π te bewerkstelligen. In een Mach-Zehnder interferometer die werkt in push-pull operatie, kan de fase-sectie op basis van deze quantumputten zelfs worden verkleind tot 0.46 mm.

Er werd ook onderzocht in hoeverre de discrete toestandsdichtheid alsmede de hoge piekabsorptie in quantum doosjes, gelegenheid bieden om de elektro-optische effecten en niet-lineaire effecten verder te vergroten. Hiertoe zijn opnieuw de brekingsindex spectra berekend op basis van de Luttinger-Kohn hamiltoniaan, gebruik makend van een vlakke golf expansie. Voor een piramidevormig quantumdoosje vinden we een piek brekingsindex verandering van 0.35 voor TE-polarisatie, wat 35x groter is dan in een quantumput. In de staart van het absorptiespectrum vinden we nog steeds een brekingsindex verandering van $1.3x10^{-2}$ bij een rest absorptie verlies van 0.15 dB/cm.

In hoofdstuk V wordt een volledig optische schakelaar gerapporteerd die werkt op basis van een niet-lineariteit van de brekingsindex als gevolg van toestandvulling in InAs/InP quantumdoosjes. Hiertoe is een monolaagje InAs/InP quantumdoosjes gegroeid in de kern van een InGaAsP/InP optische golfgeleider met Chemische Bundel Epitaxie. De quantum doosjes geven fotoluminescentie bij 1500 nm. Vervolgens zijn deze structuren verwerkt tot Mach- Zehnder interferometrische (MZI) schakelaars met behulp van een etsproces met reactieve ionen. In het schakelexperiment worden de quantumdoosjes van boven af belicht met een laserbundel afkomstig van een optische parametrische oscillator die afstembaar is tussen de 1400 en 1600 nm. De niet-lineariteit van de brekingsindex wordt afgetast met een tweede bundel afkomstig van een afstembare halfgeleider diodelaser. Deze bundel wordt ingekoppeld in een ingangsgolfgeleider van de MZI. We zien nu dat de aftastbundel wordt geschakeld van de “rechtdoorgaande” uitgang naar de “gekruisde” uitgang van de MZI t.g.v. de niet-lineariteit in de brekingsindex. Door te belichten met licht met een energie onder de InGaAsP bandkant, kunnen we bewijzen dat het schakeleffect het gevolg moet zijn van toestandvulling in de quantumdoosjes. De schakelefficiëntie is 5 rad/(µW geabsorbeerd vermogen), hetgeen correspondeert met een schakelenergie van slecht 6 femtoJoule. Tenslotte is de schakelaar relatief ongevoelig voor de golflengte van de aftastlaser als gevolg van de grote variatie in de afmetingen van de quantumdoosjes.

Publications:

Journal Papers:

1. “Compact polarization-independent Mach-Zehnder space switch, combining carrier depletion and the Quantum Confined Stark Effect”, R.Prasanth, J.E.M.Haverkort, J.H.Wolter, IEEE Journal of Quantum Electronics , Vol 39(2), pp 379-383, (2003)

2. “Electrorefraction in quantum dots: Dependence on lateral size and shape”, R.Prasanth, J.E.M.Haverkort, J.H.Wolter, IEEE. Transactions on Nanotechnology, (in press)

3. “All Optical Switching due to state-filling in quantum dots”, R.Prasanth, J.E.M. Haverkort, A. Deepthy, J.J.G.M. van der Tol, E.A. Patent, G. Zhao, Q. Gong, P.J.van Veldhoven, R. Nötzel and J.H. Wolter, Submitted to Appl.Phys.Lett

4. ”Low-Crosstalk Penalty MZI Space Switch with a 0.64mm Phase Shifter using Quantum-Well Elecrorefraction”, B.H.P.Dorren, J.E.M.Haverkort, R.Prasanth, F.H.Groen and J.H.Wolter, IEEE Photon. Technol. Lett., Vol 13(1) pp37-39 (2001)

5. ”A photoacoustic study of the effect of doping concentration on the transport properties of GaAs epitaxial layers“, S.D. George, Dilna S, Prasanth R, P.Radhakrishnan, C.P.G.Vallabhan, V.P.N.Nampoori, Optical Engineering , Vol 42, No 5, pp 1476-1480, (2003)

Conference papers:

6. “Compact Mach-Zehnder Space switch combining bandfilling and the quantum confined Stark effect”, R.Prasanth, J.E.M.Haverkort, J.H.Wolter IEEE/LEOS Symposium, Benelux Chapter, pp21-24 December, 2001 ,Brussel, Belgium

7. “Electrorefraction in Quantum Dots", R.Prasanth, J.E.M.Haverkort, J.H.Wolter, IEEE/LEOS Symposium, Benelux chapter, December 2002, Amsterdam, The Netherlands pp 234-237

8. “Electrorefraction in Quantum dots: Dependence on lateral size and shape”, R.Prasanth, J.E.M.Haverkort, J.H.Wolter, IEEE Nano-2003 conference, August 2003, San Francisco, USA

9. ”All Optical Switching in a quantum dot switch”, R.Prasanth, J.E.M. Haverkort, A. Deepthy, J.J.G.M. van der Tol, E.A. Patent, G. Zhao, Q. Gong, P.J.van Veldhoven, R. Nötzel and J.H. Wolter, Proceedings SAFE 2003 conference, Veldhoven, The Netherlands, 2003

10. “Wavelength insensitive all-optical switching in quantum dots”, J.E.M. Haverkort, R.Prasanth, A. Deepthy, E.W.Bogaart, J.J.G.M. van der Tol, E.A. Patent, G. Zhao, Q. Gong, P.J.van Veldhoven, R. Nötzel and J.H. Wolter, IEEE/LEOS symposium, Benelux Chapter, November 2003, Enschede, The Netherlands, pp 193-196

11. “Ultrashort Mach-Zehnder space switch based on quantum dots”, R. Prasanth, J.E.M. Haverkort, J.H. Wolter, Smart Structure and Materials; Modeling, Signal Processing, and Control, SPIE Conference 5383, San Diego, USA, March 14-18 2004

12. “A Polarization Independent MZI space switch with a 0.64 mm phase shifter and a low crosstalk penalty”, B.H.P.Dorren, R.Prasanth, J.E.M.Haverkort, F.H.Groen, J.H.Wolter, IEEE/LEOS symposium, Benelux Chapter, November 1999, Mons, Belgium pp 65-68

Curriculum Vitae

I was born in the coastal village Eravipuram, in Kerala, the southern state of India on 19 August 1972. I received my Master of Science degree in Physics from the University of Kerala in 1995. In 1998 I received Master of Technology degree in Opto-Electronics from Cochin University of Science and Technology (CUSAT). From June 1999 onwards, I pursued my education by research on photonic switching in the Semiconductor Physics group at the Eindhoven University of Technology (TU/e), the Netherlands. The research that resulted in this PhD thesis was part of a “sandwich PhD program” between TU/e and the International School of Photonics at CUSAT within the framework of the NUFFIC (Netherlands organization for international cooperation in higher education) sponsored “Joint financing program for cooperation in Higher Education (MHO)”.

Acknowledgements

At this moment of great satisfaction, I have to acknowledge a number of people who helped and encouraged me with the successful completion of this Thesis. First of all, my sincere thanks to my promotor, Prof.Dr. J.H. Wolter, for providing me all the facilities and enough time to finish my work. Heartfelt thanks to my co-promotor, dr. J.E.M. Haverkort, for introducing me to this exciting field of research and helping me with ideas and suggestions. I would like to thank my second promotor, Prof. V.P.N. Nampoori, who motivated me with the basic ideas of photonics. A word of thanks is just not enough for dr. B.Premlet, who taught me the basic concepts of physics and encouraged me with all kind of advice at the moment of crisis. I would like to thank Prof. Girijavallabhan for his help and support. I am also thankful to Prof. Nandakumaran and Prof.Radhakrishnan. Dr. Deepthy's help and encouragement was incredible for the successful completion of my experimental work. I would like to thank all my colleagues in the group Semiconductor Physics, especially Rene van Veldhoven, dr. Gong and dr. Richard Noetzel for growing the sample necessary for my experiment. I am also thankful to dr. Jos van der Tol and Evgeni Patent for etching the Mach Zehnder Interferometer switch. I would like to thank my colleague and friend Aneeshkumar for his company and help. "A friend in need is a friend indeed". My sincere thanks also extend to Harm, Eric and Twan for their valuable corporation.
Mr. Jan van Schijndel, Mr. Jan van Cranenbroek and Ir. Patrick van Schijndel did a remarkable work in managing the MHO project and arranging accommodation and facilities during my stay in Eindhoven. I have great appreciation for them. I thank the group secretary, Ms. Margriet van Doorne, for her help and encouragement. I am also grateful to all my Indian friends in Eindhoven for creating a homely atmosphere in Eindhoven that helped me a lot in research and life.

Finally I bow my head to my parents, '*the real source of endless inspiration*'!